University of Alberta

Imaging Mantle Discontinuities and Velocity Structures
Using the Radon Transform

by

Yuling An ©

A thesis submitted to the Faculty of Graduate Studies and Research in partial fulfilment
of the requirements for the degree of **Master of Science.**

in

Geophysics

Department of Physics

Edmonton, Alberta
Fall 2007

Canada

Abstract

Transition zone discontinuities highlight density and velocity variations in the mantle and provide key information on the Earth's thermal and chemical evolution. SS precursors are highly sensitive to upper mantle discontinuities and have been used to image large-scale mantle structures. Traditional methods to increase the signal-to-noise ratio in SS precursors are stacking or slowness slant stack, which cannot well constrain the ray parameter. To overcome the limitation of these methods, the Radon transform is introduced to suppress background noise, simultaneously constrain differential travel times and ray parameters, and detect weak reflected or converted phases.

By applying Radon transforms, we are able to delineate discontinuity structures beneath the northeastern Pacific Ocean and the northwest Canada. Also, differential travel time curves or ray parameters impose alternative constraints on the upper-lower mantle velocity structure beneath hotspot locations, in addition to the depth of 400-km discontinuity and transition zone thickness.

Acknowledgements

I would like to thank my supervisor, Dr. Mauricio D. Sacchi and Dr. Yu J. Gu for their kindly guidance and propelling during the process of this research project. Thanks to Ahmet Okeler, Christian Escalante, Keith Brzak and all my friends for their friendship, intellectual support and valuable suggestions during my research. Also I appreciate Joshua Davidson and Martin Knapmeyer for their programming help. Special thanks to my family for their support and encouragement during my studies at the University of Alberta.

Table of Contents

List of Tables

List of Figures

List of Symbols and Abbreviations

Symbol or Abbreviation	Name or Description
τ	Intercept travel time
p	Ray parameter / Radon parameter
t	Travel time in seconds
x	Offset (distance between source and receiver)
d	Seismic data
u	Radon domain signal
ϕ, ϕ'	Integration paths
e	Additive noise
$\mathbf{L}$	Forward Radon operator
$\mathbf{L}^{-1}$	Inverse Radon operator
$\mathbf{I}$	Unit matrix
μ	Regularization (trade-off) parameter
f	Temporal frequency in Hertz (Hz)
D	Seismic data in frequency domain
U	Radon signal in frequency domain
E	Additive noise in frequency domain
b	Hyper-parameter (a small constant)
$\mathbf{Q}$	A diagonal matrix
G	Resolution matrix
X	Original bootstrap dataset
X'	Bootstrap sample

Symbol or Abbreviation	Name or Description
IRLS	Iteratively re-weighted least squares
CG	Conjugate Gradients
PREM	Preliminary Reference Earth Model
TZ	Transition Zone
DLS	Damped least-squares
LRT	Linear Radon transform
FRT	Forward Radon transform
RT	Radon transform
SSS	Slowness slant stack
IC	Inner core
OC	Outer core
SNR	Signal-to-noise ratio
LSRT	Least-squares Radon transform
NQRT	Non-quadratic Radon transform
CMB	Core mantle boundary
Rw	ringwoodite
Mj	Majorite garnet
Pv	perovskite
Il	ilmenite
Mw	magnesiowustite
2D	Two dimension
FF	Finite frequency
d	Deep plume
pd	Potentially deep plume
mm	Mid-mantle

Chapter 1

Introduction

1.1 Background

The existence and the characteristics of seismic discontinuities have been widely used as effective tracers of thermal and compositional variations in the mantle. Via the most robust seismological observations, mantle transition zone (TZ) discontinuities have been shown to exist globally [*e.g.*, *Shearer* and *Masters*, 1992; *Shearer*, 1993; *Gossler* and *Kind*, 1996; *Flanagan* and *Shearer*, 1998; *Gu et al.*, 1998; *Flanagan* and *Shearer*, 1999; *Gu* and *Dziewonski*, 2002; *Chambers et al.*, 2005] and their lateral depth variations potentially reflect the local pressure-temperature conditions under which olivine phase transitions take place [*Ringwood*, 1975; *Agee* and *Walker*, 1988; *Katsura* and *Ito*, 1989]. Temperature perturbations, which can cause tens of kilometers of topography on a given discontinuity, have been reported both on local and global scales [*Gossler* and *Kind*, 1996; *Gu et al.*, 1998; *Deuss* and *Woodhouse*, 2002]. Other seismic discontinuities/reflectors are only intermittently reported and remain controversial, most notably near 220-km (largely continental) [*Gu et al.*, 2001; *Deuss* and *Woodhouse*, 2002], 250-350 km [*Revenaugh* and *Jordan*, 1991; *Deuss* and *Woodhouse*, 2002], 500-600 km (global) [*e.g.*, *Shearer*, 1990; *Deuss* and *Woodhouse*, 2001], and 900-1200 km [*Kawakatsu* and *Niu*, 1994; *Niu* and *Kawakatsu*, 1997]. Each of them represents a potential piece of the puzzle in the accurate description of the subsurface thermal and composition regimes.

Global constraints on mantle discontinuities mainly come from long-period waves, despite the increasing popularity of higher-frequency method such as receiver functions in recent years. Receiver function is one of the most popular high resolution methods to study TZ discontinuities. Receiver function has resolution on a scale of a few hundreds of kilometers, but its application is limited by the distribution of multi-component seismic stations. In addition, they can only resolve structures in the depth range between ~100 km and ~400 km [*Du et al*, 2006]. The structure at depth deeper than 400 km is accessible

1

only with long-period phases, which instead, have lower lateral resolution. Of the methods based on long-period waves, SS precursors remain one of proven means for identifying and interpreting mantle reflectors [e.g., Shearer and Master, 1992; Shearer, 1993; Gossler and Kind, 1996; Gu et al., 1998; Flanagan and Shearer, 1998; Gu and Dziewonski, 2002; Schmerr and Garnero, 2006]. These weak underside reflections are highly sensitive to both depth and reflectivity of mantle reflectors but, to a much less extent, to the station location. For notation convenience, we name each discontinuity by its Preliminary Reference Earth Model [PREM, Dziewonski and Anderson, 1981] depth even though the actual depth may vary. For example, TZ discontinuities are named 400-km and 670-km discontinuities after PREM.

Among techniques used in analyzing SS precursors, waveform stacking of data at similar geographical locations (or 'bins') is commonly used to enhance signal-to-noise ratio [e.g., Shearer, 1993]. Occasional variations in identifying and differentiating these weak seismic phases include slowness slant stack which stack seismograms along a given slowness [Gossler and Kind, 1996; Gu et al., 1998] or back azimuth (the "vespa" technique) [Rost and Thomas, 2002]. However, these methods cannot well constrain the ray parameter. To overcome these limitations, in this study, we introduce Radon transforms to provide more accurate, high-resolution solutions for differential travel times and ray parameters of SS precursors. The Radon transform is a technique to attenuate incoherent noise and suppress multiples in seismic exploration. This method also provides an effective mechanism to resample the data in space domain. While similar approaches have been used in focusing the energy of shallow seismic signals and attenuating correlated/random noise [Hampson, 1986; Foster and Mosher, 1992], their potential applications in global seismology are still thinly explored [Wilson and Guitton, 2007].

1.2 Motivation

During the last two decades, with the development of digital seismometers and digital recording systems, high quality broad band seismic signals are available from global seismic networks. With the improvement of data quality, seismologists switch their targets from striving to improve the data quality to introducing new techniques into seis-

2

mology. Motivated by densely distributed high-quality tele-seismograms, we are seeking to introduce the Radon transform, a successful technique in processing seismic data in seismic exploration, to global seismology. By employing the Radon transform, a simultaneous constraint of differential travel times and ray parameters of *SS* precursors allows for more accurate interpretation of mantle discontinuities.

1.3 Scope of this work

The purpose of this thesis is to investigate the feasibility of the linear Radon transform in global seismology. The Radon transform is proven to be effective in attenuating coherent and incoherent noise from seismograms, isolating travel time and ray parameter, interpolating seismic data, and further constraining the TZ depth and infering velocity variation of the mantle. The novelty of this thesis consists in inferring the velocity structure with a more sensitive element ---- ray parameter. The weak reflections of SS precursors, which are always embedded in extensive background noise for individual seismograms, are adopted to assess the effectiveness of the Radon transform. With the Radon transform, a more accurate interpretation of mantle discontinuities is presented where velocities are constrained by differential ray parameters.

1.4 Thesis outline

The linear Radon transform and its solutions are presented in Chapter 2. Time and frequency domain implementations of the linear Radon transform are described and compared. Two important properties of Radon transforms ---- filtering and interpolation, are presented. The relation between the Radon transform and slowness slant stack is also studied.

Chapter 3 focuses on the implementation of the Radon transform to SS precursors. The feasibility of the technique to process SS precursors is fully examined with synthetic and real seismic recordings.

In Chapter 4, one applications of the Radon transform in global seismology are presented. By constraining the differential travel time and ray parameter with the least-squares Radon transform, mantle discontinuities are examined and imaged.

In Chapter 5, the non-quadratic Radon transform (high resolution Radon transform) is adopted to constrain differential travel times and ray parameters. The upper-mid mantle velocity structure is investigated beneath 17 hotspot locations.

Finally, Chapter 6 summarizes the research and discusses the results along with possible future directions.

4

Chapter 2

The Radon Transform

The Radon transform is a mathematical technique used in seismic imaging to attenuate undesired signals, such as multiples, source generated noise, and surface waves [*Hampson*, 1986]. The Radon transform is more commonly known as the slant-stack or the τ - p transform (τ denotes intercept time and p is ray parameter). In general, the Radon transform is defined as a simple integration of the data along a family of parametric paths. Therefore, the linear Radon transform can map linear arrivals in the t - x (time – space) domain into points in the transformed domain (often called the τ - p domain).

Algorithms for the Radon transform have been developed during last two decades. *Thorson* and *Claerbout* [1985] suggested a time domain hyperbolic least-squares method which gives a high resolution result at the expense of a large matrix computation during the inversion. *Hampson* [1986] proposed a much more efficient frequency domain least-squares parabolic transform method which immediately became the industry standard; however, the result is smeared in the $\tau - p$ domain and suffers from truncation artifacts. *Sacchi* and *Ulrych* [1995] introduced a fast frequency domain sparseness algorithm by means of Bayes rule using a Cauchy-like norm, which is generally used in seismic processing. In 1999, *Sacchi* and *Porsani* proposed a new conjugate gradient method that operates with circulant matrices to further reduce the computational cost of the Radon transform.

In this chapter, I introduce the Radon transform, basically, the linear Radon transform. Chapter 2.1 explains the concept of the Radon transform. Chapter 2.2 illustrates the implementation of the linear Radon transform in the time and frequency domain. In chapter 2.3, the high resolution Radon transform with non-quadratic solution is explained. Chapter 2.4 presents two important properties of the Radon transform that are useful in processing tele-seismic data. Chapter 2.5 illustrates the relation between the Radon transform and the Vespa process [*Rost* and *Thomas*, 2002] or slowness slant stack with a synthetic example. A summary is presented in chapter 2.6.

5

2.1 The linear Radon transform

In general, the Radon transform is a simple integration of the data along a family of parametric lines and can be expressed as the following transformation

$$\tilde{u}(\tau, p) = \int_{-\infty}^{\infty} d(t = \phi(\tau, p, x), x) dx . \tag{2.1}$$

Where, $\tilde{u}(\tau, p)$ denotes the transformed signal (or $\tau - p$ signal) in the transformed domain (the Radon domain or $\tau - p$ domain), $d(t, x)$ represents the data in time domain, and $t = \phi(\tau, p, x)$ represents the integral path. The variables τ and p represent the intercept time and ray parameter, respectively. Similarly, the variables x and t represent distance (or offset) and time.

To project the Radon domain signal back to the original time domain, a forward Radon transform is defined

$$d(t, x) = \int_{-\infty}^{\infty} u(\tau = \phi'(t, x, p), p) dp . \tag{2.2}$$

The above equations (2.1) and (2.2) are not the exact inverse pair; rather, they form a forward-adjoint pair.

In practice, data are sampled and recorded at certain values, so we use discrete Radon transform as a summation of data over a range of distances [x_{min}, x_{max}],

$$\tilde{u}(\tau, p_j) = \sum_{k=1}^{N} d(t = \phi(\tau, p_j, x_k), x_k) , \tag{2.3}$$

where $t = \phi(\tau, p_j, x_k)$ is a discrete function that represents the summation path and it is chosen based on the desired application. The adjoint pair becomes

$$d(t, x_k) = \sum_{j=1}^{M} u(\tau = \phi'(t, x_k, p_j), p_j) . \tag{2.4}$$

Usually, the Radon transform used in exploration seismology integrate arrivals along a linear, parabolic or hyperbolic curve. Here, I will describe the linear Radon transform (LRT) which integrate arrivals along a linear line; since the relative travel time curves of SS precursors are well approximated by linear lines.

6

In this case, the summation path is

$$t = \tau + px .\tag{2.5}$$

Mathematically, the linear discrete Radon transform is represented as follows:

$$\tilde{u}(\tau, p_j) = \sum_{k=1}^{N} d(t = \tau + p_j x_k, x_k) .\tag{2.6}$$

Equation (2.6) is the low resolution Radon transform and can be used to search for seismic arrivals with linear arrivals. It can be interpreted as a transformation that maps a linear waveform in $t - x$ domain to a point in $\tau - p$ domain, which is true if we assume an array of infinite aperture.

Rather than using equation (2.6), we adopt the following expression which is often called the forward Radon transform (FRT):

$$d(t, x_k) = \sum_{j=1}^{M} u(\tau = t - p_j x_k, p_j) .\tag{2.7}$$

By using expression (2.7), we are able to represent the data as a linear superposition of signals in the $\tau - p$ domain. The advantage of equation (2.7) is that we can consider the Radon transform as an inverse problem. In addition, after estimating and filtering the $\tau - p$ model, we can apply the forward Radon transform to reconstruct the data.

Considering the noise or the part of data that are not modeled by the transform, the forward Radon transform can be incorporated into the formulation as follows:

$$d(t, x_k) = \sum_{j=1}^{M} u(\tau = t - p_j x_k, p_j) + e(t, x_k) .\tag{2.8}$$

The error term $e(t, x_k)$ accounts not only for noise but also for undesired scattered waveforms that are not modeled by the forward Radon operator.

7

2.2 Inversion of the forward Radon transform

To solve the Radon transform as an inverse problem, usually we adopt the forward Radon transform (2.8). In this chapter, I will present techniques to invert equation (2.8). Linear Radon transform is time invariant; therefore, it can be solved in time domain and frequency domains. One advantage of the computation in the frequency domain is that a large matrix computation can be broken into several smaller ones. To solve it in time domain, inversion of large matrices is unavoidable; while the advantage of the time domain implementation is that it gives more flexibility in choosing integral path.

2.2.1 Time domain implementation

To solve the linear Radon transform in time domain, equation (2.8) can be rewritten in a matrix form

$$\mathbf{d} = \mathbf{Lu} + \mathbf{e} \tag{2.9}$$

where, the Radon model is represented by $\mathbf{u}$, the data is denoted by $\mathbf{d}$, the forward operator is $\mathbf{L}$, and the error term is $\mathbf{e}$.

Equation (2.9) can be solved as an inverse problem. The damped least-squares (DLS) solution [*Menke, 1989*] is obtained by minimizing the following cost function

$$J = \|\mathbf{Lu} - \mathbf{d}\|_2^2 + \mu \|\mathbf{u}\|_2^2 \tag{2.10}$$

where $\|\mathbf{Lu} - \mathbf{d}\|_2^2$ is the misfit, a measure of how well the forward Radon operator can model the data. The second term $\|\mathbf{u}\|_2^2$ is the regularization term (also known as damping or penalty term), which is the quadratic model norm required to stabilize the solution. μ is the trade-off (regularization) parameter to control the stability and resolution of the inverse problem.

Taking derivatives of J with respect to $\mathbf{u}$ and set them to zero leads to the following damped least-squares solution,

$$\mathbf{u} = (\mathbf{L}^T\mathbf{L} + \mu\mathbf{I})^{-1}\mathbf{L}^T\mathbf{d}, \tag{2.11}$$

where T represents the transpose operator.

8

The Radon transform is solved as an inverse problem; while the solution is often unstable and non-unique. To overcome this pitfall, a trade-off parameter μ is introduced to control the stability and resolution to which the forward Radon operator can model the data. An optimal trade-off parameter μ can be determined from a L-curve [*Engl* and *Grever*, 1994]. The L-curve, also known as the trade-off diagram, indicates that a small trade-off parameter will produce a solution with a small misfit and a large model norm. This class of solution is considered unstable and, in addition, a clear indication of data over-fitting. In other words, excessive data fitting leads to an unstable solution with a large model norm. Conversely, a large value trade-off parameter leads to a solution that does not fit the data and the signals are not well focused in the Radon transform. Therefore, to avoid over and/or under fitting the data, one needs to find a trade-off parameter that leads to well-focused Radon transforms and good modeling properties. Based on this criterion, the turning point in the L-curve is chosen as the trade-off parameter [*Engl* and *Grever*, 1994].

2.2.2 Frequency domain implementation

To avoid the inversion of large matrices, the linear Radon transform can be solved in the $f - x$ (frequency-space) domain, which allows us to break one big problem into several smaller problems.

By applying the Fourier transform with respect to the temporal variable t to both sides of equation (2.8) and by using the Fourier delay theorem [*Papoulis*, 1962], expression (2.8) reduces to the following expression

$$D(f, x_k) = \sum_{j=1}^{M} U(f, p_j)e^{-i2\pi f x_k p_j} + E(f, x_k).$$ (2.12)

In this formulation, time domain signals are transformed into frequency domain. Implementing computation in frequency domain is more convenient for time-invariant transform, such as, the linear Radon transform. With this method, the inversion of large matrices can be avoided. This technique was adopted by *Beylkin* [1987], *Foster* and *Mosher* [1992], and *Sacchi* and *Ulrych* [1995].

Expression (2.12) can be expanded as following matrices:

9

$$
\begin{pmatrix} D(f,x_1) \\ D(f,x_2) \\ \cdot \\ \cdot \\ \cdot \\ D(f,x_N) \end{pmatrix} = \begin{pmatrix} e^{-i2\pi fx_1 p_1} & e^{-i2\pi fx_1 p_2} & \cdot & e^{-i2\pi fx_1 p_M} \\ e^{-i2\pi fx_2 p_1} & e^{-i2\pi fx_2 p_2} & \cdot & e^{-i2\pi fx_2 p_M} \\ \cdot & \cdot & \cdot & \cdot \\ \cdot & \cdot & \cdot & \cdot \\ \cdot & \cdot & \cdot & \cdot \\ e^{-i2\pi fx_N p_1} & e^{-i2\pi fx_N p_2} & \cdot & e^{-i2\pi fx_N p_M} \end{pmatrix} \begin{pmatrix} U(f,p_1) \\ U(f,p_2) \\ \cdot \\ \cdot \\ U(f,p_M) \end{pmatrix} + \begin{pmatrix} E(f,x_1) \\ E(f,x_2) \\ \cdot \\ \cdot \\ \cdot \\ E(f,x_N) \end{pmatrix} . \quad (2.13)
$$

To avoid notational clutter, equation (2.13) is rewritten as the following matrix expression:

$$
\mathbf{D}(f) = \mathbf{L}(f)\,\mathbf{U}(f) + \mathbf{E}(f) . \quad (2.14)
$$

It is clear that for a single monochromatic frequency f, we have reduced our problem to a linear inverse problem.

Equation (2.14) can be solved using the damped least-squares method [*Menke*, 1989] by finding the minimum of the following cost function:

$$
J(f) = \|\mathbf{L}(f)\mathbf{U}(f) - \mathbf{D}(f)\|_2^2 + \mu\|\mathbf{U}(f)\|_2^2 . \quad (2.15)
$$

The first term in the right hand side is the data misfit; the second term is the model norm, or the regularization term.

The damped least-squares solution is found by minimizing equation (2.15) with respect to the unknown vector $\mathbf{U}(f)$. The minimum of equation (2.15) is given by

$$
\mathbf{U}(f) = (\mathbf{L}^H(f)\mathbf{L}(f) + \mu\mathbf{I})^{-1}\mathbf{L}^H(f)\mathbf{D}(f) , \quad (2.16)
$$

where H represents the conjugate transpose operator. It is important to stress that expression (2.16) must be solved for all frequencies. Once $\mathbf{U}(f)$ is obtained for all frequencies, we use the inverse Fourier transform to map $U(f,p_j)$ back to time domain. The final result is the Radon operator $u(\tau,p_j)$ in the time domain.

10

2.3 The non-quadratic solution

It is important to stress that several strategies exist to invert equation (2.8). In addition to damped least-squares method, non-quadratic regularization method could has also been adopted [*Sacchi* and *Ulrych*, 1995] and it had been applied in global seismology to solve receiver functions [*Escalante et al*, 2007] and to migrate depths [*Wilson* and *Guitton*, 2007]. Under good SNR conditions, non-quadratic regularization methods allow to generate sparse solution in the $\tau - p$ domain, which is also known as high resolution Radon transform. In other words, it represents a Radon transform where the energy in the model domain is focused without transformation artifacts introduced by limited aperture.

If sparseness is expected in the solution, the regularization terms are required and represented by various norms. *Sacchi* and *Ulrych* [1995] introduced non-quadratic regularization norm into the inversion: Huber norm and Cauchy norm. Here, I only discuss Cauchy-like norm to be the sparseness constraint and obtain non-quadratic solutions. The Cauchy function is given by

$$\rho_c(u) = \ln(\frac{u^2}{2} + 1),$$ (2.17)

where, u is the time domain signal. The Cauchy norm regularization is defined as

$$\Re_C(u) = \sum_i \rho_C(u_i / \sigma).$$ (2.18)

With the Cauchy-like norm, we minimize the following cost function

$$J = \|\mathbf{Lu} - \mathbf{d}\|_2^2 + \mu \sum_k ln(1 + u_k^2/b),$$ (2.19)

where u_k indicates an element of $u(\tau, p)$ after lexicographic arrangement (transformation of a matrix into a vector), b is a small constant. The parameters μ and b are the hyper-parameters of the problem [*Sacchi* and *Ulrych*, 1995].

Taking derivatives of J with respect to u_k and equal them to zero leads to the following solution,

$$u^k = (\mathbf{L}^T\mathbf{L} + \mu\mathbf{Q}(u)^{k-1})^{-1}\mathbf{L}^T\mathbf{d}.$$ (2.20)

11

Here, $\mathbf{Q}$ is a diagonal matrix with elements given by

$$Q_{ii} = \frac{1}{b + |u_i|^2},$$

(2.21)

and k indicates the iteration. The matrix of weights $\mathbf{Q}$ is computed from the result of the previous iteration.

The high resolution Radon transform can be solved in the time domain and/or frequency domain. However, the non-quadratic Radon transform solved in frequency domain can only impose sparsity in p direction due to the transformation of data in the time domain to the frequency domain. On the other hand, the non-quadratic Radon transform solved in the time domain will impose sparseness constraints in both $\tau - p$ domains.

In general, the most often used method for solving damped least-squares or non-quadratic solutions is the iteratively re-weighted least squares (IRLS) [*Scales* and *Gersztenkorn*, 1988] because of its simplicity and efficiency. Also one can solve the problem using conjugate gradient (CG) method. The CG algorithm removes the need to store the large matrix $\mathbf{L}$.

Figure 2-1 and Figure 2-2 compare the inversion results from damped least-squares solution and non-quadratic solution. Both are solved in the time domain. The same synthetic data in Figure 2-1(a) and Figure 2-2(a) are shown with three linear arrivals and some random noise. The Radon signal solved by damped least-squares [Figure 2-1(b)] obviously has lower resolution than the one computed with the non-quadratic regularization in Figure 2-2(b). With the Radon operators in Figure 2-1(b) and Figure 2-2(b), the data are reconstructed and shown in Figure 2-1(c) and Figure 2-2(c), respectively. The residuals displayed in Figure 2-1(d) and Figure 2-2(d) are noise dominated.

12
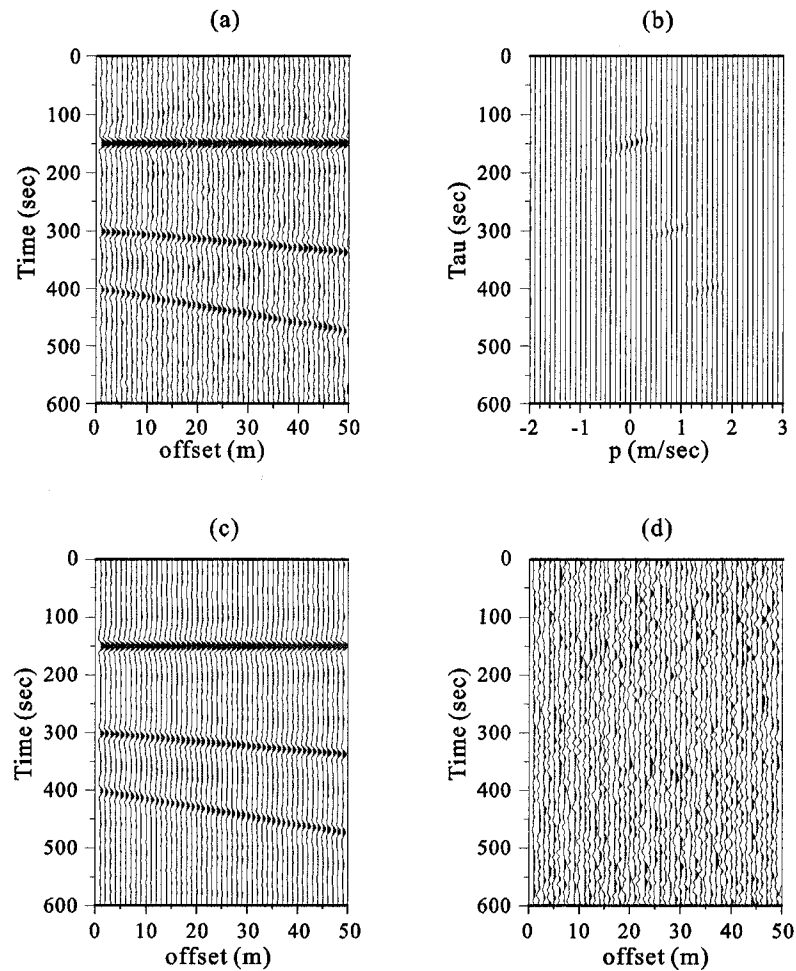
Figure 2-1 The damped least-squares Radon transform of a synthetic dataset. (a) Synthetic data. (b) The Radon signals solved in time domain by damped least-squares method. (c) Reconstructed data from the Radon signals in (b). (d) The difference between original data (a) and reconstructed data (c).

13
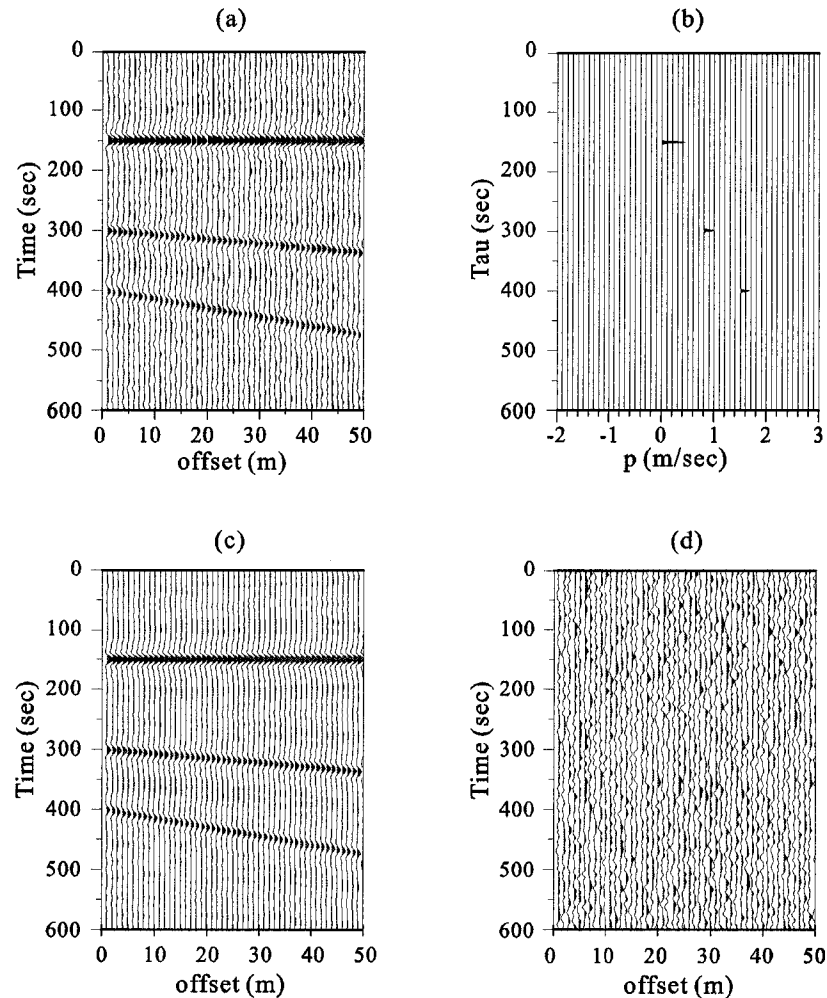
Figure 2-2 An example of the non-quadratic Radon transform. (a) The same synthetic data as that in Figure 2-1(a). (b) The Radon signal solved in time domain by non-quadratic solution. (c) Reconstructed data from the Radon signal in (b). (d) The difference between original data (a) and reconstructed data (c).

Since the Radon transform is solved as an inverse problem, the trade-off parameter μ is important for stabilizing the solution. There are many methods for trade-off parameter selection, such as the L-curve and χ^2 method. In this thesis, the turning point in the L-curve is chosen as the optimal trade-off parameter [*Engl* and *Grever*, 1994]. For exam-

14

ple, the L-curve in Figure 2-3 is used to choose optimal damping parameter μ for the case shown in Figure 2-1, where μ is about 9.
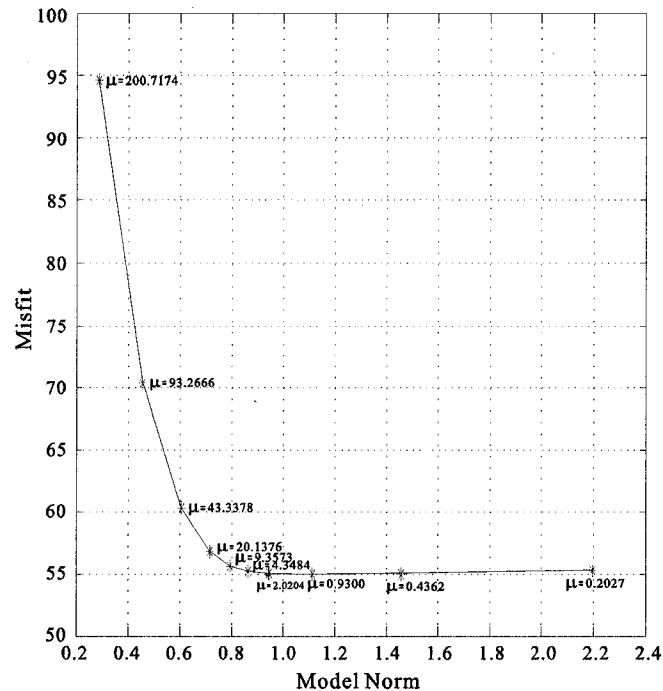
Figure 2-3 The L-curve used to choose damping parameter μ for the case shown in Figure 2-1.

2.4 Properties of the Radon transform

The Radon transform is a popular method in seismic imaging which can be used in velocity analysis [*Hampson*, 1986], noise attenuation [*Foster* and *Mosher*, 1992] and data interpolation [*Trad et al.*, 2002]. In this thesis, the filtering and interpolation properties are used to process tele-seismic data.

2.4.1 Filtering

One of the most important properties of the Radon transform is that it can attenuate non-coherent noise and coherent signals, such as multiples and undesired arrivals. Radon signals can be filtered to exclude undesired ray-parameters before mapping Radon signals back to the spatial domain, which is more useful in separating seismic arrivals.

15

Here I present an example of suppressing non-coherent noise and coherent signals, especially undesired arrivals. The synthetic data are shown in Figure 2-4(a) with four linear arrivals. The fourth arrival has an apparently different slop, which we consider it as an interfering arrival. By projecting the data to Radon domain with time domain non-quadratic method, four corresponding sparse points are shown in Figure 2-4(b). To attenuate the fourth arrival, there are two methods. One is filtering out the fourth point from the Radon signal in Figure 2-4(b), and the filtered result is shown in Figure 2-5(a); the other is mapping three interesting arrivals to the Radon domain directly [Figure 2-5(b)] by choosing the p range accordingly. By reconstructing the input data with the Radon operator in Figure 2-5(a) and (b), three arrivals [Figure 2-5(c)] are reproduced; while the fourth arrival is attenuated and presented in the residual plot [Figure 2-5(d)].
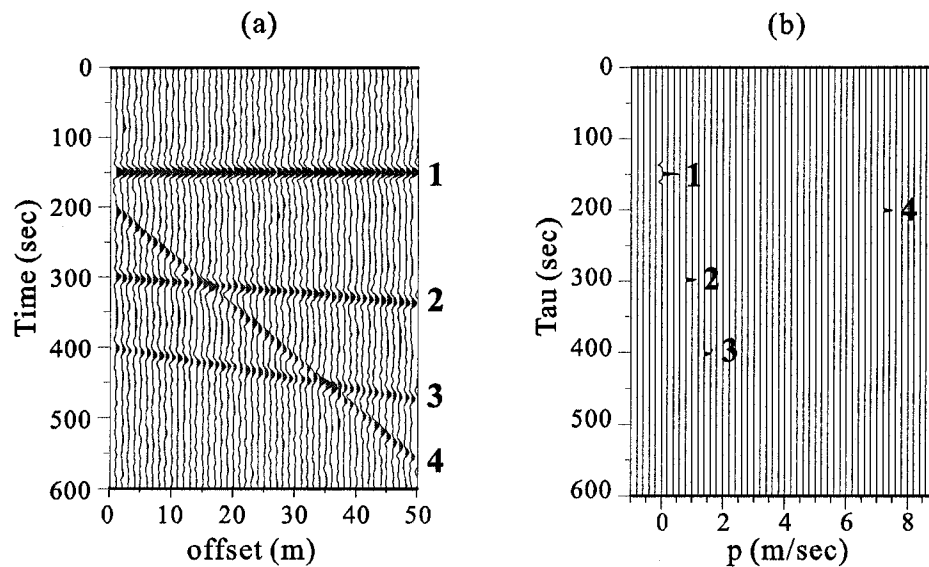
Figure 2-4 The high resolution Radon transform of a synthetic data set. (a) The synthetic data contain random noise and one undesired signal (the fourth arrival). (b) The non-quadratic Radon signals solved in time domain.
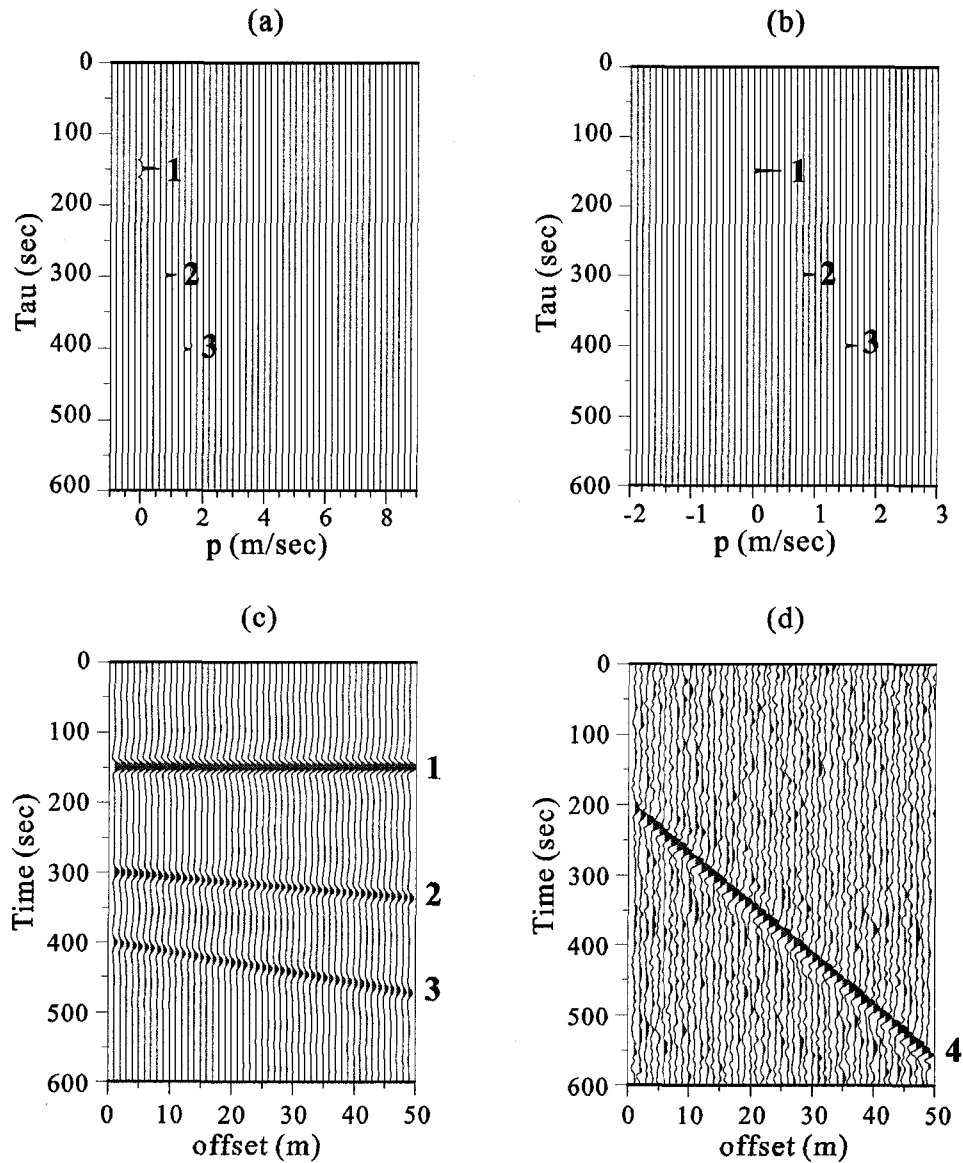
Figure 2-5 The filtering property of Radon transform. Non-coherent noise and undesired signals are attenuated with the filtered Radon signal. (a) The fourth point is filtered out from the Radon signal in Figure 2-4(b). (b) The non-quadratic Radon signals of three interested arrivals. (c) Reconstructed data without noise and the uninterested arrival. (d) The residual of original data in (a) and the reconstructed data in (c).

17

2.4.2 Resampling and interpolation

With Radon transforms, one can resample and interpolate the input data while reconstructing the data using the Radon operator. This property is especially useful in global seismology where unevenly sampled seismograms in the spatial domain are inevitable due to the unevenly distribution of earthquakes and stations.

We have two operators: one to compute the Radon transform, the other to reconstruct the data. In other words, we have a pair of transforms:

$$\begin{cases} \mathbf{u} = (\mathbf{L}^T\mathbf{L} + \mu\mathbf{I})^{-1}\mathbf{L}^T\mathbf{d} \\ \hat{\mathbf{d}} = \mathbf{L}\mathbf{u} \end{cases} \tag{2.22}$$

Notice that the reconstructed data are indicated by $\hat{\mathbf{d}}$. One can use two different operators to evaluate the Radon transform using the original data aperture $\mathbf{L}_o$ and, another to resample the data to a new spatial position $\mathbf{L}_r$. In this case, the pair of operators is given by

$$\begin{cases} \mathbf{u} = (\mathbf{L}_o^T\mathbf{L}_o + \mu\mathbf{I})^{-1}\mathbf{L}_o^T\mathbf{d} \\ \hat{\mathbf{d}} = \mathbf{L}_r\mathbf{u} \end{cases} \tag{2.23}$$

Equations (2.23) are used to resample and interpolate data in spatial domain.

Figure 2-6 illustrates the resampling and interpolation property of the Radon transform. The input data contains three arrivals while they are unevenly sampled in spatial domain [Figure 2-6(a)]. With the time domain high resolution Radon signals in Figure 2-6(b), one can reconstruct the data with the same spatial position [Figure 2-6(c)] or reconstruct it with a new uniformly sampled spatial position [Figure 2-6(d)]. Notice that the signals in Figure 2-6(d) show better resolution than these in Figure 2-6(c) due to the resampling and interpolation.

18
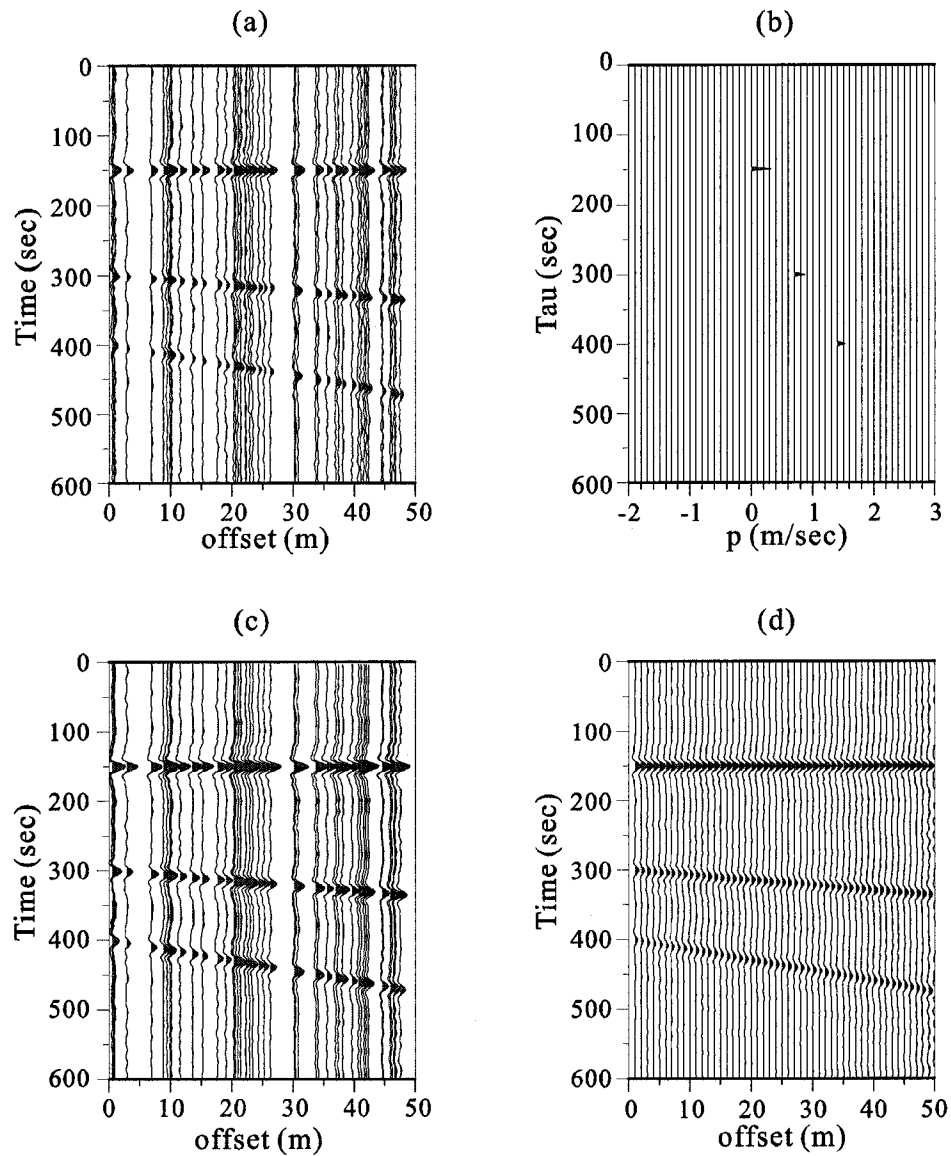
Figure 2-6 The interpolation property of Radon transform. (a) The synthetic data which are unevenly sampled in space domain. (b) The non-quadratic Radon signals. (c) Reconstructed data without resampling. (d) Reconstructed data with resampling and interpolation.

19

2.5 Comparison of the Radon transform and the Vespa process

One of the most commonly used methods in global seismology is Vespa process [*Rost and Thomas*, 2002] or slowness slant stack [*Gossler* and *Kind*, 1996], Comparing the Vespa process with the Radon transform discussed above, it should be noted that they are two related methods: the Vespa process is the low resolution Radon transform. To make it clear, let's introduce the Vespa process/slowness slant stack first.

2.5.1 The Vespa process/slowness slant stack and the Nth root process

The Vespa process (velocity spectral analysis) is originated by *Davies et al.* [1971]. The Vespa process estimates the seismic energy arrivals for a fixed back azimuth and different horizontal slownesses which is also called slowness slant stack (SSS); alternatively, it can be used for a fixed slowness and varying back azimuths. The result of the Vespa process is displayed as a Vespagram, which is a diagram showing the amplitude energy of signals as a function of slowness/back azimuth and time. The Vespa process is effective in separating arrivals with different slownesses or finding the right back azimuth for a beam forming. However, the limitation is obvious that the slowness resolution is poor and not always sufficient to separate arrivals with very similar slownesses [*Rost* and *Thomas*, 2002].

Due to the limitation of the Vespa process, the Nth root process is sometimes used to enhance the resolution in slowness. The Nth root process sums up the Nth root of M traces and then takes the summation to the Nth power. In some senses, the Nth root process can suppress incoherent noise, amplify the coherent signals and enhance the slowness resolution. However, the Nth root process is nonlinear, which will distort the waveform of signals.

2.5.2 The relation between slowness slant stack and the Radon transform

When used for a fixed back azimuth and varying slownesses, the Vespa process is also called slowness slant stack and can be calculated by:

$$v_u(t) = \frac{1}{N} \sum_{k=1}^{N} d_k(t - t_{u,k}),$$ (2.24)

20

where $d_k(t)$ represents the seismogram at station k, $t_{u,k}$ represents the relative travel time to station k for horizontal slowness u, and N represents the number of array stations.

Here, recall that low resolution Radon transform presented by equation (2.6) in chapter 2.1,

$$\tilde{u}(\tau, p_j) = \sum_{k=1}^{N} d(t = \tau + p_j x_k, x_k).$$

It is obvious that the slowness slant stack expression (2.24) and the low resolution Radon expression (2.6) are the same except the constant scalar $1/N$. That is to say, the slowness slant stack is a low resolution Radon transform. However, in this study, we didn't use equation (2.6) to solve the Radon problem; instead, we adopt the forward Radon transform (equation 2.7) and solved it as an inverse problem,

$$d(t, x_k) = \sum_{j=1}^{M} u(\tau = t - p_j x_k, p_j).$$

The Radon operator u solved from equation (2.7) is different from equation (2.6).

Using matrix notation to rewrite the adjoint pair (2.6) and (2.7) as follows,

$$\tilde{u} = L^T d, \tag{2.25}$$

$$d = Lu. \tag{2.26}$$

The operators L and L^T form an adjoint pair. The matrix L is the forward operator and L^T denotes the adjoint operator. The vector u indicates the Radon signal and the vector d indicates the data. Equation (2.25) represents the low resolution Radon transform or slowness slant stack. Equation (2.26) can be solved as an inverse problem and the damped least-squares (DLS) solution is

$$u_{dls} = (L^T L + \mu I)^{-1} L^T d. \tag{2.27}$$

It is obvious that if we denote $u_{sss} = L^T d$, then

$$u_{dls} = Gu_{sss}, \tag{2.28}$$

where $G = (L^T L + \mu I)^{-1}$ is the resolution matrix with Toeplitz form. Equation (2.28) illustrates the relation and difference between the least-squares Radon transform and the slowness slant stack. That is to say that the inverse procedure provides solutions with higher resolution than that from slowness slant stack. In addition, the inverse Radon op-

21

erator can be used to reconstruct data, which is an advantage of the Radon transform over slowness slant stack.

Figure 2-7 illustrates the difference among the slowness slant stack, the least-squares Radon solution and the non-quadratic Radon transform with a synthetic data set. Figure 2-7(a) shows the synthetic data with three arrivals. The slowness slant stack results in Figure 2-7(b) have lower resolution than the least-squares solution in Figure 2-7(c) and the non-quadratic solution in Figure 2-7(d). The non-quadratic solution (Figure 2-7d) is dramatic in resolution without any artifacts. Figure 2-8 shows the same results as Figure 2-7, but panel (b), (c) and (d) are displayed as energy contour.
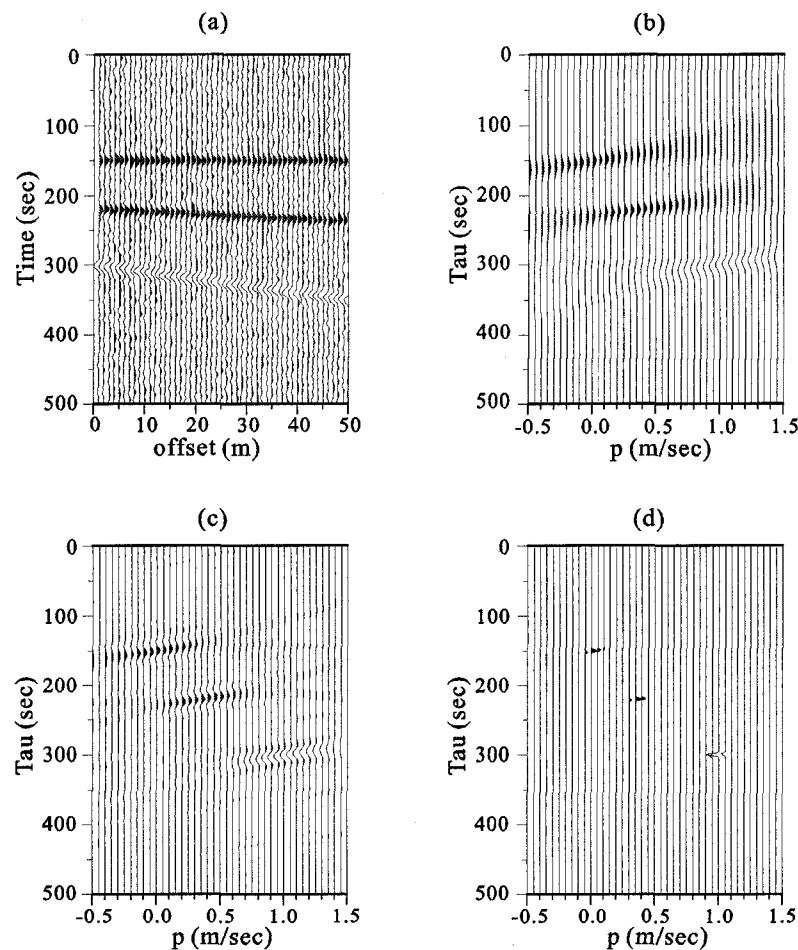
Figure 2-7 The comparison of slowness slant stack, the least-squares Radon solution and the non-quadratic Radon transform. (a) Synthetic data. (b) The results of slowness slant stack. (c) The least-squares Radon signal. (d) The non-quadratic Radon signal.

22
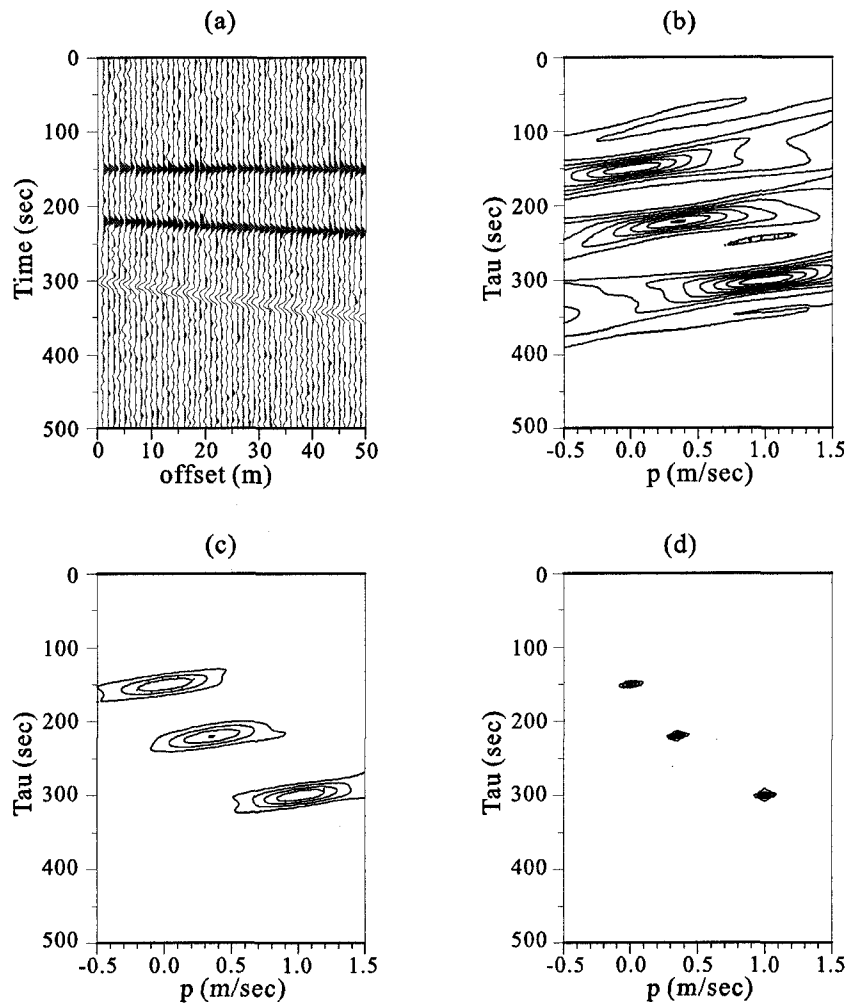
Figure 2-8 The comparison of slowness slant stack, least-squares Radon solution and the non-quadratic Radon transform, while the results are shown as energy contour. (a) Synthetic data. (b) The results of slowness slant stack. (c) The least-squares Radon signals. (d) The non-quadratic Radon signal.

23

2.6 Summary

Radon transform is a mature technique in noise attenuation, velocity analysis and data interpolation. In this chapter, I reviewed the concept of Radon transform and focused on the linear Radon transform. The time-invariant linear Radon transform can be computed in the time domain and frequency domain as well. Both implementations have been described and compared. The time domain implementation is flexible in choosing the integration path, while the frequency domain implementation can avoid the inversion of a large matrix computation. However, the frequency domain implementation can only impose constraints in the p domain; whereas, the time domain implementation can constrain both τ and p domains. Therefore, the time domain implementation is more accurate. In addition to the damped least-squares method to solve the linear Radon transform as an inverse problem, the non-quadratic regularization is presented and applied to generate high resolution Radon signals.

The Radon transform is superior in resolution than the traditional slowness slant stack, especially the non-quadratic method can produce high resolution Radon signal. In addition, the Radon transform allows for the reconstruction and interpolation of the original time series, which is more useful in global seismology due to the unevenly distributed earthquake and station. However, the Radon transform has pitfalls as well. Due to the limited aperture and sampling rate, artifacts and aliasing could be introduced to the Radon domain. Hence, proper choices of regularization parameters are critical in producing stable and sparse solutions.

24

Chapter 3

The Study of SS Precursors with the Radon Transform

To characterize transition zone (TZ) discontinuities, different reflected and converted wave groups have been employed. The most frequently analyzed phase groups are long-period waves, such as *SS* precursors [e. g., *Shearer* and *Master*, 1992; *Shearer*, 1993; *Gossler* and *Kind*, 1996; *Gu et al.*, 1998; *Flanagan and Shearer*, 1998; *Gu* and *Dziewon-ski*, 2002], *PP* precursors [e.g., *Flanagan* and *Shearer*,1999; *Chambers et al.*, 2005], *P'P'* precursors [e. g., *Benz* and *Vidale*, 1993; *Xu et al.*, 1998]. *SS* precursors remain one of proven means for identifying and interpreting mantle reflectors, since these weak underside reflections are highly sensitive to both depth and reflectivity of mantle reflectors. In this chapter, I apply Radon transforms to *SS* precursors to test the feasibility of Radon transform in global seismology.

25

3.1 Data selection and preprocessing

3.1.1 SS precursors

SS precursors are the mild underside reflections from mantle discontinuities which arrive as precursors to the main *SS* arrival. They are strongly sensitive to the structure beneath *SS* reflection point and less related with unevenly distributed sources and stations. *SS* precursors are termed *SdS*, where *d* stands for reflection depth, for example, the underside reflection from 400 km is denoted *S400S*. Figure 3-1 illustrates the ray geometry of *SS* and its precursors propagating through a spherical Earth model of radially varying velocity. Differential travel times between *SS* and its precursors can be used to detect the subtle structural perturbation between the surface and the reflected depth. To study *SS* precursors, the broad band long-period *SH* component of seismogram is used.

Long-period *SS* precursors will average structure around the geometric ray path due to the broad sensitivity of the Fresnel zone. Fresnel zone is the region where a ray scatters from a single point and arrives at the receiver within 1/4 of the dominant period of the direct waveform. *SS* precursors have a complex Fresnel zone of about 1000 km [*Neele at al.*, 1997] if the dominant period is 20 sec. Such large size of Fresnel zone can lead to underestimate in discontinuity topography [*Deuss*, 2007], especially when the topography has a smaller scale variation.

26

(a)

(b)
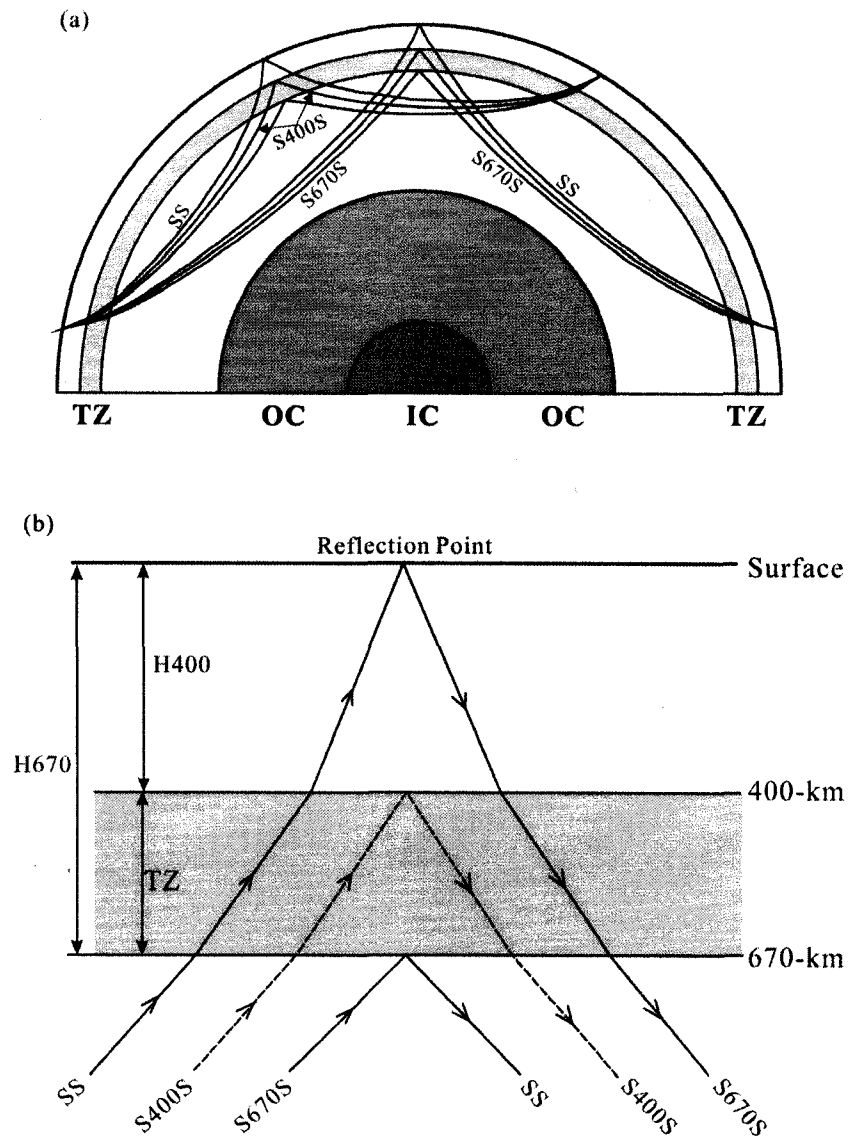
Figure 3-1   The ray geometry of *SS* and its precursors.

3.1.2 Data selection criteria

In this research, we utilize more than 10 years of long-period broadband tele-seismic data archived by GDSN, IRIS, GEOSCOPE and other seismic networks. The synthetic seismograms are generated with PREM [*Dziewonski* and *Anderson, 1981*] for each source and receiver pair.

27

To ensure the quality of dataset, we select records from shallow events (<45 km) to minimize the interference from depth phases (e.g., sSS). Only events with moment magnitude Mw > 5.0 are considered to provide a good signal-to-noise ratio (SNR); and the epicentral distance is restricted to 100°-160° to minimize potential waveform interference from ScS precursors $ScSdScS$ and topside reflections $sdsS/sdsS_{diff}$ [$Schmerr$ and $Garnero$, 2006], where d represents a discontinuity depth. From synthetic seismograms shown in Figure 3-2, the interfering waveforms from $ScSdScS$ and $sdsS/sdsS_{diff}$ are clearly identified. The data are filtered with a Buttersworth band pass filter with cut off period at 15 sec and 75 sec. The filtered data are subjected to a SNR-based selection criterion (defined by the energy ratio between SS and its proceeding "noise" level). All records with SNR lower than 3.0 are automatically rejected; therefore, the seismogram with lower SNR, for example, seismogram 4 (SNR=0.99919) in Figure 3-3, is rejected. We improve the accuracy further by interactively inspecting all seismograms using a MATLAB-based visualization and stacking code (Figure 3-3). Seismogram 3 in Figure 3-3 is rejected from the dataset due to lower frequency signals in the target region. The polarity of a given seismogram is reversed if necessary to account for potential instrument misorientation [$Shearer$, 1993].
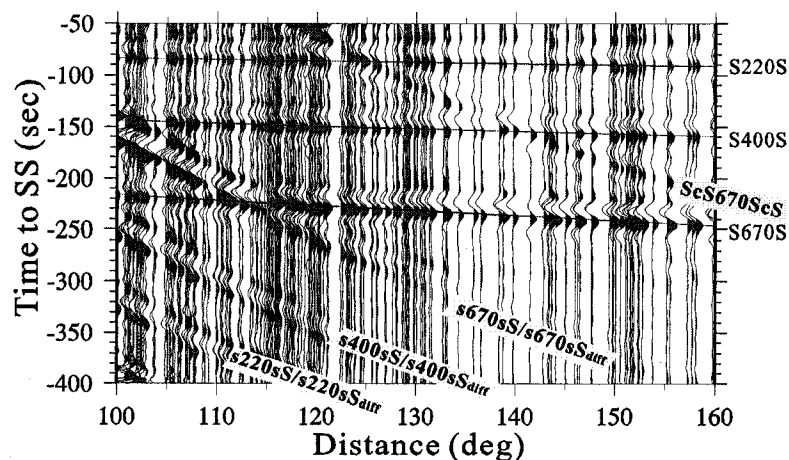
Figure 3-2 Waveform interferences from $ScSdScS$ and $sdsS/sdsS_{diff}$ are clearly identified from synthetic seismograms.

28
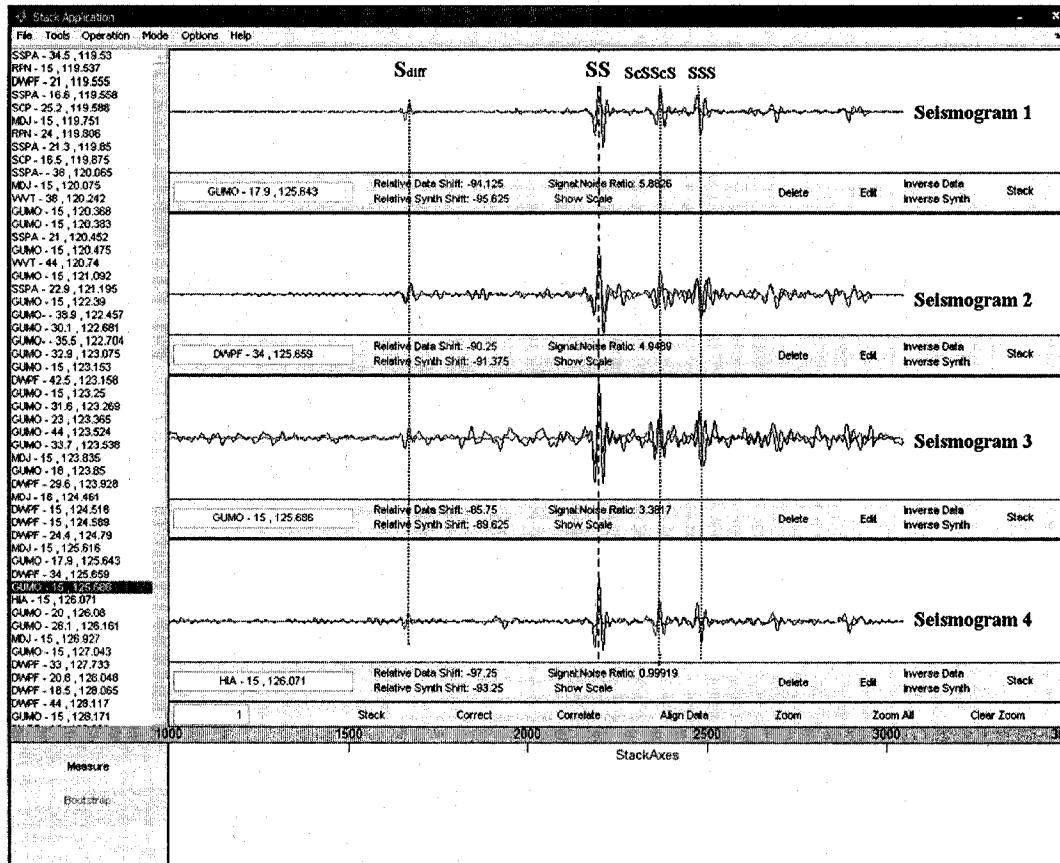
Figure 3-3 Interactive inspection of all seismograms with a MATLAB-based code. Seismogram 3 and 4 are rejected due to its low frequency and low SNR, respectively.

3.1.3 Corrections

Corrections are applied to the selected dataset to account for the effect of surface topography, crust thickness and mantle heterogeneity. Prior to correction, we align the first major swing of the reference phase SS and normalize each record by its maximum absolute amplitude to equalize the source effect. After alignment and normalization, corrections are performed. The effects of surface topography and crust thickness at reflection points are computed from ETOPO5 (distributed by the National Geophysical Data Center) and CRUST2.0 [*Bassin et al.*, 2000], respectively. The heterogeneity correction is computed from the shear wave velocity model S12_WM13 [*Su et al.*, 1994]. However, we do not correct for epicentral distance as did in earlier studies of SS precursors [*e.g., Shearer*, 1993; *Gu et al.*, 1998; *Flanagan and Shearer*, 1998; *Duess* and *Woodhouse*, 2002]; since

29

the distance-time relationship is an integral part of the Radon analysis. We then multiply each record by the square root of its SNR to increase the weight of high-quality records.

3.2 Radon tests with synthetic seismograms

3.2.1 Theoretical travel time curves

The SS precursor dataset is more complicated than the simulated dataset examined in chapter 2.3. In general, seismograms are irregularly sampled in space domain due to the uneven distribution of earthquakes and stations on the Earth. Because each record has been aligned to SS, the travel times of remaining phases become relative (or corrected) times to SS; similarly, the ray parameters of the remaining phases become differential ray parameters to that of SS. To determine the feasibility of the Radon transform algorithm for this dataset, we first fit the theoretical relative travel times (calculated from PREM) of $S220S$, $S400S$ and $S670S$ using 2nd order polynomials (Figure 3-4). These travel time curves are approximately linear and the coefficients of quadratic terms are about 500 times smaller than those of respective linear terms. We keep the quadratic term by adopting an empirical scaling factor of -0.002 times linear term coefficient to accurately fit travel time curves.
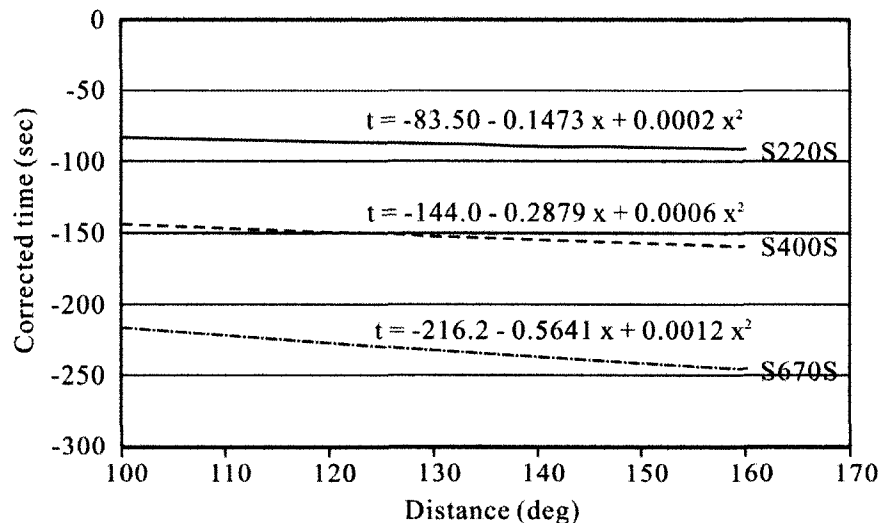
Figure 3-4   The differential travel time curves for SS precursors, which are calculated based on PREM.

30

The travel time equation can be written as follows:

$$t = \tau + px + \alpha px^2, \tag{3-1}$$

where $\alpha = -0.002$ is the scaling factor, x is the distance in $t - x$ domain, τ is the differential intercept time in the Radon domain, and p is the relative ray parameter to that of SS. In this research, equation (3-1) is used to be the summation path, rather than a linear path, for the Radon transform.

3.2.2 Radon tests with synthetic SS precursors

With synthetic data, we tested the validity of damped least-squares Radon transform (LSRT) and non-quadratic Radon transform (NQRT) using the summation path presented in equation (3-1). Figure 3-5 shows the synthetic seismograms (calculated based on PREM) after aligning on and normalizing by SS for Hawaii hotspot (20°N, 204°W) with 10° geographic bin size. Three arrivals resulting from underside reflections of 220-, 400- and 670-km discontinuities are clearly identified. Also, undesired interferences from $ScSdScS$ and the topside reflection $sdsS/sdsS_{diff}$ are identified.

The damped least-squares method is applied to solve the Radon problem. The Radon signals of the Hawaii synthetic seismograms are shown in Figure 3-6(a). Three well-defined energy maxima with relative p values of -0.184, -0.268 and -0.519 sec/deg correspond to $S220S$, $S400S$ and $S670S$ in the time domain, respectively. The intercept time τ is the relative travel time to SS at 100° epicentral distance. Once a $\tau - p$ model is obtained, it can be used to reconstruct data in the time domain. Figures 3-6(b) shows recovered $t - x$ domain signals. To certain extent, random noise and interfering phases $ScSdScS$ and $sdsS/sdsS_{diff}$ are attenuated. The Radon transform is also an efficient interpolator [*Sacchi* and *Ulrych*, 1995], which can be used to extend the aperture and fill gaps. When we transform Radon operator back to $t - x$ domain, interpolation can be performed at the same time. Figure 3-6(c) shows the reproduced time domain signals after spatial resampling and interpolation. The interpolated time series have higher quality than the original ones due to the removal of noise and gaps in data coverage. The residuals in Figure 3-6(d) show some incoherent noises and interferences from $ScSdScS$ and $sdsS/sdsS_{diff}$.

31

By limiting the range of the ray parameter, we can limit the number of arrivals to be mapped in the $x-t$ domain. In other words, limiting the range of the Radon parameter or filtering the Radon signals in the $\tau - p$ domain will eliminate undesired events. The ability to eliminate such interfering arrivals outside the $\tau - p$ range of interest is one of the key advantages of the Radon transform.
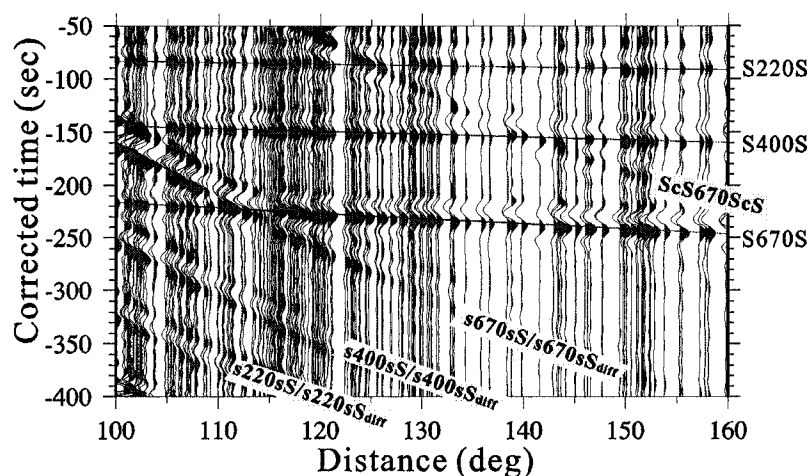
Figure 3-5   The synthetic seismograms from Hawaii hotspot.
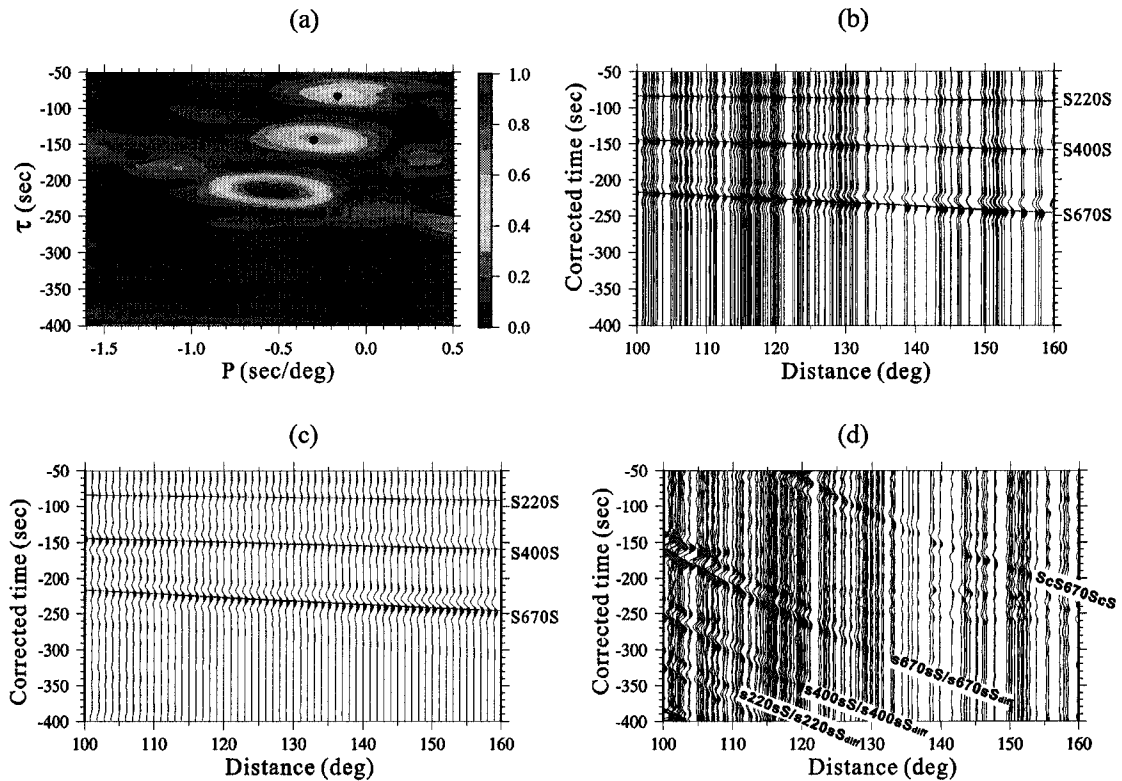
Figure 3-6   The least-squares Radon transform of synthetic data from Hawaii hotspot. (a) The damped least-squares Radon results of the synthetic seismograms in Figure 3-5, which is plotted as energy envelopes. The solid dots denote the peak $\tau - p$ values of Radon signals. (b) The reconstructed time series. Undesired reflections and random noise are strongly attenuated. (c) The Reproduced time series after resampling and interpolation. (d) The residual between the original and the predicted time series.

The non-quadratic Radon transform is performed to the same synthetic dataset. Figure 3-7(a) displays the non-quadratic Radon signals of the Hawaii dataset. The energy is highly focused on three points which correspond to $S220S$, $S400S$ and $S670S$. Notice that the resolution of these Radon signals is much better than that in Figure 3-6(a) calculated with damped least-squares method. With this high resolution Radon signals, much cleaner time series are reconstructed in Figure 3-7(b) and Figure 3-7(c). The residuals in Figure 3-7(d) show similar interfering arrivals and incoherent noise as these in Figure 3-6(d).

33
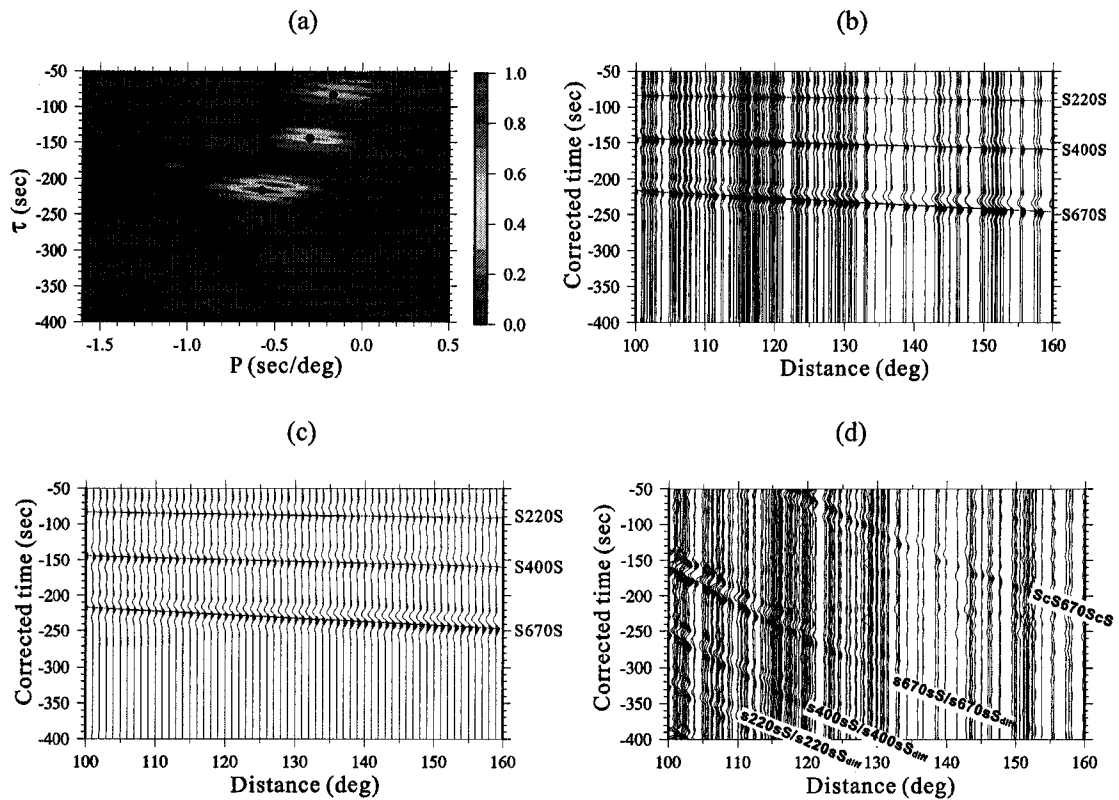
Figure 3-7   The non-quadratic Radon transform of synthetic data from Hawaii hotspot. (a) The non-quadratic Radon signals for the synthetic seismograms, which are plotted as energy envelopes. The solid dots denote the peak $\tau - p$ values. (b) The reproduced time series. Undesired reflections and random noise are highly attenuated. (c) The Reconstructed time series after resampling and spatial interpolation. (d) The residual between the original and the predicted time series.

Also, the low resolution Radon signal or the slowness slant stack is computed and presented in Figure 3-8. The resolution of the slowness slant stack results in time domain is compatible with the Radon signals in Figure 3-6(a) calculated with damped least-squares method; however, the ray parameter has lower resolution. Compared with the high resolution Radon signals in Figure 3-7(a), the slowness slant stack results show fairly lower resolution in the $\tau - p$ domain.

34

Figure 3-8   The low resolution Radon signal/slowness slant stack results of synthetic seismograms from Hawaii hotspot. The results are plotted as energy envelopes. The solid dots represent the peak $\tau - p$ values from damped least-squares Radon signals.

3.3 The Radon transform applied to broadband SS precursors

In theory, the Radon transform can be directly applied to the reflections and conversions from mantle discontinuities. With real seismic records, however, other aspects come into play. The presence of noise and other non-ideal conditions make the final solutions very different. In practice, the recorded SS precursors often require additional signal enhancement due to the presence of correlated/random noise and incomplete data coverage. Figure 3-9 shows the preprocessed data from the Hawaii hotspot where $S400S$ and $S670S$ are nearly indistinguishable from surrounding noise. Without preconditioning, the non-quadratic procedure cannot effectively project the time domain recordings to Radon domain (Figure 3-10), and the scatter in Radon domain is as severe as it is in the time domain.

35
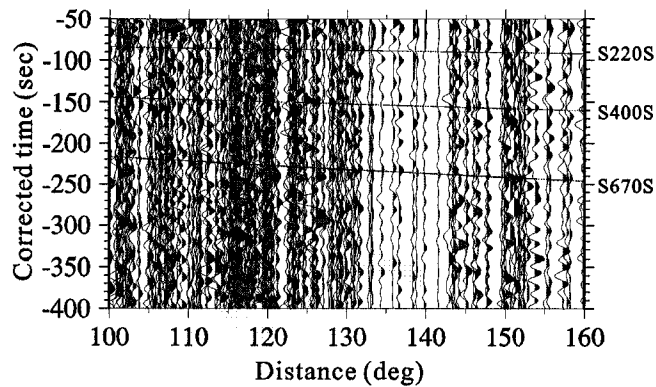
Figure 3-9   Unconditioned seismic recordings for Hawaii hotspot. The reflections from mantle discontinuities are buried in the background noise.
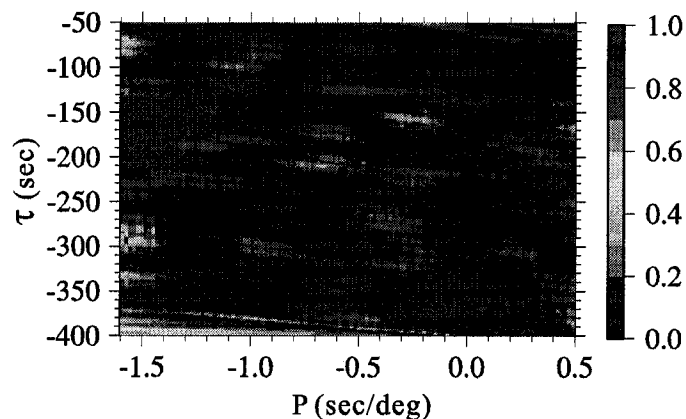
Figure 3-10   The non-quadratic Radon results of the unconditioned seismograms (Figure 3-9). No recognizable pattern is detected. The black dots denote the theoretical $\tau - p$ values from synthetic seismograms for $S220S$, $S400S$, and $S670S$, respectively.

We precondition the data by partially stacking SdS along the theoretical differential travel time curve of $S400S$-SS and $S670S$-SS calculated from PREM [*Dziewonski* and *Anderson*, 1981] for a distance window of 20°. The stacking result is an effective running average of records within a window. The window size dictates the amount of smoothing. The choice of a 20°-30° stacking window is superior to common approaches such as slowness slant stacking that typically averages the entire distance range [*Gossler* and

36

Kind, 1996] and strikes a reasonable balance between signal coherence and data resolution.

Figure 3-11 shows the partially stacked traces of original data (Figure 3-9) with a spatial averaging distance of 20°. The observed differential travel time curve of *S400S-SS* shows a jump around 120°. To make the Radon transform eligible to this problem, we apply the Radon transform to the dataset between 120°-160° in distance. The improvement of time domain SNR substantially enhances energy focusing of Radon signals calculated with damped least-squares method [Figure 3-12(a)]. Two peaks are identified which correspond to *S400S* and *S670S*, respectively. These values are consistent with PREM predictions (denoted by black dots). Two weaker peaks are likely associated with secondary discontinuities in the mantle. The reconstructed data in Figure 12(b) and (c) are consistent with those original partially stacked data.

The non-quadratic Radon signals of the same partially stacked data are presented in Figure 3-13(a). The latter shows higher resolution in the Radon domain than the Radon signals in Figure 3-12(a) computed with the damped least-squares method. The reconstructed data (with and without resampling and interpolation) show an improvement of SNR of the time series.
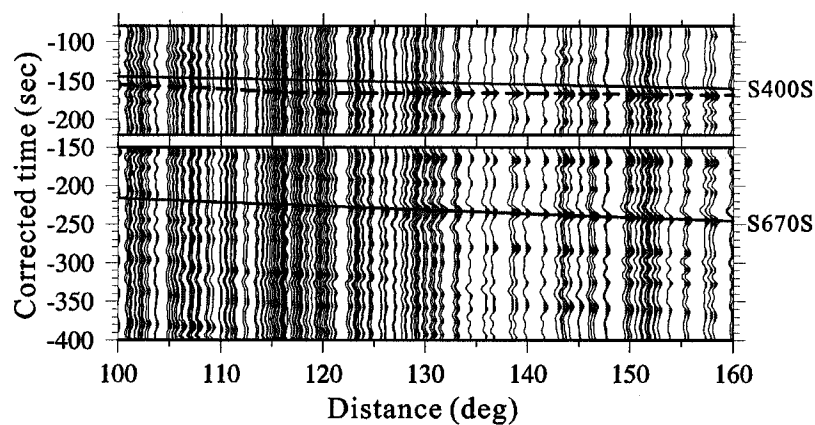
Figure 3-11 The same time series as Figure 3-9 after partial stacking (20°) along theoretical relative ray parameter calculated from PREM for *S670S-SS* and *S400S-SS*. The solid line represents the theoretical differential travel time curve. The dash line denotes the observed travel time curve after partial stacking.

37
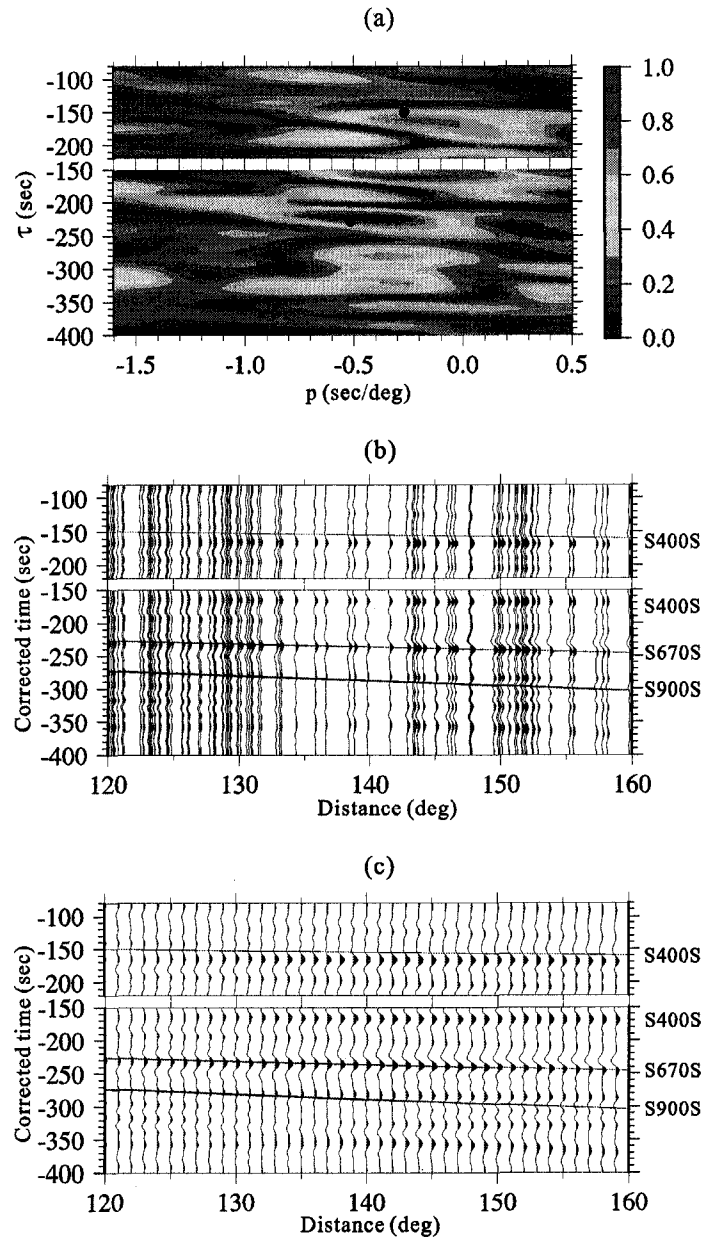
Figure 3-12   (a) The damped least-squares Radon signals of the partially stacked data, which are shown as energy envelopes. The black dots denote the $\tau - p$ values from synthetic seismograms. (b) The reconstructed time series without resampling. (c) The reproduced time series after resampling and interpolation.

38
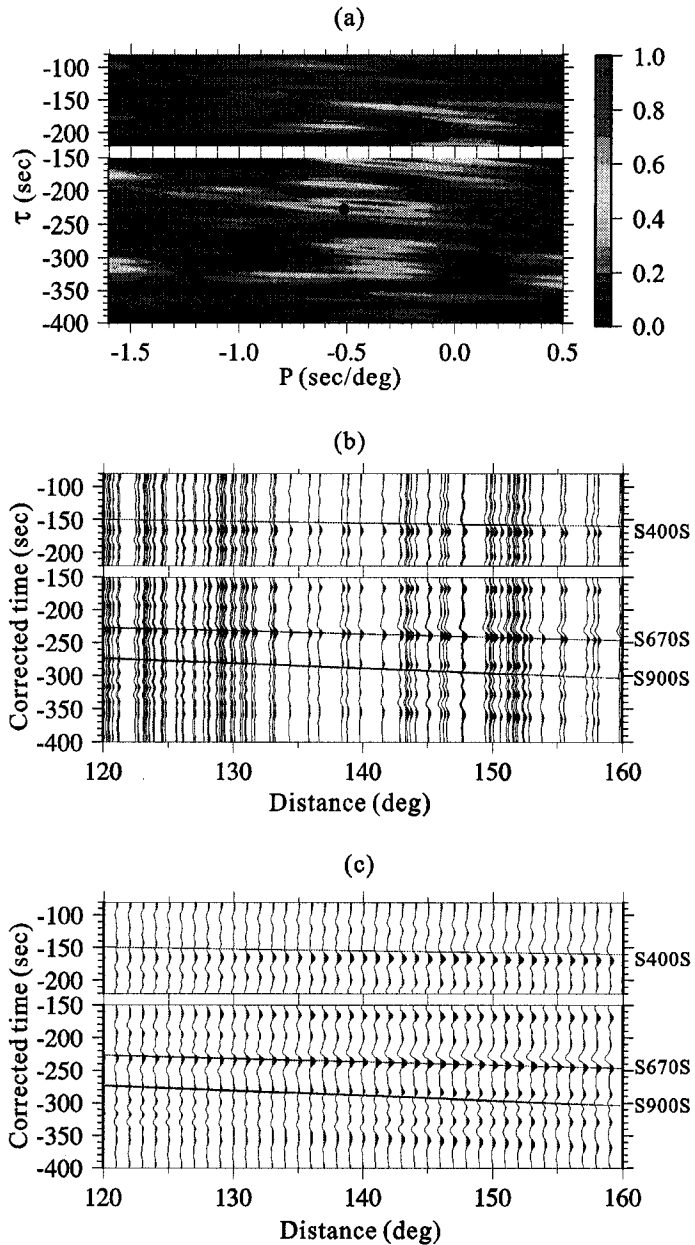
Figure 3-13   (a) The energy plot shows the non-quadratic Radon-domain signals of the partially stacked data (Figure 3-11). The black dots denote the $\tau - p$ values from synthetic seismograms. (b) The reconstructed time series without resampling. (c) The reproduced time series after resampling and interpolation.

39

3.4 Concluding remarks

The formulation of the Radon transform provides mechanisms for signal enhancement, noise attenuation and interpolation. First, by adjusting the trade-off parameter, one can control the degree of fitting to the original data with the data generated from the forward Radon operator. Second, once a $\tau - p$ model is obtained, the forward transform can be applied to reproduce the time domain data, as well as to resample and interpolate them. Spatial interpolation is particularly useful considering that gaps in data coverage are often prevalent in earthquake recordings. Finally, the Radon transform can be used to remove interfering arrivals with vastly different $\tau - p$ values by filtering the data in the Radon domain. These properties make the Radon transform effective in differentiating small seismic phases of interest from SS precursors and in attenuating random noise or scattered waveforms.

40

Chapter 4

Imaging Mantle Discontinuities

In this chapter, I focus on the application of the Radon transform to image mantle discontinuities. The damped least-squares method is used to solve the Radon transform. The effectiveness of the Radon transform is fully assessed for the analysis of long-period SS precursors. All the possible seismic discontinuities, including transition zone discontinuities, across the northeastern Pacific Ocean and the northwestern Canada, are delineated.

4.1 Introduction

The study profile is a cross section encompassing the northeastern Pacific Ocean and the northwestern Canada, which is particularly well sampled by SS reflection points in the distance range from 100° to 160°. Tectonically, this region constitutes landmasses of intermediate-to-young oceanic lithosphere, accretionary margins, and stable continental platforms. The diverse tectonic signatures invite a number of important scientific questions regarding the presence and nature of seismic discontinuities in the mantle.

In this study, I present regional observations and interpretations for all mantle discontinuities below 200 km to address, at least partially, some of the above questions. The damped least-squares method is used to solve the Radon transform and accurate $\tau - p$ values are obtained to infer depth variations of mantle discontinuities. The results reveal strong thermal variations beneath the selected profile and provide a glimpse of the uncanny potential of the Radon transform in mapping subsurface structures [*An et al.*, 2007].

4.2 Implementing the Radon transform to SS precursors

According to the selection criteria outlined in chapter 3.1.2, 402 high-quality records which encompass the northeastern Pacific Ocean and the northwestern Canada are retrieved. These datasets are further divided into seven 5-deg geographic bins along the great circle, connecting (155.335°W, 42.098°N) and (124.189°W, 66.859°N) (Figure 4-1). After alignment and normalization on SS, these datasets are further corrected for topogra-

phy, crust, and heterogeneity as outlined in Chapter 3.1.3. The cap size is dictated partly by the number of data for an effective analysis, and partly by the size of Fresnel zone (~1000 km for a 130-deg, 20 s SS wave). The overlap between any two caps introduces coherent spatial averaging across the study transact.
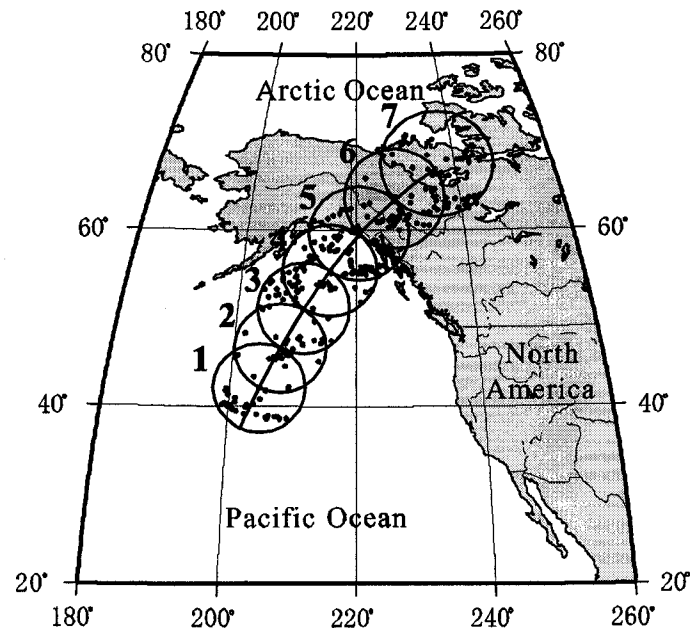
Figure 4-1   Cap locations of the study profile. There are seven 5-deg caps across the northeastern Pacific Ocean and the northwestern Canada. The black dots denote the reflection points of SS.

The Radon tests presented in chapter 3.2 and 3.3 illustrate the effectiveness of Radon transform to isolate differential travel time and ray parameter of SS precursors. Therefore, the damped least-squares Radon transform is performed to the synthetic and actual seismic records of these seven 5-deg caps, and the corrected intercept time τ and relative ray parameter p are tabulated in Table 1. The intercept time τ represents the distance-corrected differential travel time of SdS - SS at 100°. The observed $\tau - p$ deviations from those of synthetic seismograms reflect the arrival time perturbations relative to the PREM model.

42

Prior to the implementation of Radon transforms, partial stacking is performed for actual seismic data to improve SNR. An averaging distance of 30° is chosen as partial stacking window for the first two caps and 20° for the remaining caps. To ensure correctness, we analyze $S400S$ and $S600S$ separately and compare the partially stacked time series (left column in Figures 4-2 and 4-3) with the corresponding energy diagram in the Radon domain (right column in Figures 4-2 and 4-3). The Radon energy maxima accurately reflect the secondary arrivals proceeding to SS. More importantly, coherent phases outside of interest of this study, for example, the topside reflections $sdsS/sdsS_{diff}$ and ScS precursors, are effectively eliminated from the original time series through Radon-domain filtering. In addition, with the Radon operator, the time series can be reconstructed and interpolated, which is one of the key advantages of the Radon transform. Figure 4-4 explains the reconstruction and interpolation of time series using cap 7 as an example. In Figure 4-4, we also compare the damped least-squares Radon solution (Figure 4-4c) with slowness slant stack results (Figure 4-4d). The measurements of τ values from the energy maxima are consistent between Figures 4-4(c) and (d), and their resolutions are comparable. However, the resolution of the ray parameter is substantially improved by damped least-squares solution, see Figure 4-4(c).

43
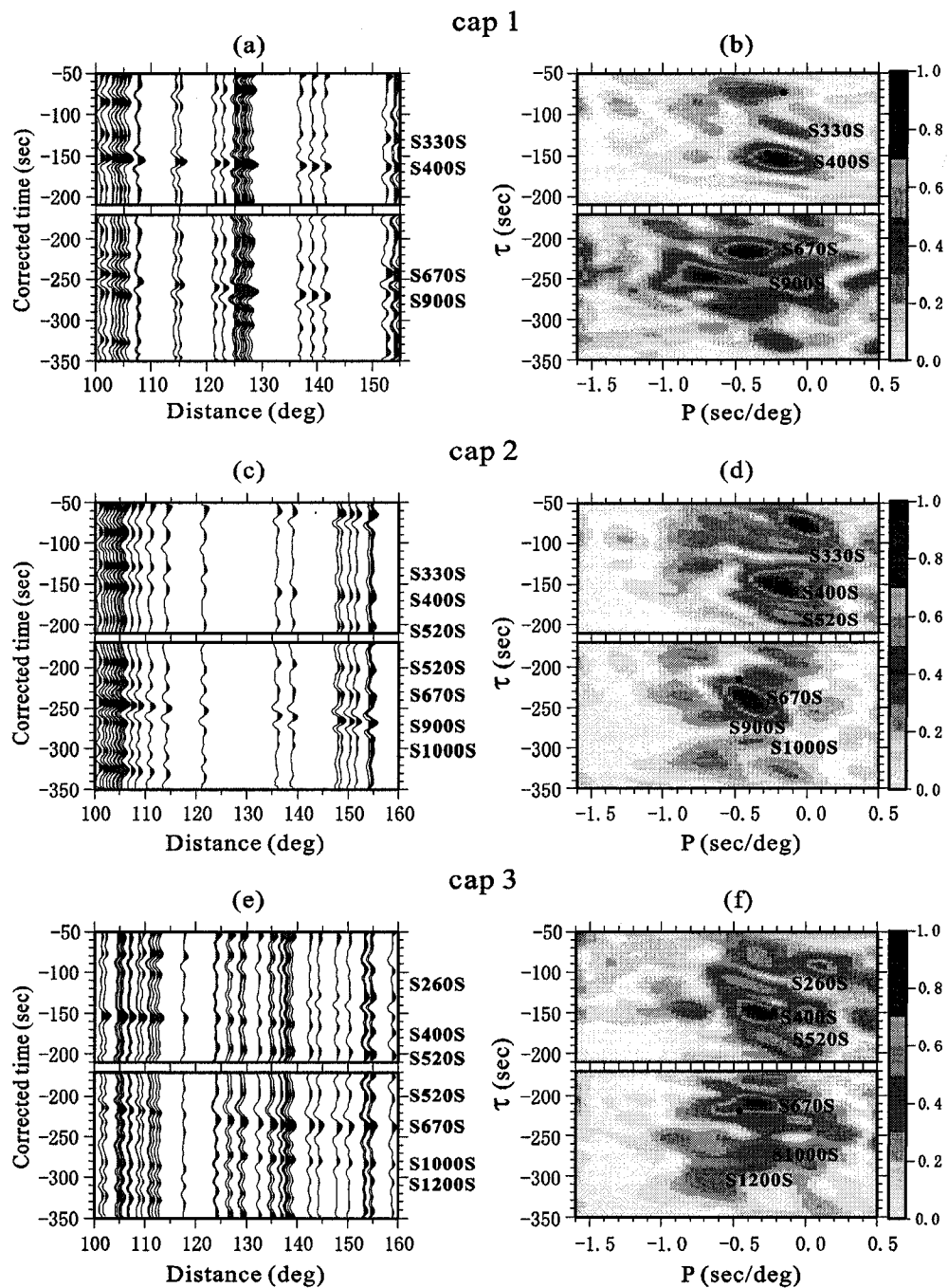
Figure 4-2   The time series for caps 1-3 after partial stacking are shown on the left-hand side and the corresponding Radon signals calculated with damped least-squares method are shown on the right column. The black dots in (b), (d) and (f) denote the theoretical $\tau - p$ values measured from Radon signals of corresponding synthetic seismograms.

44
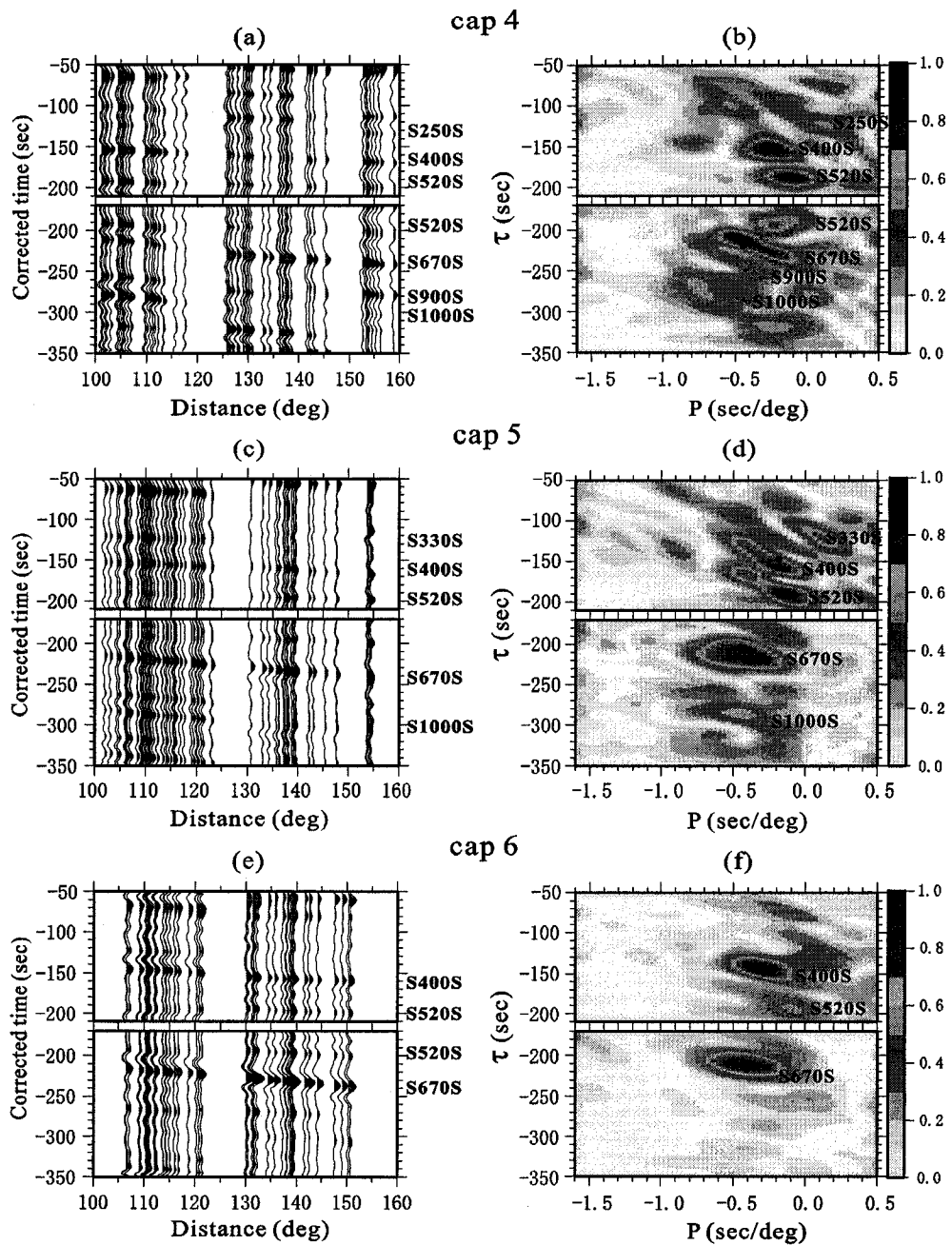
Figure 4-3 The partially stacked traces for caps 4-6 are shown on the left-hand side and the corresponding Radon signals calculated with damped least-squares method are shown on the right column. The black dots in (b), (d) and (f) denote the theoretical $\tau - p$ values measured from Radon results of corresponding synthetic seismograms.

45
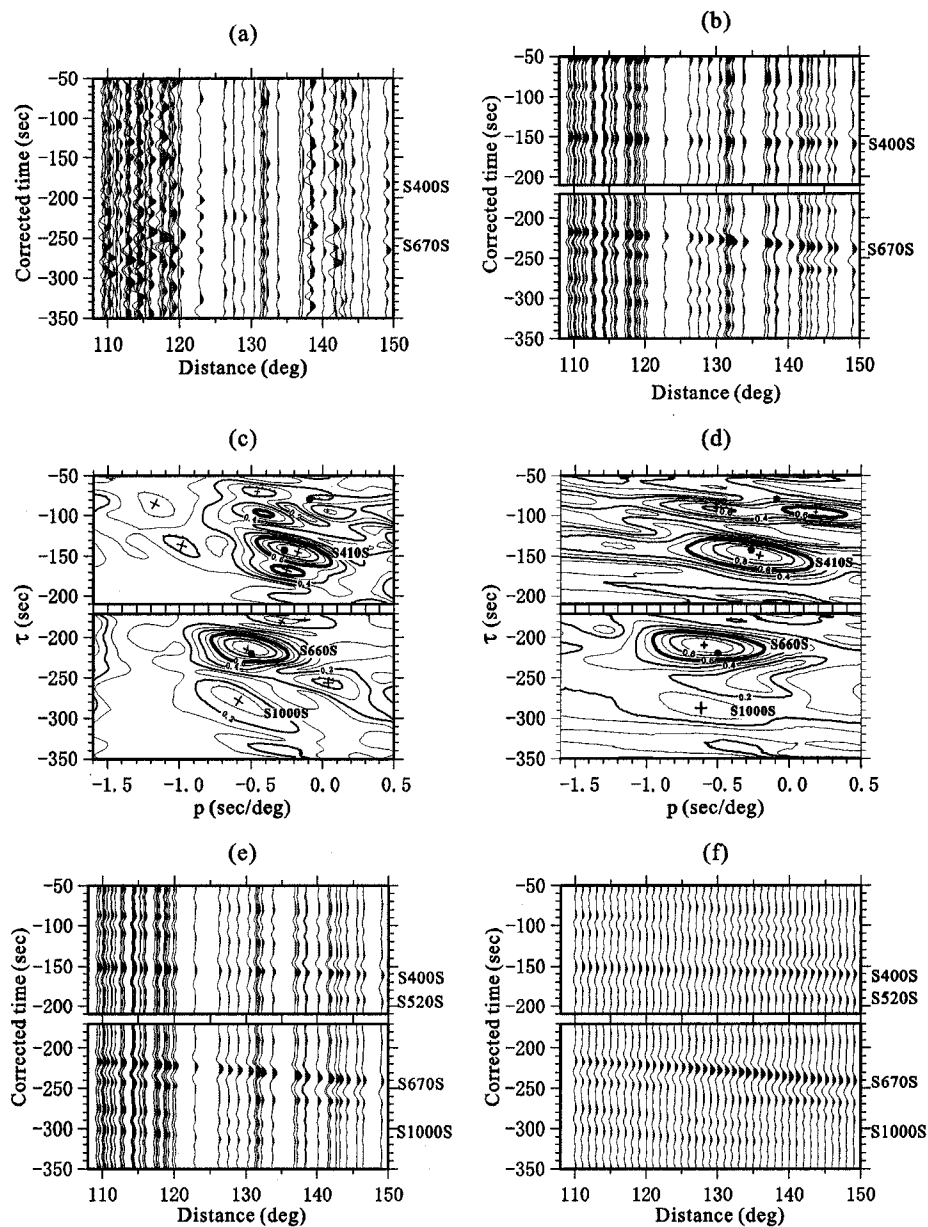
Figure 4-4 (a) The actual seismic records for cap 7. Phases $S670S$ and $S400S$ are contaminated by ambient noise. (b) The partially stacked (20°) time series for cap 7. (c) The Radon-domain signals of the partially stacked data which are calculated with damped least-squares method and shown as contour plot of the energy. (d) The slowness slant stack results of the partially stacked data (contour plot of the energy). The bold curves represent the same scale value (0.6). (e) The reconstructed time series without resampling. (f) The reproduced time series after resampling and interpolation.

46

| | location | | Number of traces | | S660S | | | | S410S | | | | TZ thickness (km) |
	latitude	longitude			Tau (sec)	P (sec/deg)	Depth (km)	Deviation (km)	Tau (sec)	P (sec/deg)	Depth (km)	Deviation (km)	
cap 1	42.098	-155.335	36	syn	-217.40	-0.426	667	2.36	-147.11	-0.278	415	0.40	252
				data	-216.98	-0.440			-155.15	-0.213			
				mean	-216.80	-0.443			-154.67	-0.225			
				deviation	4.14	0.040			0.91	0.012			
cap 2	46.630	-152.378	27	syn	-215.09	-0.474	658	0.89	-150.82	-0.277	418	0.62	240
				data	-213.09	-0.445			-154.04	-0.214			
				mean	210.77	-0.432			-152.68	-0.240			
				deviation	4.33	0.027			3.69	0.038			
cap 3	51.072	-148.884	57	syn	-218.27	-0.461	647	1.30	-148.05	-0.263	419	1.20	229
				data	-210.75	-0.349			-150.06	-0.333			
				mean	-209.32	-0.419			-148.79	-0.282			
				deviation	0.60	0.024			1.91	0.040			
cap 4	55.388	-144.660	70	syn	-219.00	-0.447	634	2.67	-151.59	-0.238	420	1.43	214
				data	-211.94	-0.488			-154.15	-0.266			
				mean	-211.74	-0.498			-153.97	-0.256			
				deviation	2.13	0.030			1.10	0.018			
cap 5	59.523	-139.424	95	syn	-217.75	-0.400	648	1.57	-147.87	-0.189	419	1.49	229
				data	-214.28	-0.427			-156.12	-0.212			
				mean	-212.51	-0.441			-148.97	-0.273			
				deviation	4.21	0.033			6.17	0.053			
cap 6	63.392	-132.779	57	syn	-215.99	-0.406	643	1.52	-143.83	-0.218	391	1.45	252
				data	-210.66	-0.427			-143.30	-0.335			
				mean	-211.52	-0.395			-141.00	-0.300			
				deviation	1.46	0.026			1.01	0.059			
cap 7	66.859	-124.189	60	syn	-219.03	-0.502	640	1.81	-146.84	-0.226	403	0.90	237
				data	-212.96	-0.505			-143.60	-0.206			
				mean	-215.32	-0.485			-142.81	-0.235			
				deviation	1.54	0.036			0.95	0.017			

Table 4-1   The Radon results, TZ depth and thickness of seven caps

4.3 Depths of TZ discontinuities

Differential travel times between the observed and PREM-based SS precursors represent depth perturbations of mantle discontinuities. The reconstructed data/synthetic seismograms are stacked along the best-fit travel time curves and collapsed to one representative distance of 100° (Figures 4-5) using the Radon transform. The travel time perturbations of $S400S$ are pronounced but only slight variations of $S670S$ are observed.
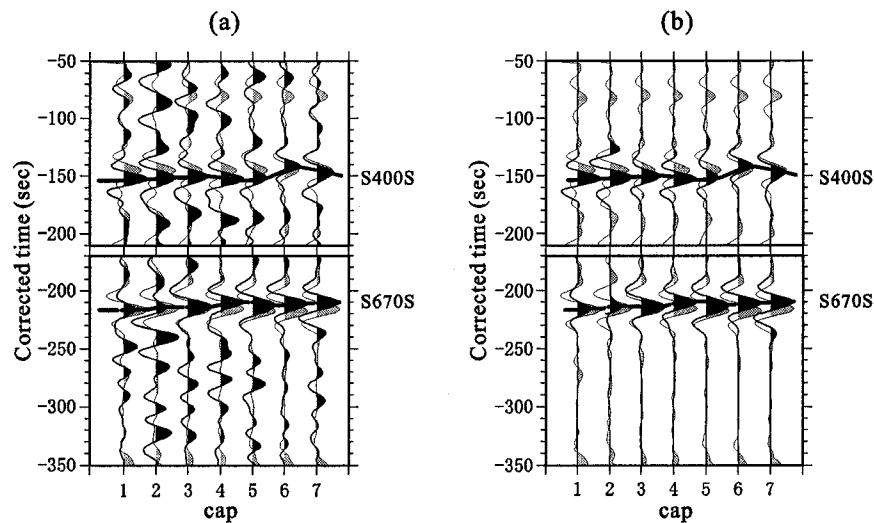
Figure 4-5   Cumulative stack for each cap based on measured ray parameter p for both synthetic (shown in grey) and observed seismograms (shown in black). To avoid inaccuracies in the stacking procedure, stacking is performed individually for $S400S$ and $S670S$ in each case. The two panels show the stacking results (a) without Radon-domain filtering and (b) with Radon-domain filtering.

By computing theoretical times of SS and SdS for a range of depths, we determine the depth that best matches the observed τ values. Figure 4-6 compares our migrated depth estimations of TZ discontinuities with those from *Flanagan & Shearer* [1998] and *Gu et al.* [2003] at similar locations. The topography maps are generally consistent with those from early studies, especially the 400-km discontinuity. However, the smaller-scale topography observed by this study, for example, at caps 4 and 6, are not present in the earlier studies.

48

Our depths span 29 km for 400-km discontinuity (391 - 420 km) and 33 km for 670-km discontinuity (634 - 667 km) (see Table 4-1), both are notably larger than the reported variations from earlier studies along the similar transect. The regional average depths of 412.1 km and 648.1 km agree well with the corresponding values of 411 km and 654 km from *Gu et al.* [1998] and are only slightly shallower than those (418 km and 660 km) of *Flanagan* and *Shearer* [1998]. The 400-km discontinuity generally shows weak topography except at cap 6, where a pronounced local elevation is observed. The topography of the 670-km discontinuity appears to be more undulating [*e.g., Flanagan* and *Shearer,* 1998; *Gu et al.,* 1998, 2003], in particular, the maximum elevation of 33 km from PREM under the northeastern Pacific Ocean is not reported by earlier studies of *SS* or *PP* precursors [*Flanagan* and *Shearer,* 1999; *Deuss et al.,* 2006]. We attribute some of the differences between the present and earlier studies to the difference in resolution, because strong topography on lateral scale of ~1000 km scales are often invisible to 10-deg caps (with a nominal resolution of 2000 km) used by the earlier global studies.
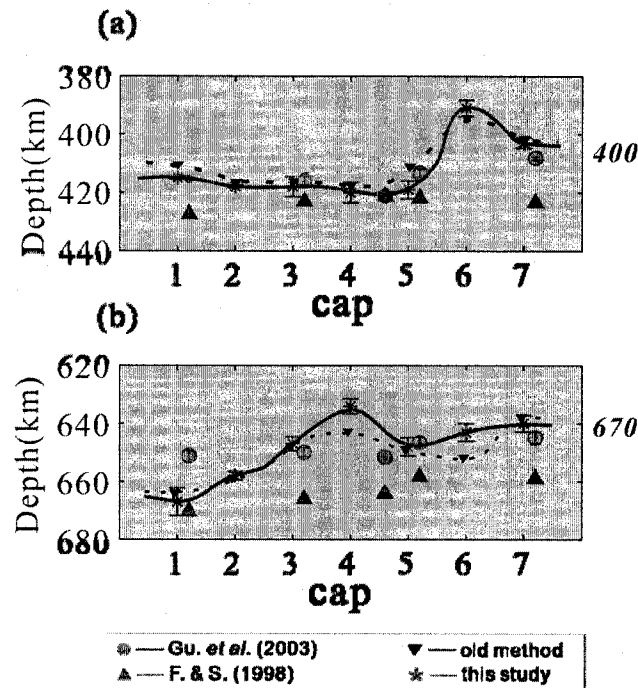
Figure 4-6   Depth of TZ discontinuities.   In each case, the star represents the depth measurement of this study. (a) The depths of 400-km discontinuity. (b) The depths of 670-km discontinuity.

49

It should be noted that the estimated depths from damped least-squares Radon transform are generally consistent with those obtained from low resolution Radon transform or the slowness slant stacking, particularly of the 400-km discontinuity. The average difference between these two methods is ~3 km and, despite the significant departures in methodology, the large lateral-scale characteristics of the discontinuities from both methods are consistent.

Two most significant topographic results are observed in this study at caps 6 and 4. The first one is a pronounced elevation of 400-km discontinuity beneath the northwestern Canada (cap 6). The discontinuity depth of 391 km is ~20 km shallower than our regional depth average (412.5 km). If we remove this extreme measurement from cap 6, the regional average would become ~416 km. The depth of 670-km discontinuity at the same location is 643 km, which is slightly shallower than the regional average (647 km). A strongly elevated 400-km and a weakly uplifted 670-km discontinuity lead to a 10-km thicker TZ than the global average of 242 km [*Gu et al.*, 2002]. The TZ thickness uncertainty in this region is ~2 km, which is too small to account for the observed anomaly.

The second significant observation is the elevation of 670-km discontinuity at cap 4, beneath the northeastern Pacific Ocean. The depth of 634 km is 13 km shallower than the regional depth average of 647 km, and is about 20 km shallower than the global average value of 654 km reported by earlier studies of *SS* precursors [*Gu et al.*, 1998]. The 400-km discontinuity at the same location is 420 km, which is slightly deeper than the regional average. This observed narrow TZ (213 km) appears to be well resolved since these measurements have small uncertainties (1.0-2.7 km).

4.4 Uncertainty analysis

The confidence levels for the final τ, p values and the depths of TZ discontinuities are computed using the bootstrap resampling algorithm [*Efron* and *Tibshirani*, 1991]. The bootstrap method is a statistical technique which is used to describe data and draw valid statistical inferences.

The bootstrap algorithm depends on a bootstrap sample, which is a sample of size n drawn with replacement from the original dataset $X = (x_1, x_2, ..., x_n)$. The bootstrap sam-

ple is denoted as $X' = (x'_1, x'_2, ..., x'_m)$. Where x'_m is one randomly selected element from the original dataset X. The name bootstrap refers to the use of the original dataset to generate new datasets X'. In our case, the bootstrap procedure is performed for each cap as follows:

1. For each cap, a large number (M=150) of independent bootstrap samples are generated randomly. Each bootstrap sample has the same number traces as we did for the analysis.

2. The damped least-squares Radon transform is performed for each bootstrap sample.

3. The $\tau - p$ values are picked and TZ discontinuity depths are measured for each bootstrap sample.

4. The mean and empirical standard deviation of M picked $\tau - p$ values and depths are computed to generate a statistically significant distribution. For each cap, M-time computation of the Radon transform is performed.

Figure 4-7 shows the bootstrap measurements of cap 7. The $\tau - p$ values are generally consistent and form a tight cluster around the mean (see Figure 4-7a). The depth uncertainties of 670-km is approximately 1. 81 km (Figures 4-7b and 4-7c), which is comparable with estimates from *Gu et al.* [2003]. The depth uncertainties for 400-km discontinuity is approximately 0.90 km (Figures 4-7d and 4-7e), which is appreciably smaller than the reported value of 1.6 km from *Gu et al.* [2003]. The remaining uncertainties (see Table 4-1) are generally comparable to or better than earlier *SS* precursor studies.

The bootstrap method used here is to measure the repeatability of Radon results that reflects the measurement error due to imperfect data quality and coverage. But this method does not reflect uncertainties from the Radon method itself. The stability of the Radon transform is more accurately determined by the size of energy maximum. Another source of error could originate from the assumed quadratic differential travel time curves based on the PREM model since the differential travel time curves from actual seismic records may deviate from these quasi-linear trends. More robust uncertainty estimates may be needed in the near future.

51
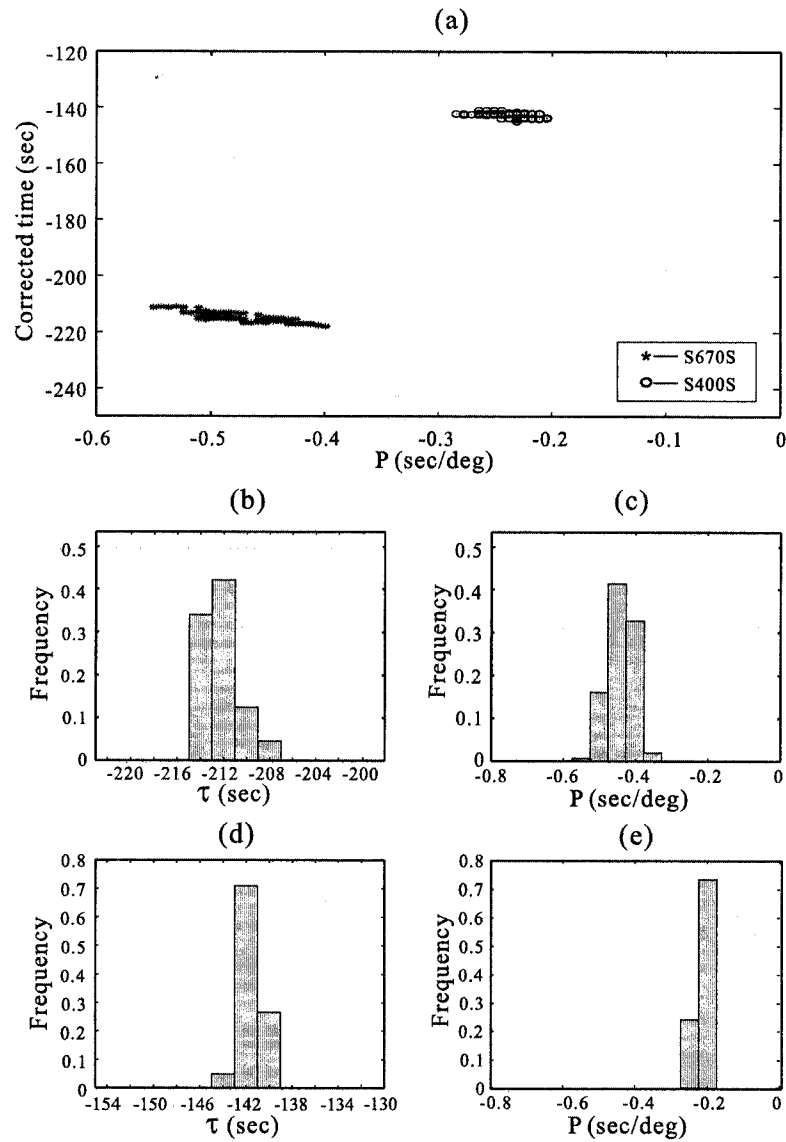
Figure 4-7   (a) Bootstrapped Radon-domain measurements of $S400S$ and $S670S$ for cap7. The histograms show the distribution of measurements for (b) the τ value of $S670S$, (c) the p value of $S670S$, (d) the τ value of $S400S$, and (e) the p value of $S400S$.

52

4.5 Other mantle reflectors

The presence of the 400- and 670-km discontinuities is well established by global and regional studies, while the existence of lithospheric [e.g., *Lehmann*, 1959; *Revenaugh* and *Jordan*, 1991; *Vidale* and *Benz*, 1992; *Gu et al.*, 2001], 250-330 km [*Revenaugh* and *Jordan*, 1991; *Deuss* and *Woodhouse*, 2002], 520-km [e.g., *Shearer*, 1993; *Gu et al.*, 1998; *Deuss and Woodhouse*, 2001] and mid/lower mantle discontinuities [*Niu* and *Kawakatsu*, 1997; *Vinnik* et al., 2001; *Shen* et al., 2003] have been debated during the past few decades. By combining careful data selection with strong constraints in the Radon domain, we are able to confidently resolve some of the aforementioned discontinuities/reflectors beneath the study region (see Table 4-2 and Figure 4-8). Figure 4-8 shows the detected reflectors beneath the study transect. The symbol size indicates the clarity of detection of that mantle discontinuity.
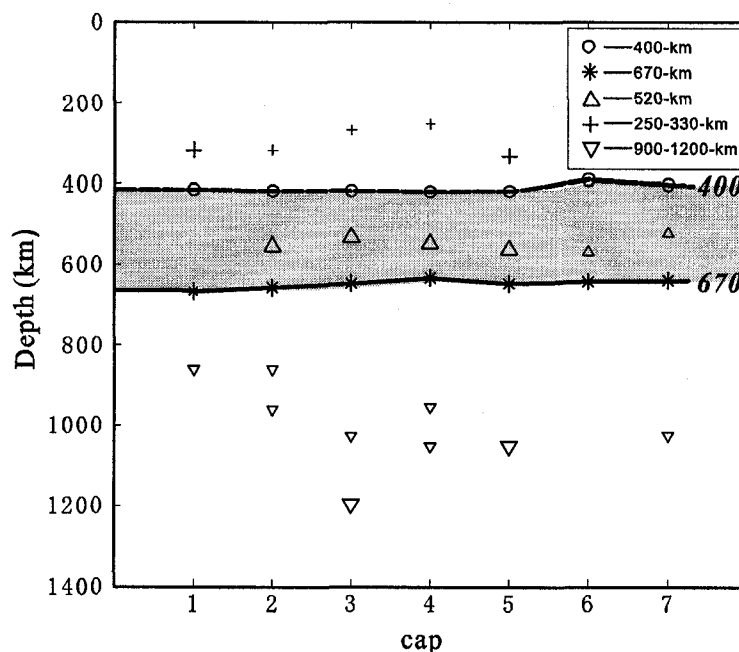
Figure 4-8   Detected mantle discontinuities/reflectors down to mid/lower mantle. The symbol size represents the quality of measurements and reliability of detection. The X discontinuities are detectable at most cap locations. The 520-km discontinuity is generally observed below 530 km, and a series of mid/lower mantle reflectors are detected.

53

Discontinuities	Clearity	Depth (km)						
		cap 1	cap 2	cap 3	cap 4	cap 5	cap 6	cap 7
220 km	no evidence	*			*	*	*	*
	weak		*	*				
	detected							
250-330 km	no evidence						*	*
	weak		318	268	253			
	detected	318				333		
520 km	no evidence	*						
	weak						570	524
	detected		554	532	547	562		
800-1100 km	no evidence						*	
	weak	860	860 961	1028	955 1055			1027
	detectable			1198		1055		

Table 4-2 The detection of other mantle discontinuities

Note: * represents no detection of discontinuities.

Above the TZ, we find little evidence for a significant seismic discontinuity between 180 km and 240 km (see Figures 4-2 and 4-3). Even cap 2, the lone location showing a $\tau - p$ peak at depth of 180 km -240 km in the projected Radon domain, is marred by relatively poor spatial data coverage (see Figure 4-2). However, underside reflections at depths between 250 and 330 km are observed at caps 1-5. The reflections from caps 1 and 5 are more pronounced, as indicated by focused Radon maxima (Figures 4-2a-b and 4-3c-d), and their depths are 318 and 333 km, respectively.

Imaging seismic discontinuities within the TZ is often difficult, especially in the time domain, due to large side-lobes of the reflections from 400- and 670-km discontinuities [Shearer, 1990; Shearer, 1996; Gu et al., 1998]. Flanagan and Shearer [1998] proposed a global 520-km discontinuity, but they claimed that reliable observations critically depend on spatial data coverage. In this study, we improve the constraint on this potential discontinuity from both time and Radon domains. We consistently identify a mid-TZ dis-

continuity (Figure 4-8), most notably beneath the Pacific Ocean [*Gu et al.*, 1998; *Deuss and Woodhouse*, 2001]. The continental portion of our transect, for example, caps 6 and 7, shows significant complexity. The amplitude of the signal is only slightly above our detection threshold. The topography of the 520-km discontinuity slightly correlates with that of the 670-km discontinuity. The range of depth perturbation is 46 km (524 - 570 km) and the mean value is 551.4 km; the latter estimate is visibly deeper than the global mean (515 km) reported by *Flanagan* and *Shearer* [1998]. We do not witness significant splitting of this reflector [*Deuss* and *Woodhouse*, 2001].

The most intriguing result from our regional mapping of mantle discontinuities is the detection of consistent mid/lower mantle reflectors. We use the term "reflector" to indicate that the nature of these reflections may not be global or horizontal. One or multiple underside reflections are consistently observed along the transect (Figure 4-8 and Table 4-2), which are associated with previously reported discontinuities at 900, 1050 and 1150 km [*Niu* and *Kawakatsu*, 1997; *Deuss* and *Woodhouse*, 2002]. For example, a reliably detected reflector is present at ~1000 km at cap 3 and cap 5. The lateral coherence of these reflectors has significant implications for the thermal and compositional variations above and within the mid mantle.

4.6 Interpretations

The depth and reflectivity of TZ discontinuities impose indirect constraints on the thermal and potential compositional variations. It is often assumed that solid-solid phase transitions from α-olivine to β-wadsleyite and from γ-ringwoodite to magnesiowüstite [(Fe, Mg)O] and silicate perovskite [(Mg, Fe)SiO$_3$] [*Ringwood*, 1975; *Ito* and *Takahashi*, 1989] are mainly responsible for the respective velocity changes at depths near 400 and 670-km. Then, a significantly shallower 400-km discontinuity near northern British Columbia (at cap 6) would, in the absence of compositional changes, suggest a colder-than-normal mantle due to the positive Clapeyron slope of the former transition [*Katsura* and *Ito*, 1989]. If we assume the Fo90 composition [*Katsura* and *Ito*, 1989], an elevation of ~30 km at this cap location would translate into a temperature difference in excess of 250°C relative to the ambient mantle. An anomaly of such magnitude is unlikely an arti-

55

fact of inaccurate mantle velocity corrections, nor could it be caused by horizontal smearing of present-day seismic structures more than 1500 km away from its cap center; the Fresnel-zone volume of the SS precursors is ~1000-1500 km [*Neele et al.*, 1997; *Shearer*, 1999]. Considering the history of this region and its proximity to major subduction zones northwest (near the eastern Aleutian trench) and south (due to the interaction of Kula, Farallon-Pacific and North America Plates), a remnant part of the subducted oceanic lithosphere in the TZ may be responsible for the observed topography. In particular, the Farallon-Pacific spreading center approached the Farallon-North America subduction zone at 50-55 Ma [*Stock* and *Molnar*, 1988; *Braunmiller* and *Nabelek*, 2002]. The plate convergence and the subsequent subduction nearly deposited the entire lithosphere of the former Kula-Farallon plates into the mantle beneath western North America. Part of the high-velocity lithosphere has potentially reached mid-mantle [*Grand et al.*, 1997; *Kárason* and *van der Hilst*, 1998; *Bunge* and *Grand*, 2000], while remaining traces of the slab material may have been littered throughout the mantle beneath North America. We hypothesize that a fraction of the substantial mass flux from the series of subduction events remained in the upper mantle and contribute to the high velocities observed at ~391-km depth north of the present-day Cascadian subduction zone. The northward extension of the subduction slab is quite possible in this tectonically complex region, considering that the remnant Farallon plate at mid-mantle depths nearly span the entire North American plate along a northwest-southeast orientation, as evidenced by high-resolution P and S wave tomography [e.g., *Kárason* and *van der Hilst*, 1998; *Boschi* and *Dziewonski*, 2000]. The presence of a fast upper-mantle velocity beneath cap 6 is also consistent with results obtained by recent high-resolution S-wave tomographic models of *Bunge* and *Grand* [2000].

Should the aforementioned high-velocity anomaly continue across the 670-km discontinuity, one would expect the 670-km discontinuity to be locally depressed due to the endothermic nature of the γ-phase phase transition. However, despite a thickened TZ, the topography of the 670-km discontinuity is slightly elevated (to 643 km) instead. The lack of anti-correlation between the 400- and 670-km discontinuities could suggest: 1). the proposed high velocity anomaly terminates within the transition zone, or 2). the pro-

56

posed high velocity anomaly continues down to the lower mantle, but the presence of compositional variations and/or other phase transitions sufficiently counteracts the thermal effects on the olivine phase transition. The first scenario could materialize if the high velocity region represents a broken piece of subducted oceanic lithosphere near the 400-km discontinuity. Local compositional variations near the 670-km discontinuity can just as easily reduce the seismic velocities and elevate the phase boundary, for example, through an increase of *Fe* and/or water content [*Sinogeikin et al.*, 1998; *Katsura et al.*, 2004; *Yusa* and *Inoue*, 1997; *Chen et al.*, 2002; *Bercovici* and *Karato*, 2003]. Furthermore, phase transition of majoritic garnet to *Ca*-perovskite [*Weidner* and *Wang*, 2000; *Hirose*, 2002; *Deuss et al.*, 2006], an exothermic process, could overcome the effect of the endothermic olivine phase transition near 670 km. The separation of thermal versus compositional variations from the limited seismic data is difficult without further data constraint.

The second significant feature of the two major TZ discontinuities is the combination of a depressed 400-km discontinuity and an elevated 670-km discontinuity beneath the northern Pacific (see caps 4-6). The opposite movement of the phase boundaries and a thin TZ can be caused by a high temperature anomaly penetrating the TZ. If we assume a thermal origin, the TZ thickness in this region (214 km) would translate into a temperature difference of ~150°C relative to that of an average TZ mantle. The presence of the proposed low-velocity zone in this region is supported by recent tomographic models (Figure 4-9). For example, corresponding cross-sections of S20RTS [*Ritsema* et al., 1999], S362D1 [*Gu et al.*, 2003] and S20A [*Ekström* and *Dziewonski*, 1998] consistently show a low-velocity zone within the TZ in the northeastern Pacific, generally coinciding with the thinnest part of the TZ in our study region. Judging from the results of tomographic models, this anomaly has a lateral dimension of 1500-2500 km and covers a significant portion of the northeastern Pacific Ocean. The origin of the Pacific heterogeneity is unknown since the center location is relatively far from major subduction zone (in the northeast) or potentially deep-rooted hotspot (in the southwest) locations. Thermal effect aside, a vertical structure with minor variations in Fe content [*Sinogeikin et al*, 1998; *Ka-*

57

tsura et al., 2004] or the presence of H₂O/melt [*Yusa* and *Inoue*, 1997; *Chen et al.*, 2002] could offer alternative explanations for the observed phase boundary perturbations.
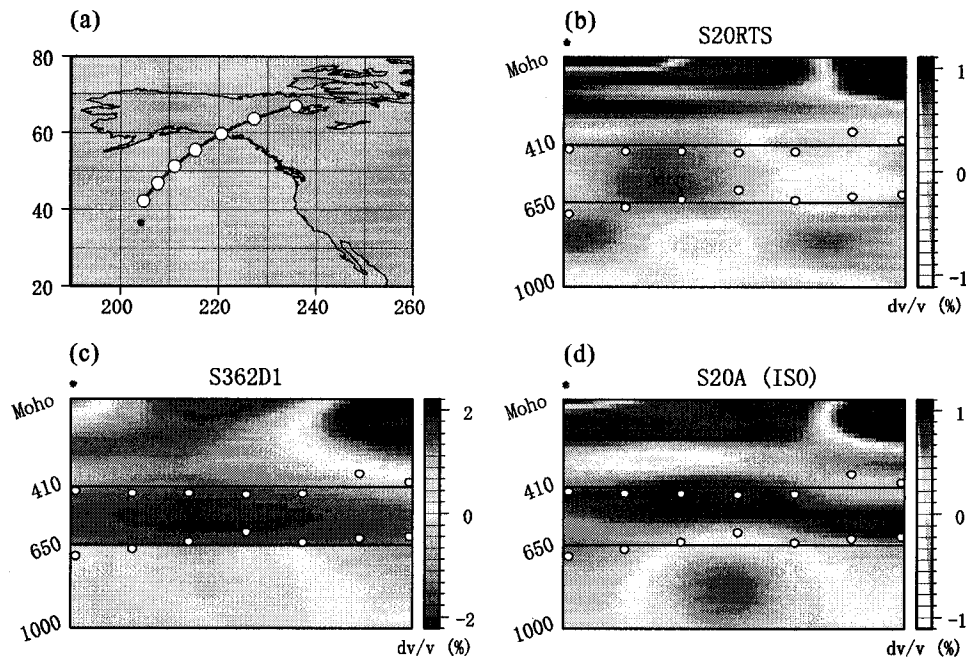
Figure 4-9 A comparison of discontinuity depth and mantle shear wave velocity. (a) The locations of cap centers. The tomographic models are (b) S362D1 [*Gu, et al.*, 2003], (c) S20A [*Ekström* and *Dziewonski*, 1998], and (d) S20RTS [*Ritsema et al.*, 1999]. The location of the anomalously thin TZ beneath the northeastern Pacific Ocean appears to coincide with a low-velocity TZ anomaly in the tomographic models.

Besides the well-known phase boundaries, the improved accuracy and resolution of the least-squares Radon transform approach enables a closer examination of intermittently reported reflectors in the mantle. We started with the Lehmann discontinuity [*Lehmann*, 1959] between 180-240 km depth ranges. Since the incorporation of this discontinuity as a global interface [*Dziewonski* and *Anderson*, 1981], a number of studies have provided regional evidence for the 220-km discontinuity beneath stable Cratons [*Gaherty* and *Jordan*, 1995; *Gu et al.*, 2001; *Duess* and *Woodhouse*, 2002] and plate-boundary zones [*Revenaugh* and *Jordan*, 1991; *Vidale* and *Benz*, 1992; *Gu et al.*, 2005]. However, the global existence of this discontinuity is still in question [*Shearer*, 1993; *Gossler* and *Kind*, 1996; *Gu et al.*, 1998; *Flanagan* and *Shearer*, 1998]. With exception of caps 2 and

58

3, where a reflection is barely distinguishable between 180 km and 240 km, we do not find evidence for significant energy peaks in the Radon domain that could be associated with a mechanical or thermal boundary layer. The lack of a robust 220-km discontinuity beneath the Pacific Ocean is not unexpected, as the shallower Gutenberg discontinuity at ~160-km depth may represent the true lithosphere-asthenosphere boundary [e.g., *Gung et al.*, 2003]. The incoherent *S220S* signal beneath the western North America at high latitudes (caps 6-8) is surprising, despite recent observations of weak or complex secondary reflections/conversions associated with the base of lithosphere [*Gu et al.*, 2001; *Deuss and Woodhouse*, 2002]. We believe that strong local-scale topographic variations similar to an eastward dip reported beneath Vancouver Island [*Bostock*, 1996] may be responsible. Still, judging from individual long-period records, the presence of a laterally *coherent* 220-km discontinuity is unlikely beneath the profile examined in this study.

We do identify, however, reflectors at moderately deeper depths (250-330 km) at most cap locations. Their presence is evidenced by one (or more) consistent distance-time move-out(s) between *SS* and *S400S* after eliminating topside reflections and crustal multiples. Similar phases have been documented by *Deuss* and *Woodhouse* [2002] using a time-domain analysis beneath the Pacific Ocean and were attributed to the presence of X discontinuities [*Revenaugh* and *Jordan*, 1991; *Li* and *Fischer*, 2002; *Williams* and *Revenaugh*, 2005]. Without consistent depth variations across the transect, it is difficult to assess whether the cause of these discontinuities represent potential phase changes in the coesite to stishovite system, exsolution of stishovite from clinopyroxenes [*Williams* and *Revenaugh*, 2005] or, in some cases, simply a deeper lithospheric discontinuity.

In addition to X discontinuities, we find clear evidence for a weak reflector within the transition zone [e.g., *Gu et al.*, 1998; *Flanagan* and *Shearer*, 1998; *Deuss* and *Woodhouse*, 2001]. The former discontinuity was first reported by *Shearer* [1990 and 1996] as a global feature, and has since been associated with either an endothermic phase change between β-wadsleyite and γ-ringwoodite [*Ringwood*, 1975] or phase changes in the garnet system [*Weidner* and *Wang*, 2000; *Deuss* and *Woodhouse*, 2001]. Along the transect examined in this study, a positive phase with a similar move-out curve as *S670S* strongly suggest the presence of a secondary velocity jump within the transition zone.

The consistent timing of the signal over several caps argues against the effect of random scattering within a laterally heterogeneous mantle. We do not observe two distinct discontinuities within the transition zone beneath continental regions, though the reflection amplitude of the lone discontinuity is visibly lower than that beneath the oceans [*Deuss and Woodhouse*, 2001].

Finally, the improvement in resolution (with 5-deg caps) and methodology enables a more accurate assessment of potential mid-lower mantle reflectors. Reflectors at depths below 670 km have been previously identified beneath subduction zones [*Karakatsu and Niu*, 1994; *Niu and Kawakatsu*, 1997; *Vinnik et al.*, 2001], and were attributed to the effect of subducted oceanic lithosphere in the lower mantle. Furthermore, *Shen et al.* [2003] identified a mid-lower mantle reflector around 1050 km beneath the South Pacific Superswell, a hotspot location, and attributed to the mineralogical phase transition at the upper-lower mantle. *Wen and Anderson* [1995] suggested that a partial flow barrier may exist near 900 km as the result of chemical difference. In this study, one or more mid/lower mantle reflector(s) is consistently present beneath the cap locations, though their lateral depth variations across the entire profile (over 400 km) are too great to be accounted for by the topography of a single, regional discontinuity. Our results suggest that lower mantle reflectors are more common than were suggested previously and their origins and depths could vary greatly. In other words, both thermal and compositional variations could contribute to their presence. A satisfactory interpretation of these mid-lower mantle reflectors remains a work in progress.

60

4.7 Concluding remarks

In this study, the Radon transform is introduced to investigate the upper-mid mantle discontinuities. The damped least-squares solution of the Radon transform can simultaneously constrain differential travel time and ray parameter, which greatly improves the resolution and flexibility over time-domain approaches such as slowness slant stacking. The Radon transform also enables a full reconstruction of the original time series after regularization. In other words, it can be used as an effective de-noising and interpolating tool.

By means of the Radon transform, we infer the depth of mantle discontinuities from the differential travel times of long-period *SS* and its precursors. Two key observations regarding the upper mantle TZ stand out: (1) a strong elevation of the 400-km discontinuity and a normal 670-km discontinuity beneath northwestern Canada, and (2) a narrow TZ beneath the northeastern Pacific Ocean. The first observation may be an evidence of subducted oceanic lithosphere in the transition zone due to past interactions of Kula, Farallon, and North America plates. Still, potential compositional variations and garnet-perovskite phase transformations could be important near the 670-km depths in the region. The narrow TZ beneath the northeastern Pacific is most likely caused by a low-velocity heterogeneity penetrating the TZ.

In addition to a consistent 520-km discontinuity across the study region, we also successfully identified several upper-mid mantle discontinuities, but we failed to find convincing evidence for a lithospheric discontinuity between 180 and 240 km. More work remains to be done to truly understand the nature of these secondary discontinuities/reflectors in the mantle. A greater data density and wider data coverage, as well as higher resolution methods, would undoubtedly aid that effort.

Chapter 5

Imaging Velocity Structure Beneath Hotspot Locations

The Radon transform has proven to be an effective technique to constrain the differential travel time and ray parameter of SS precursors (see Chapter 4). In this chapter, I further explore the application of the non-quadratic Radon transform to SS precursors at 17 "hotspot" locations in the world. Non-quadratic Radon transform is the high resolution Radon transform, which can impose constraints on intercept time τ and ray parameter p more precisely. The differential travel time and ray parameter of SS precursors are more sensitive to the TZ topography and velocity structure beneath the bouncing point of SS. By constraining the differential travel time and ray parameter with Radon transforms, we can infer depths of mantle discontinuities. The depressed 400-km discontinuity, thinner-than-average TZ thickness and the discontinuous variation of differential ray parameter of $S400S$-SS provide critical information on the velocity structure, thermal anomaly and compositional difference of the TZ and mid-lower mantle.

5.1 Introduction

The concept of hotspot (mantle plume or hot upwelling) is first proposed by *Morgan* [1971] as a result of Earth's convection. The hotspot is defined as some hot materials ascending from deep mantle with a thin conduit and a mushroom-like head [*Morgan*, 1971]. The origin of mantle plume has been hotly debated in past three decades. Scientists are seeking answers from seismology, geodynamics, and geochemistry. There are two classes of proposal about the origin of hotspots: one is that hotspots originate from the lower mantle [*e.g.*, *Morgan*, 1971; *Depaolo* and *Manga*, 2003]; the other is that hotspots are the results of plate motions [*e.g.*, *Anderson*, 2003]. Using seismic data, tomographic techniques can provide constraints on the thermal and chemical variation that are associated with mantle plumes. However, the resolution of seismic tomography may not be high enough to image narrow plumes (<500 km), although some recent global

62

models show evidence for vertically continuous low velocity anomalies beneath some hotspots, rising from the core mantle boundary (CMB) or the TZ up to the surface [*e.g.*, *Ritsema et al.*, 1999; *Masters et al.*, 2000; *Montelli et al.*, 2004, 2006].

The topography of TZ discontinuities and the thickness of TZ may provide alternative clues to the thermal structure and/or compositional difference. The 400-km and 670-km discontinuities are generally interpreted as phase transition boundaries between olivine-spinel and post-spinel which have positive and negative Clapeyron slopes, respectively [*Katsura* and *Ito*, 1989; *Ito* and *Takahashi*, 1989]. The 400-km discontinuity is expected to depress in warm regions; therefore, the depth of 400-km discontinuity can be an indicator of hot upwellings. Conversely, the 670-km discontinuity is expected to elevate in warm regions. However, the majorite-perovskite phase transition is more active under high pressures and temperatures [*Hirose*, 2002; *Deuss*, 2007], and follows a positive Clapeyron slope that can obscure the interpretation of the 670-km discontinuity and TZ thickness. The TZ thickness is less affected by the velocity structure of the strongly heterogeneous upper mantle, and is expected to be thinner than normal if a plume ascends from the lower mantle and thicker than average if a cold subducted slab extends to the lower mantle. Therefore, TZ thickness can provide more robust constraint on the thermal structure than the individual topographies, assuming the olivine phase transition to be mainly responsible for the phase transition of the 670-km discontinuity.

The purpose of this chapter is to propose another critical constraint ---- ray parameter, to explain the velocity structure beneath hotspot locations. The ray parameter is the tangent of a travel time curve that is sensitive to the velocity structure along its ray path. We may not be able to unequivocally explain the exact origin of plumes, but we can impose key constraints on large-scale velocity variations near a plume location. In this section, the high resolution non-quadratic Radon transform is applied to simultaneously estimate depths of TZ discontinuities, TZ thickness and the velocity structure.

5.2   Observation and Radon results

Based on the selection steps outlined in Chapter 3.1.2 for source depth, magnitude, distance range, and SNR criterion, 2512 high-quality records are retrieved for 17 hotspots (Figure 5-1) characterized by a score of 2 or higher according to *Courtillot et al.* [2003]. The bin size of 10° is dictated by the number of data for an effective analysis. Most of the retrieved data sets have over 80 records to facilitate the analysis. After alignment and normalization on *SS*, these data sets are further corrected for topography, crust, and heterogeneity as presented in Chapter 3.1.3.
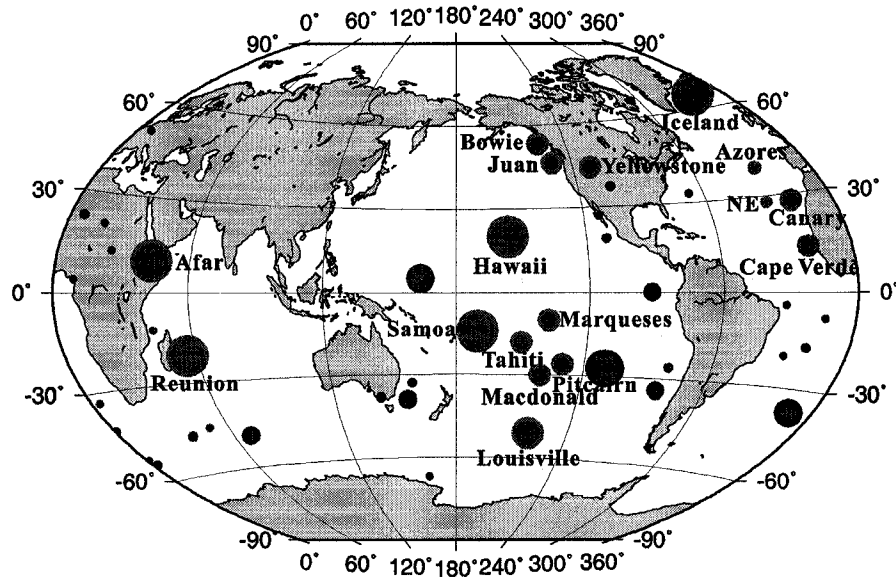
Figure 5-1   Hotspot locations in this study. All 49 blue solid circles are outlined hotspots of *Courtillot et al.* [2003]. The circle size shows the score of each hotspot. Those with red circles are the hotspots that are chosen in this study.

Figure 5-2 and Figure 5-3 show the results of non-quadratic Radon procedure with synthetic data from Juan de Fuca hotspot. Three Radon signals which correspond to *S220S*, *S400S* and *S670S* are clearly identified (Figure 5-2b); while, interfering phases

64

from $sdsS/sdsS_{diff}$ and $ScSdScS$ and are attenuated from reconstructed time series (Figure 5-3).
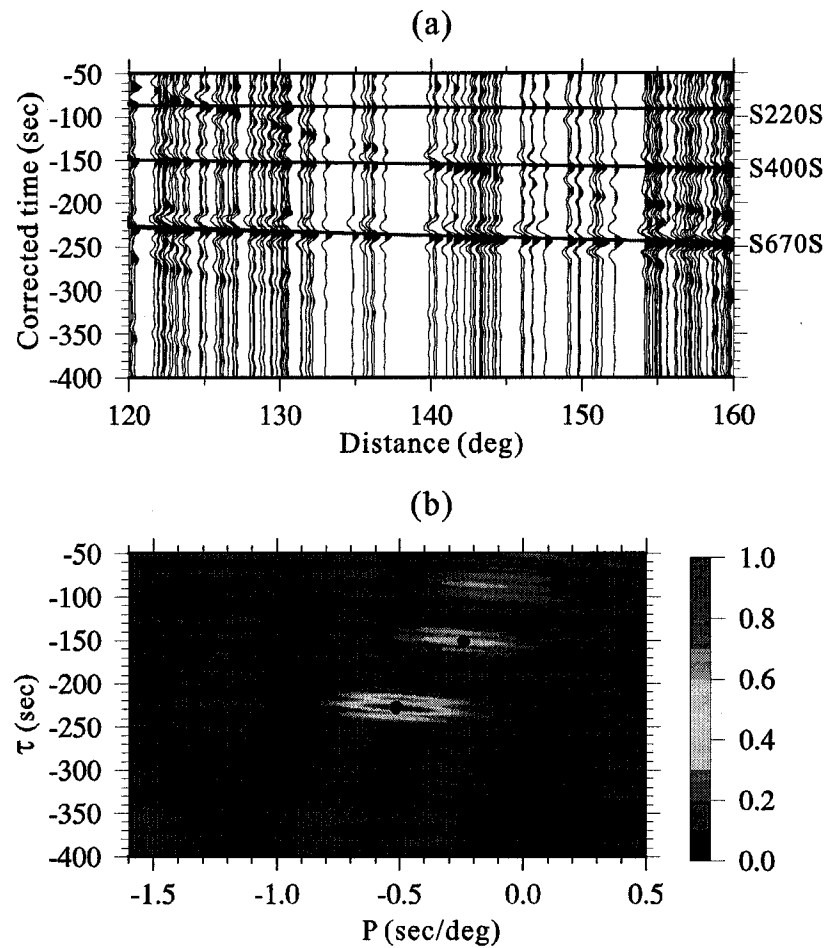
Figure 5-2   The non-quadratic Radon results of synthetic seismograms from Juan de Fuca hotspot. (a) Synthetic seismograms after alignment and normalization on SS. (b) The non-quadratic Radon signals. The intercept time τ represents the differential travel time of SdS - SS at 120°. The solid dot denotes the $\tau - p$ value of $S400S$ and $S670S$.

65
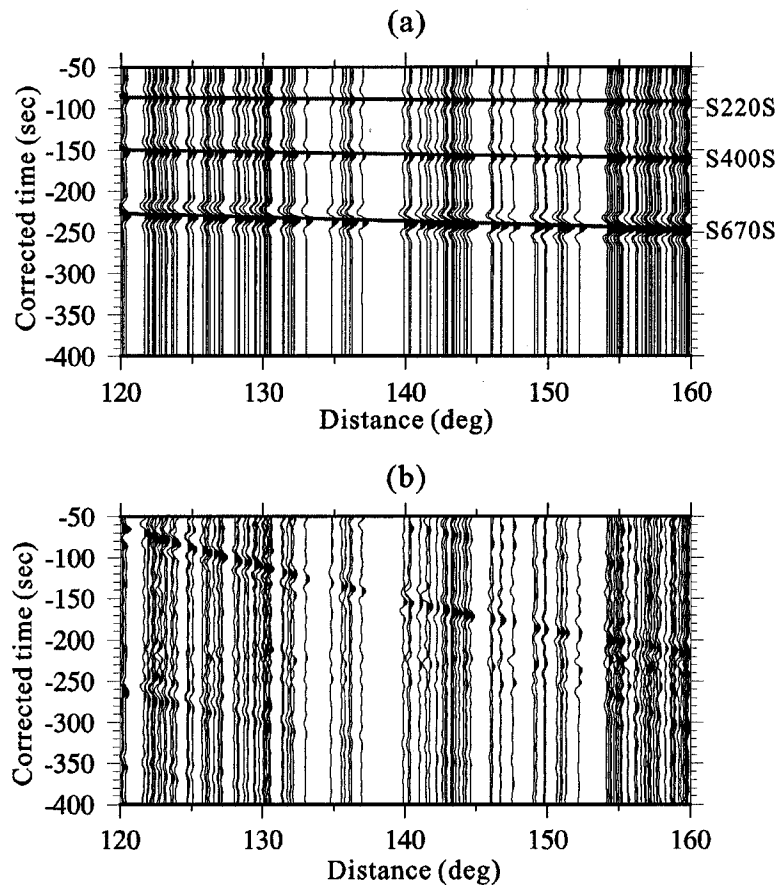
Figure 5-3 (a) Reconstructed synthetic time series. (b) The residuals between original time series in Figure 5-2 and the predictions in Figure 5-3(a). The random noise and the interference are highly attenuated.

It is unfeasible to perform Radon transform to seismic records directly, since *SS* precursors are contaminated by ambient noise in the seismic records (Figure 5-4a). To obtain better Radon signal, we precondition the data by partial stacking based on a 20° smoothing window (Figure 5-4b). Since the presence of the jump of *S400S*, it's impossible to perform Radon transform to the whole data set. Therefore, we perform the non-quadratic Radon transform to the first part of a data set from 100° to 120° in distance and to the remaining distance separately. Figure 5-4c shows the non-quadratic Radon transform to the data range of 120°-160°. The reconstructed time series show less noise and higher resolution than the original data (see Figure 5-5).

66
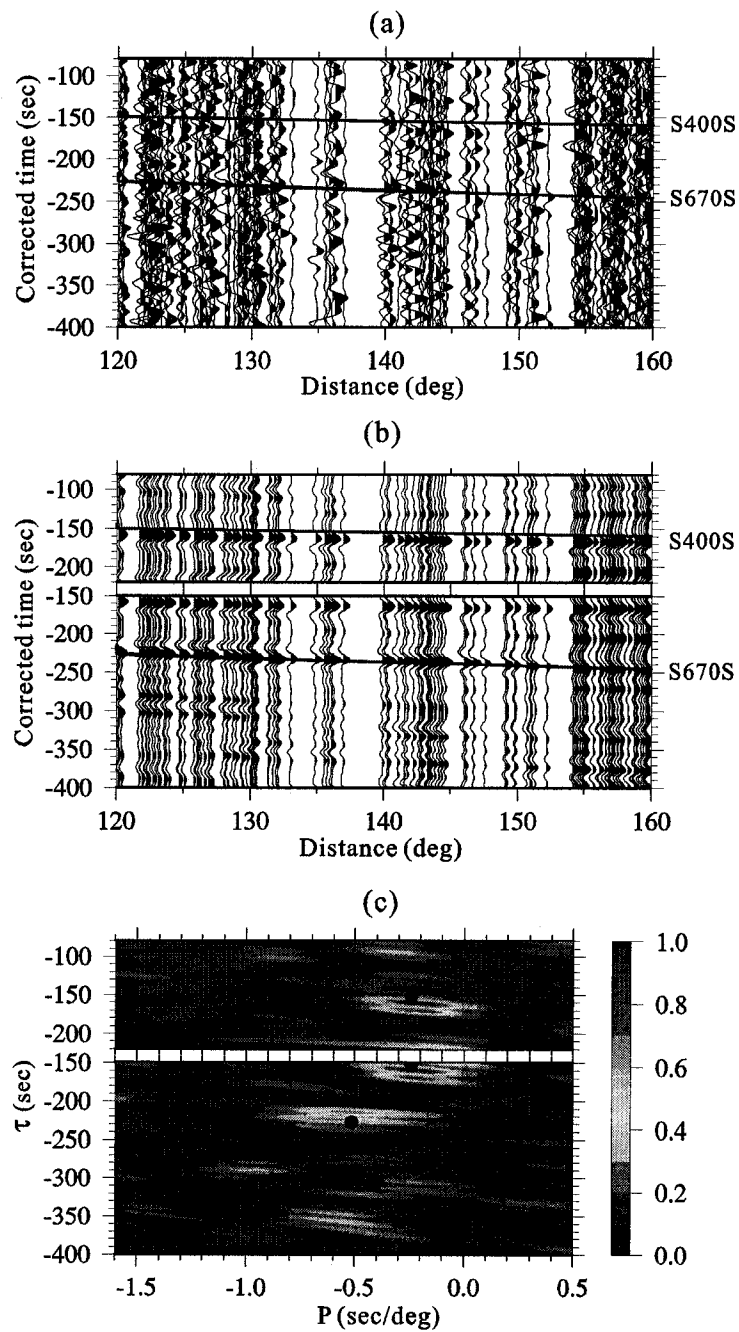
Figure 5-4   The non-quadratic Radon results of seismic records from Juan de Fuca hotspot. (a) Actual seismic records. (b) The partial stacking result using 20° distance windows. (c) The non-quadratic Radon signals. The intercept time τ represents the differential travel time of *SdS* - *SS* at 120° and the solid dot denotes the theoretical $\tau - p$ value from synthetic data.

67
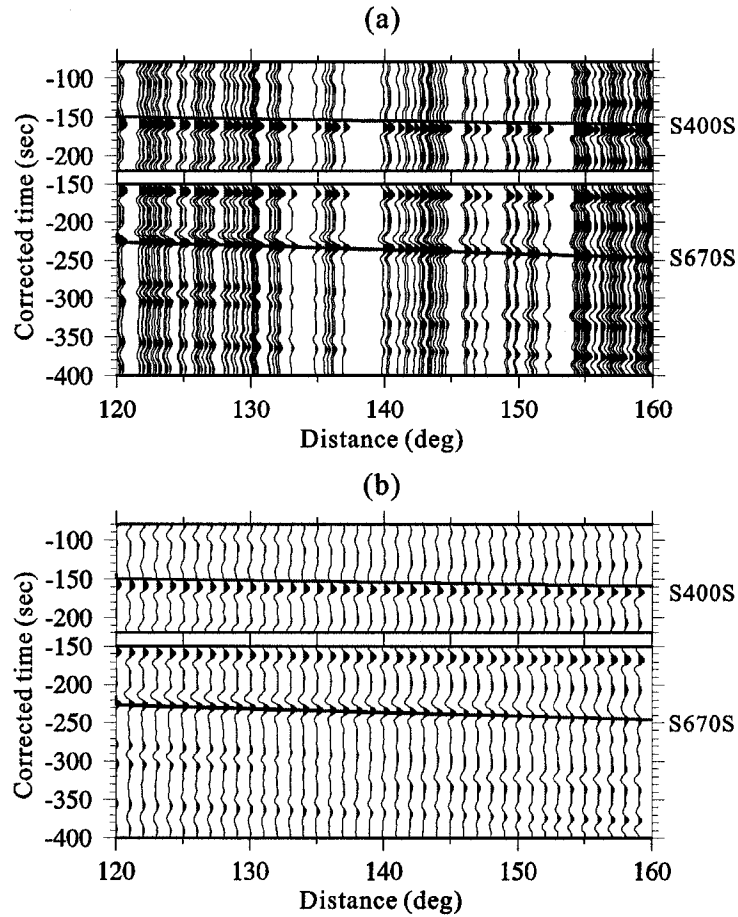
Figure 5-5   The reconstructed data with non-quadratic Radon signals in Figure 5-4(c). (a) Reconstructed time series without resampling and interpolation. (b) Reconstructed time series after resampling and interpolation.

The same procedure is performed to all synthetic and seismic records at 17 examined hotspot locations. The corrected intercept time τ and relative ray parameter p values are tabulated in Table 5-1. The ray parameter results from the first part ($100°$ $-120°$) and second part ($120°-160°$) are used to plot the exact variation of differential travel time curves. The Radon results of the second part are used to determine the depth and thickness of TZ discontinuities.

68

From our observation, we identify both positive and negative jumps in differential travel time curves of $S410S$ (Figure 5-6), which can be classified into three categories. The first type (Observation I) exhibits a positive perturbation of ray parameter relative to PREM before ~120° and followed by a negative variation of ray parameter, for example, Juan de Fuca hotspot (Figure 5-6a). This category includes Hawaii, Tahiti, Macdonald, Juan de Fuca, Yellowstone, Cape Verde and Iceland hotspots. The second type (Observation II) is characterized by a negative variation of ray parameter before ~120° and followed by a positive variation of ray parameter, such as Samoa (Figure 5-6b). This category includes Azores, Samoa, Louisville, New England, Bowie, Canary. The remaining hotspot locations, for example Marqueses and Pitcairn hotspot (Figure 5-6c), show no distinct variation of differential ray parameter (Observation III). Due to insufficient data coverage, our analysis is inclusive of Afar and Reunion hotspots.

Figure 5-7 shows the discontinuous change in the slope of differential travel time curve of $S400S$ for most of examined hotspots. The position and magnitude of travel time jumps vary significantly among the hotspots. However, the differential ray parameter of $S670S$ is surprisingly PREM-like throughout the examined distance range (Figure 5-8). The following section explores the origin of this sharp contrast between the observed travel time moveouts of $S400S$-SS (see Figure 5-7) and $S670S$-SS (see Figure 5-8).

69
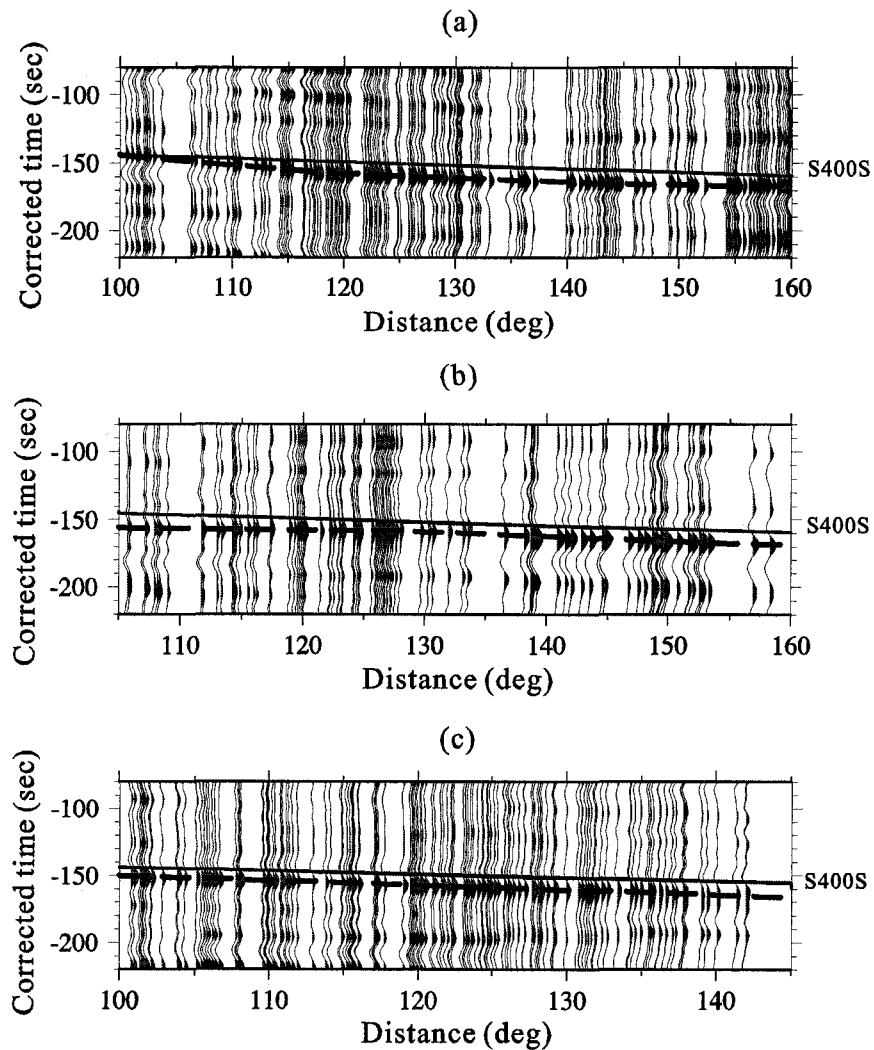
Figure 5-6 The partial stacking results of Juan de Fuca (a), Samoa (b) and Pitcairn (c), show the characteristic change of differential travel time curves of *S400S-SS*. The solid line denotes the travel time curve from PREM. The dashed line represents the observation from this study.
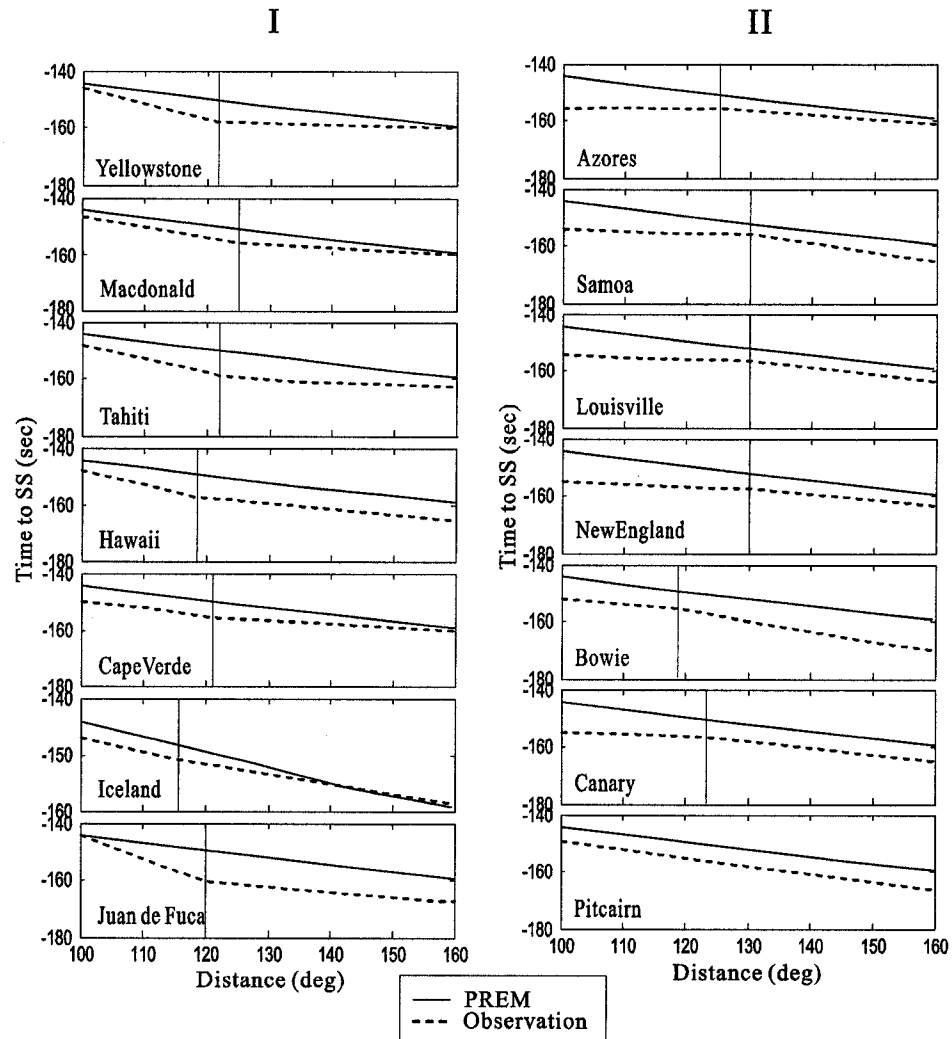
Figure 5-7   The differential travel time curves of *S400S-SS* for most of hotspot locations. The solid line denotes the travel time curves based on PREM. The dotted line represents the travel time observation from this study. The thinner vertical line denotes the turning point.

71
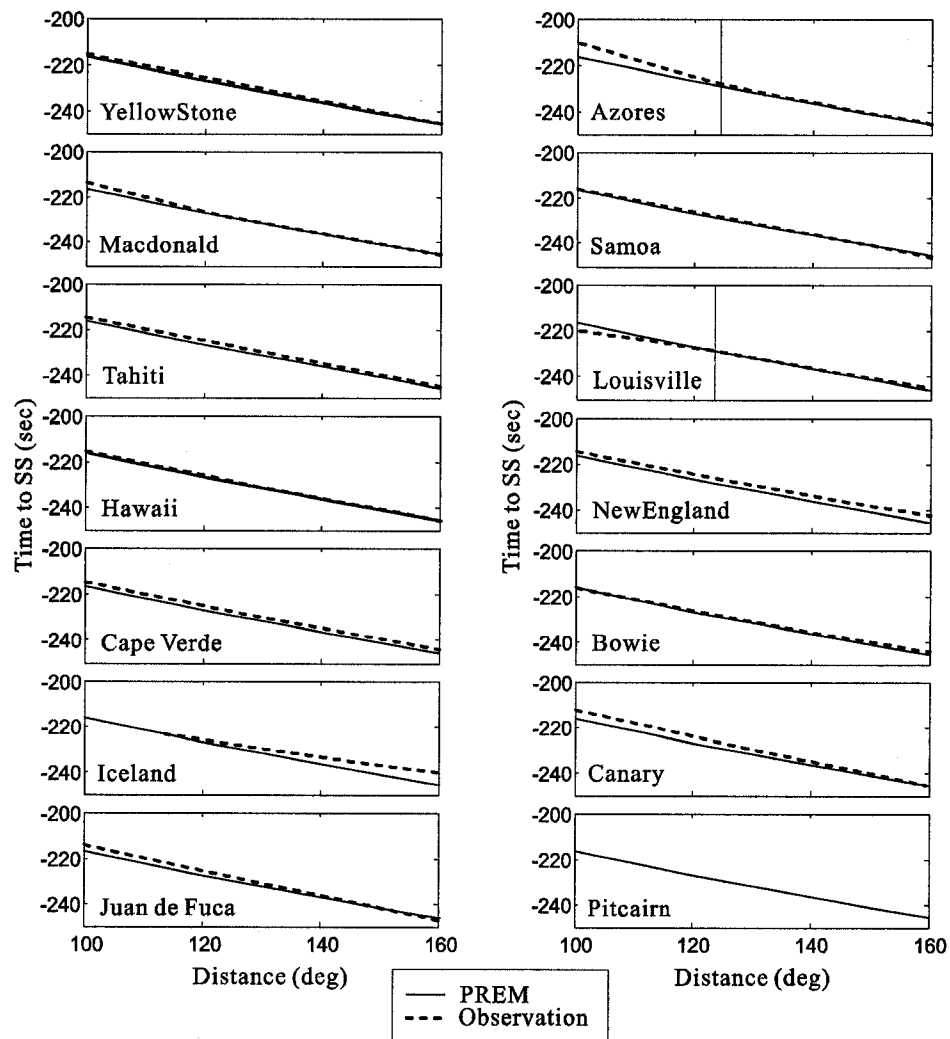
Figure 5-8   The differential travel time curves of *S670S-SS* for most of hotspot locations. The solid line denotes the travel time curves based on PREM. The dotted line represents the travel time observation from this study. No extinct variation of travel time curves as that of *S400S* is identified.

72

Hotspot	Num. of traces	location		S670S				S400S				TZ		
				τ (sec)		p (sec/deg)		τ (sec)		p (sec/deg)		Depth(km)		Thickness
		lat	long	syn	data	syn	data	syn	data	syn	data	400-km	670-km	(km)
Afar	58	10	43	-226.16	-215.68	-0.515	-0.528	-149.09	-156.10	-0.273	-0.057	414	630	213
Azores	74	39	-28	-226.82	-221.79	-0.547	-0.635	-148.81	-154.58	-0.332	-0.173	420	646	226
Bowie	298	53	-135	-227.48	-223.42	-0.506	-0.498	-150.08	-156.05	-0.283	-0.387	411	652	241
Canary	89	28	-20	-227.22	-220.58	-0.517	-0.585	-151.18	-155.71	-0.253	-0.252	412	645	233
Cape Verde	63	14	-20	-227.57	-224.32	-0.514	-0.485	-150.17	-155.40	-0.287	-0.130	414	650	236
Hawaii	224	20	-156	-227.23	-224.72	-0.519	-0.498	-149.89	-160.44	-0.268	-0.260	443	672	229
Iceland	110	65	-20	-226.72	-225.44	-0.548	-0.155	-149.50	-151.54	-0.290	-0.182	407	655	248
Juan de Fuca/Cobb	195	46	-130	-227.960	-223.000	-0.515	-0.610	-150.960	-160.130	-0.243	-0.214	420	653	233
Louisville	112	-51	-141	-227.82	-228.04	-0.516	-0.343	-151.17	-155.18	-0.243	-0.275	421	657	236
Macdonald	180	-30	-140	-227.70	-225.29	-0.531	-0.603	-150.89	-156.80	-0.218	-0.085	418	654	236
Marqueses	176	-10	-138	-226.80	-224.38	-0.533	-0.517	-149.47	-157.32	-0.285	-0.392	421	652	231
New England	98	28	-32	-226.45	-221.83	-0.568	-0.437	-149.97	-156.74	-0.269	-0.175	422	653	231
Pitcairn	155	-26	-130	-227.48	-227.46	-0.516	-0.620	-149.87	-155.29	-0.291	-0.317	416	654	238
Reunion	114	-21	56	-227.30	-227.24	-0.498	-0.478	-150.02	-156.94	-0.250	-0.320	413	669	256
Samoa	110	-14	-170	-226.44	-223.65	-0.532	-0.673	-149.44	-154.71	-0.269	-0.357	414	650	236
Tahiti	301	-18	-150	-227.07	-223.84	-0.536	-0.599	-149.69	-158.34	-0.288	-0.198	421	657	236
Yellowstone	155	44	249	-227.86	-221.13	-0.534	-0.708	-150.02	-157.43	-0.274	0.078	413	655	242
mean	144											416.1	653.5	235.5

Table 5-1   The Radon results, depths of TZ discontinuities and TZ thicknesses of 17 hotspots.

5.3 Mantle discontinuities

The depths of mantle discontinuities are inferred from high-resolution Radon domain measurements. Since the observed ray parameters of $S400S$ and $S670S$ are slightly different from that of PREM, discontinuity depths cannot be accurately obtained from a single reference epicentral distance. Therefore, we combine the ray parameter and travel time information to infer the discontinuity depths. The depths of the 400-km discontinuity (Table 5-1 and Figure 5-9) are generally consistent with those of *Deuss* [2007] and are slightly deeper (depth average is 416.1 km) relative to the global average (411 km) of *Gu et al.* [2003]. Notable differences at Azores, Canery and Cape Verde may attribute to the differences in data and methods. Out of all examined hotspots, a shallower-than-average 400-km discontinuity is only observed beneath Iceland (407 km), which is slightly elevated relative to the global average depth of 400-km discontinuity [*Gu et al.*, 1998; *Du et al.*, 2006].
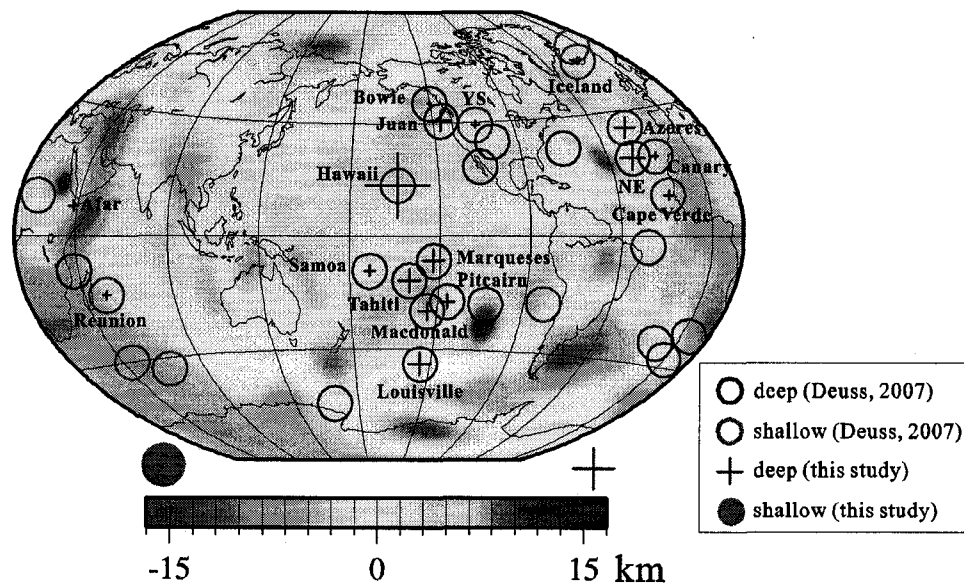
Figure 5-9   The depth measurements of the 400-km discontinuity. The contour map shows the interpolated depths of *Gu et al.* [2003]. The unfilled circles show the results from *Deuss* [2007] (without amplitude information). The size of filled circle and cross denotes the depth variation relative to the global average.

74

The depth measurements of the 670-km discontinuity (Table 5-1 and Figure 5-10) with average value at 653.5 km are close to the global average 654 km of *Gu et al.* [1998]. No obvious elevation is observed beneath the examined hotspot locations. This is inconsistent with that expected from olivine dominated post-spinel phase transition at 670-km discontinuity, which appears to suggest that mineral phase transitions in garnet are more pronounced at high temperatures [*Weidner* and *Wang*, 1998; *Hirose*, 2002; *Deuss et al.*, 2006]. At high temperatures, the majorite-perovskite phase transition with a positive Clapeyron slope is more important (Figure 5-11). At low temperatures, the post-spinel phase transition appears to be dominated by a negative Clapeyron slope (see Figure 5-11).
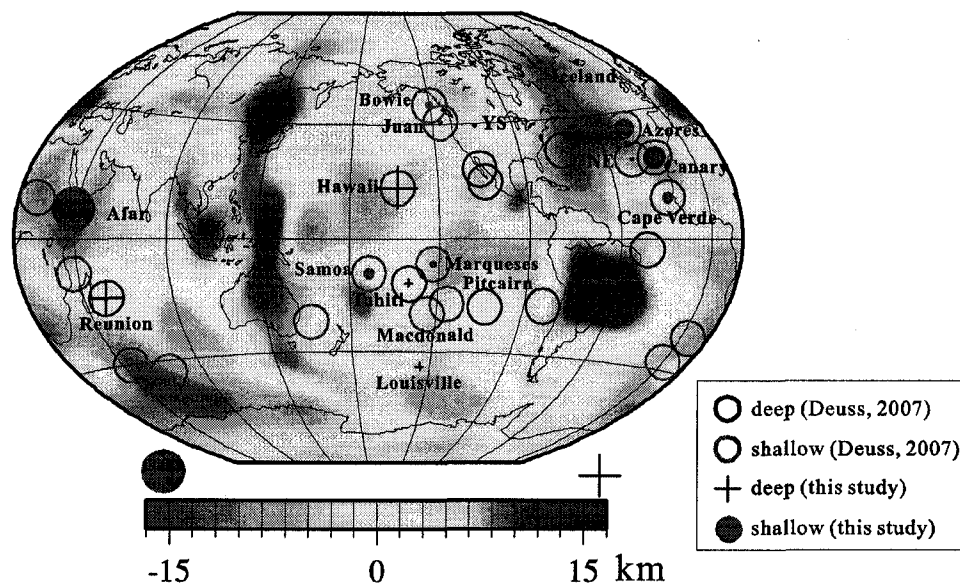
Figure 5-10   The depth measurements of the 670-km discontinuity. The contour map shows the interpolated depths of *Gu et al.* [2003]. The unfilled circles show the results from *Deuss* [2007] (without amplitude information). The size of filled circle and cross denotes the depth variation relative to the global average.
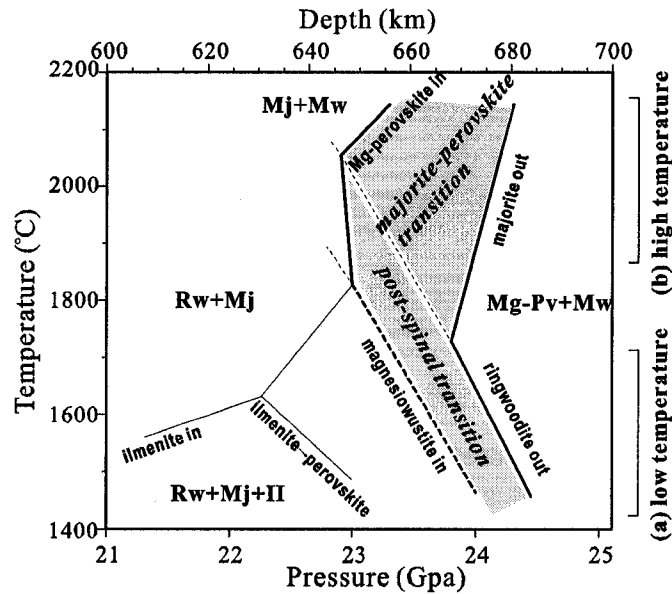
Figure 5-11 Mantle phase diagram at depth 600-700 km, after *Deuss* [2007]. The shaded area represents the perovskite-forming phase transitions. Abbreviations are: Rw=rinwoodite, Mj=majorite garnet, Pv=perovskite, Il=ilmenite, Mw=magnesiowustite, Ca=perovskite.

The TZ thickness (Table 5-1) is dominated by the locally depressed 400-km discontinuity and the resulting average beneath hotspot locations (235.5 km) is thinner than the global average of 242 km [*Gu et al.*, 2002]. TZ thickness measurements are remarkably consistent with the regional thickness variations inferred from higher resolution receiver functions of *Pds* [*Lawrence* and *Shearer*, 2006] (Figure 5-12). If a hotspot originates from the deep mantle or from TZ, the TZ thickness should be thinner, considering that the TZ is olivine-dominated. However, the TZ thickness may not be a thermometer for deep mantle plumes if garnet is dominated at 670-km discontinuity. The substantial low velocity anomalies in TZ could affect the TZ thickness as well.

76
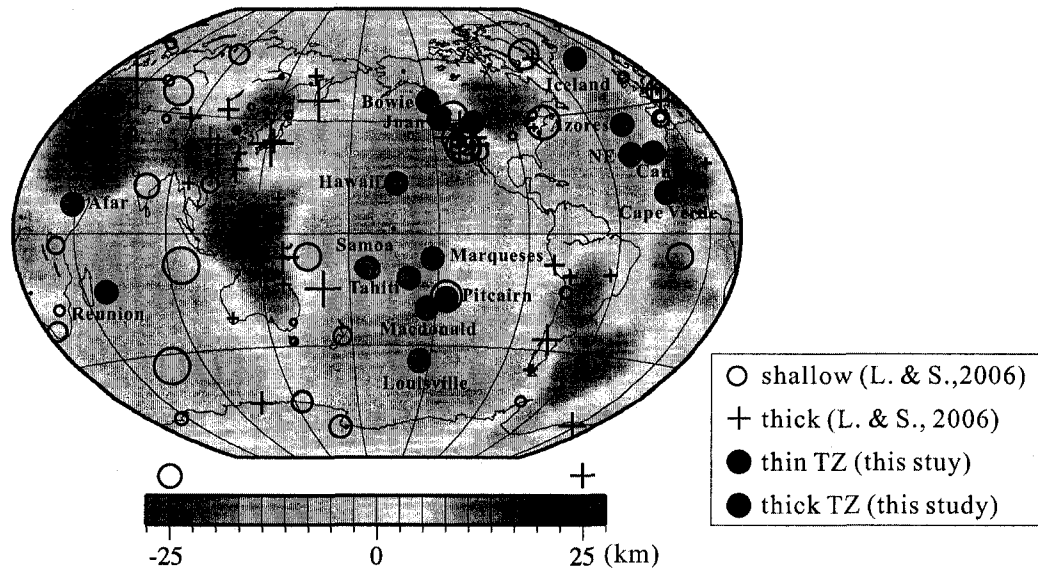
Figure 5-12 The TZ thickness measurements beneath examined hotspots. The contour map illustrates the thickness variation of *Gu & Dziewonski* [2002]. The black cross and unfilled circles denote the recent thickness results of *Lawrence & Shearer* [2006] from high resolution receiver functions. The filled circles represent the results of this study and only sign information relative to global average is given.

The presence of mid-mantle reflectors has been suggested as potential evidence of compositional stratification beneath some hotspot locations [*Shen at al.*, 2003]. To examine the existence and characteristics of potential reflectors, we conducted a systematic search in the time and Radon domain and identified clear $\tau - p$ maxima corresponding to 900-1000 km reflectors beneath Louisville (Figure 5-13), Hawaii, Tahiti, Juan de Fuca, Canary and Macdonald islands. Similar mid/lower-mantle reflectors have been observed beneath non-hotspot locations in the northern Pacific Ocean [*An et al.*, 2007], which leads us to believe that the presence of mid/lower-mantle reflectors is more common than was previously thought and their spatial distribution does not correlate with the locations of hotspots.

77
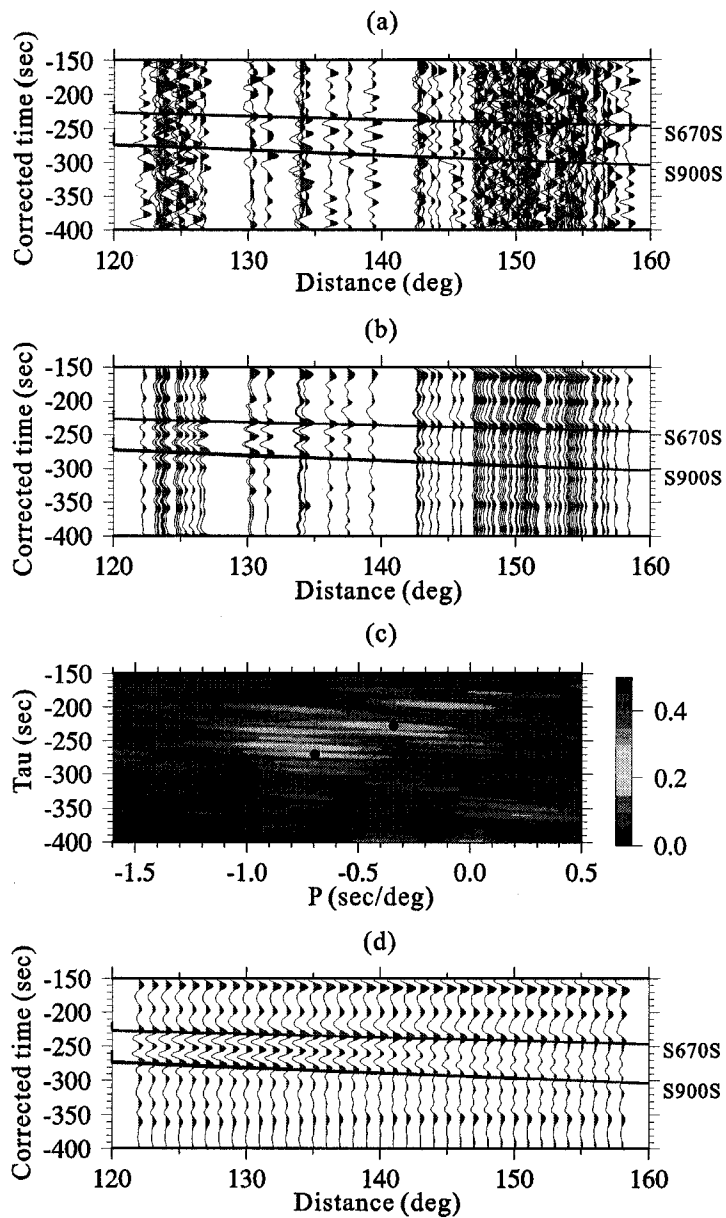
Figure 5-13   Mid/lower-mantle reflector (~900 km) is detected beneath Louisville. (a) The original seismic recordings. (b) The partially stacked time series. (c) The non-quadratic Radon signals. The solid dots represent theoretical $\tau - p$ values (from PREM) at 670- and 900-km discontinuities. (d) The reconstructed time series.

78

5.4 Velocity structures

The most striking observation in this section is the abrupt change in the differential travel time curves or the variation of differential ray parameter of $S400S$ beneath the majority of examined hotspot locations (see Figure 5-7). Both sharp increases and decreases of the differential ray parameter $S400S$ are identified. The potential sources of the sharp change in ray parameter are: 1) the velocity heterogeneity beneath hotspots, 2) the interference from $ScSdScS$ and $sdsS/sdsS_{diff}$, and/or 3) the anisotropy due to the unevenly distributed earthquake and station locations before and after the jump. The sections below examine each of these possible sources.

5.4.1 Interference

The interferences from phase $ScSdScS$ and $sdsS/sdsS_{diff}$ are clearly identified in synthetic seismograms from Hawaii hotspot (see Figure 5-14a). We partially stack the synthetic data along the differential travel time curve of $S400S$ and $S670S$ calculated from PREM as we did to the seismic records. The interfering phases do not dominate the partially stacked data in Figure 5-14(b), where only SS precursors are clearly identified. This is because that partial stacking can suppress interfering phases and some incoherent noise in certain extent. From this test, we believe that the presence of interfering phases is unlikely the major reason of the jump in the differential travel time curve of $S400S$, even though it might have minor influences on the observation.

79
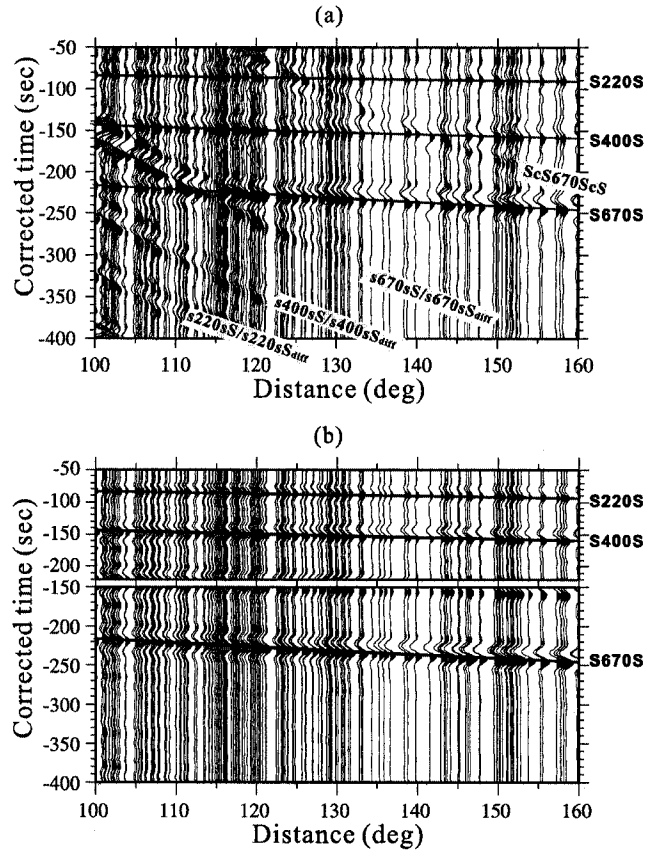
Figure 5-14 The partially stacked result of synthetic data from Hawaii hotspot. (a) The original synthetic seismograms. (b) Partially stacked traces. The interfering phases are attenuated from stacked data.

5.4.2 Azimuth and heterogeneity

The studied SS data are collected as geographic bin with 10° size; therefore, it is possible that the uneven distribution of data could be partially responsible for the observed change in ray parameter. To examine the effects of data distribution on Radon transforms, we calculate heterogeneity corrections and back azimuths at SS bouncing points for all studied hotspot locations. Figure 5-15 and Figure 5-16 display the back azimuths and heterogeneity corrections from Hawaii and Bowie hotspot. Despite the non-random distributions of velocity corrections and azimuths, neither plot exhibits differences between shorter (100°-120°) and longer (120°-160°) distances that are significant enough to pro-

80

duce the observed ray parameter jumps. We therefore conclude that ray path orientations and heterogeneity corrections are not responsible for the anomalous differential travel time curves of S400S beneath hotspot locations.
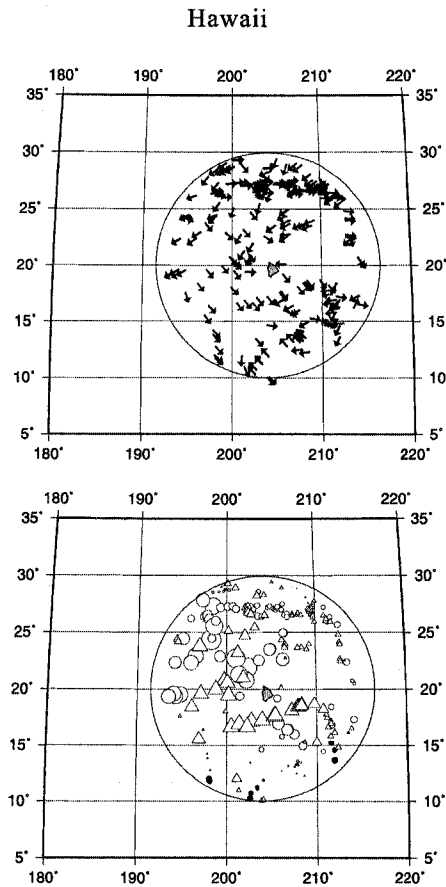
Figure 5-15 The back azimuths and heterogeneity corrections of Hawaii hotspot. The top panel shows the back azimuths of bounce points, and the bottom panel represents the heterogeneity corrections. The red and blue arrows in the top panels represent the back azimuths from the points with distance in 120°-160° and in 100°-120°, respectively. The red solid triangles and circles denote the positive heterogeneity corrections for the points with distance in 120°-160° and 100°-120°, respectively. The blue empty triangles and circles denote the negative heterogeneity corrections for the points with distance in 120°-160° and 100°-120° respectively. The size of symbols represents the magnitude of the value.

81
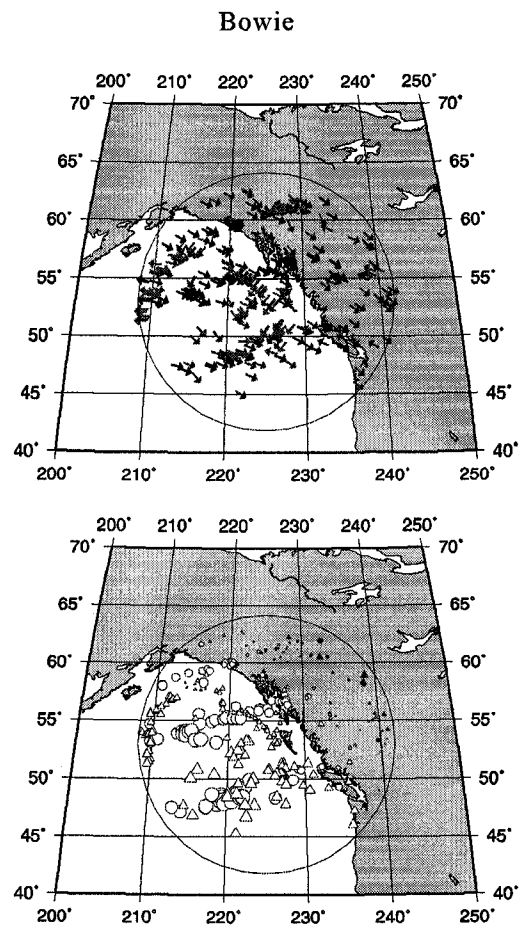
Bowie

Figure 5-16 The back azimuths and heterogeneity corrections of Bowie hotspot. The top panel shows the back azimuths of bounce points, and the bottom panel represents the heterogeneity corrections. The meaning of symbols is the same as that in Figure 5-15. The red and blue arrows in the top panels represent the back azimuths from the points with distance in 120°-160° and in 100°-120°, respectively. The red solid triangles and circles denote the positive heterogeneity corrections for the points with distance in 120°-160° and 100°-120°, respectively. The blue empty triangles and circles denote the negative heterogeneity corrections for the points with distance in 120°-160° and 100°-120° respectively. The size of symbols represents the magnitude of the value.

82

5.4.3 Velocity models

From the above analysis, we can rule out the interference, azimuth and/or heterogeneity corrections as potential reasons of differential travel time curve (or ray parameter) jump of $S400S$. The observed jump appears to be unique to hotspot locations, for example, with the exception of cap 4, none of cap locations beneath the northeastern Pacific Ocean and North America exhibits the same phenomenon (see Chapter 4). The association of ray parameter variation with hotspot is clearly evident beneath Hawaii hotspot, a well studied hotspot with a potential deep-mantle origin. We compare the partial stacking results from Hawaii hotspot and two cap locations 20° away from it. The resulting stacks (see Figure 5-17) at the nearby locations of Hawaii do not exhibit significant change in ray parameter. Therefore, the variation in ray parameter might be the unique feature of hotspot locations.
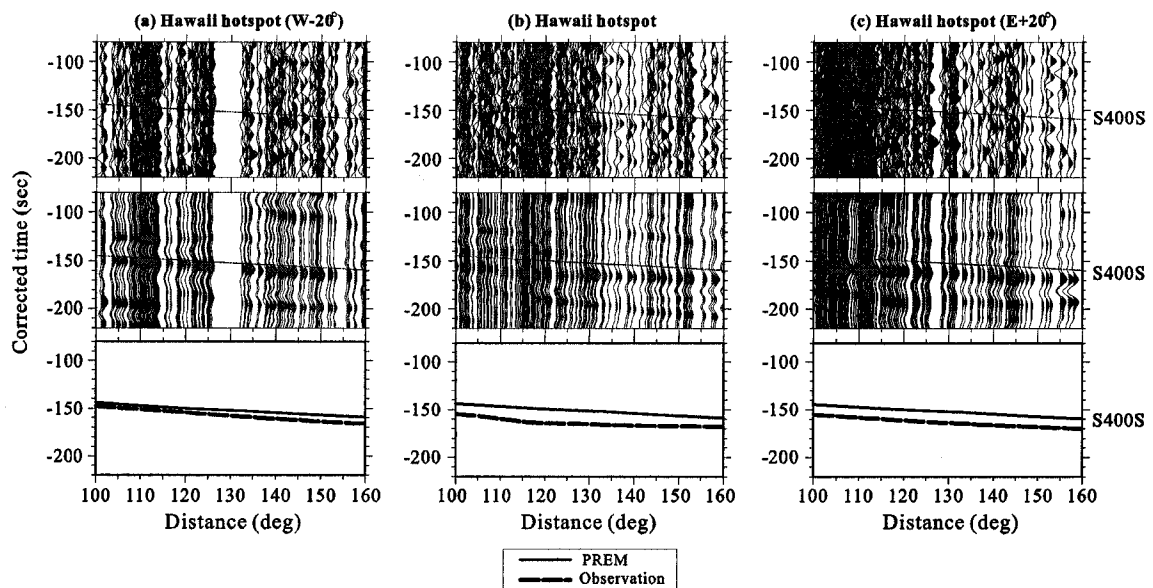
Figure 5-17 The differential travel time observation of $S400S$ from Hawaii hotspot and two adjacent locations to the west and east 20° away from Hawaii hotspot. The solid line in the bottom panel represents the travel time curve from PREM; the dashed line denotes the observed travel time curve.

83

The differential travel times of *SdS-SS* are heavily affected by upper mantle velocity structures and discontinuity topographies. So far, the topography of discontinuities and mantle velocity have been obtained through gradually independent approaches. The drawback of such approach is that these two quantities will trade-off with one another. The exception is the studies by *Gu et al.* [2002] and *Reif et al.* [2007] which simultaneously invert for mantle shear velocity anomalies and TZ discontinuity topographies. We hereby examine the relation between differential travel time and topography of TZ discontinuities. The differential travel time from a depression of 16 km on the 400-km discontinuity translates into a 4.5-5.7 sec time delay (Figure 5-18). In comparison, an elevation of 16 km on the 670-km discontinuity causes a time difference of 2.2-3.2 sec (Figure 5-18). The remaining time difference is caused by decreased seismic velocities in the upper mantle or the TZ.

(a)

(b)
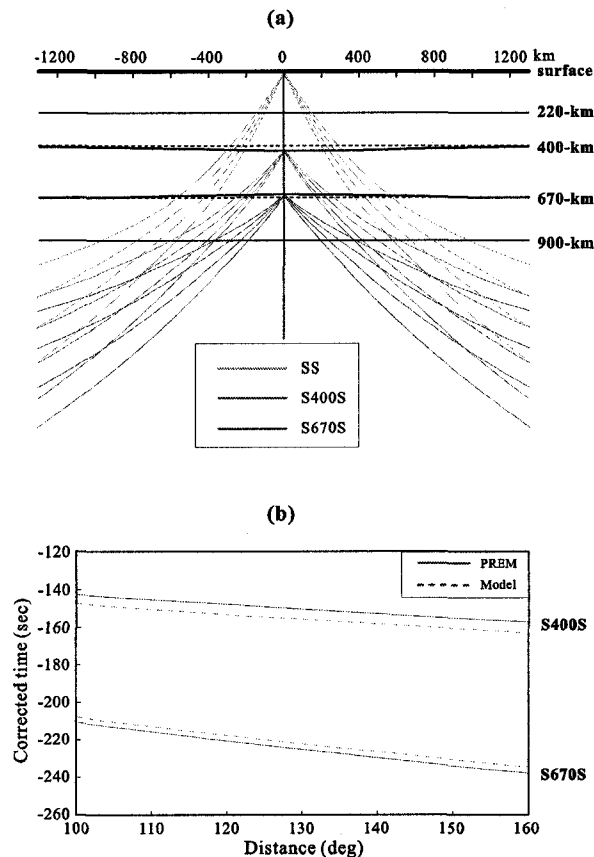
Figure 5-18 The topography of TZ discontinuities and the differential travel time curves of *SdS-SS*. (a) The topographic model with depressed 400-km discontinuity by 16 km and elevated 670-km discontinuity by 16 km. The dashed lines represent the depths at 400 km and 670 km. (b) The differential travel time curves of *S400S* and *S670S*.

To evaluate the effect of velocity anomaly upon travel time curves, we generate a series of 2D spherical shear wave velocity models. PREM [*Dziewonski* and *Anderson*, 1981] is adopted as the starting shear velocity model. The factors that affect the differential travel time and ray parameter are the topography of TZ discontinuities and, the magnitude and volume (lateral dimension and depth) of velocity anomalies beneath a hotspot location.

In this study, the average depths of 400-km and 670-km discontinuities beneath hotspot locations are 416 km and 653.5 km, respectively. In our 2D ray tracing analysis, we

85

fix the topography of TZ discontinuities to the average depths of 416 km and 654 km at a given hotspot location.

The nominal radius of a plume is 100-150 km; however, a long-lived plume may heat up the surrounding mantle over much larger distances [*Anderson*, 2007]. If the origin of the observed change in differential ray parameter is due to thermal anomaly, the epicentral distance at which the abrupt change in differential ray parameter occurs should reflect the temperature gradient and the volume of anomaly. We hereby consider the effect from strongest lateral velocity gradients and the volume of velocity anomaly over 400 km in radius. To simplify the model, we divide the anomaly into several layers: 1) 0 km – 416 km (the upper mantle); 2) 416km – 654 km (the TZ); 3) 654 km – ~900 km (the mid-mantle); 4) below ~900 km (the lower mantle).

The combination of mantle velocity anomaly and the topography of TZ discontinuities can cause differential travel time differences of *S400S* and *S670S*. The width of velocity anomaly in the upper mantle is more difficult to determine since all the rays travel through an anomaly of 300-km or wider produce similar travel time perturbations. Hence, we set the width of the first proposed anomalous layer to 400 km and use the Guassian filter to produce a lateral gradient. The ray path inside the anomaly and the structure of the last anomalous layer have critical effect on the variation of differential ray parameter which can be explained by the ray tracing theory.

We use the following observation criteria to constrain thousands of velocity models:

1. The differential travel time of *S400S*, which is caused by the topography of 400-km discontinuity and the velocity structure of the upper mantle. The average time difference between observed *S400S* and the PREM at 120 deg is 6.4 sec. We fix the topography of 400-km discontinuity at 416 km, which will account for 4.5-5.7 sec time difference. The excessive time difference should result from low velocity anomalies in the upper mantle.

2. The differential ray parameter variation of *S400S* and its "bending" position. The cause of ray parameter change reflects the ray path difference between *SdS* and *SS* inside the velocity anomaly. The volume (depth and width) of anomaly can be used to model the exact position of the jump in travel time curves.

86

3. The differential travel time and ray parameter of *S670S*. Unlike the 400-km discontinuity, the differential travel time curve of *S670S* shows only minor variations. Our preferred models must reflect the substantial difference in the characteristics of *S400S* and *S670S* travel time curves.

According to the above-mentioned criteria, we present the following candidate velocity models (Figure 5-19 and Figure 5-20) from thousands of randomly generated models. We quantify them into two major categories that we refer to as Model I and Model II which correspond to observation I and observation II, respectively.

Model I (Type I hotspots): We observe three possible models which correspond to observation I (Figure 5-19). The first two models (Model I-1 and Model I-2 in Figure 5-19) have low velocity anomaly in the upper mantle and beneath the 670-km discontinuity. The low velocity anomaly in the upper mantle contribute to the differential travel time of *SdS*. Inside the TZ, both positive (Model I-2) and negative (Model I-1) velocity anomalies obtain a sharp change of *S400S* differential ray parameter. Furthermore, a -6% shear velocity anomaly beneath 670-km discontinuity is required to generate a big jump, which is in agreement with the result of global tomography. This large volume of ultra-low velocity anomaly may be explained by potential ponding of plume material. Beneath the substantial low velocity anomaly, a thinner low velocity plume conduit may exist. This is likely to occur if a deep-rooted mantle plume ascends and ponds beneath the 670-km discontinuity. However, the ultra thinner conduit is hard to detect with SS precursor dataset (see Figure 5-21). Because there is insufficient constraint on the lower mantle velocity structure from *SS* precursors. Model I-3 has the preferable travel time curve of *S400S* with observation I; however, the travel time curve from S670S provides evidence against observation I. Therefore, model I-3 can be ruled out. The remaining models I-1 and I-2 are the only models to explain observation I. Both models confer deep-rooted mantle plumes beneath the Type I hotspots.

87
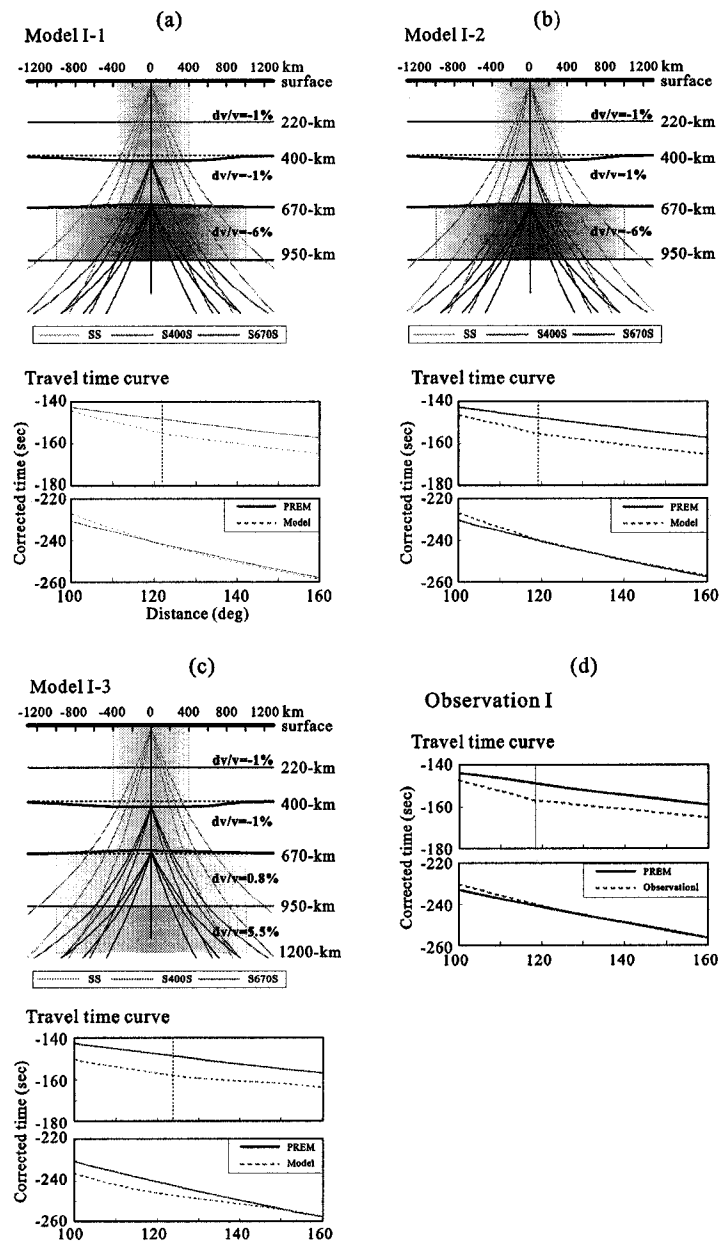
Figure 5-19 Numeric velocity models and their travel time curves which correspond to observation I. (a) The low velocity extends to mid mantle. (b) The low velocity anomaly extends to the mid mantle while a slight high velocity anomaly inside the TZ isolates this low velocity. (c) The low velocity anomaly extends to the TZ and followed by a high velocity anomaly. (d) The observed differential travel time curves ---- Observation I.

88
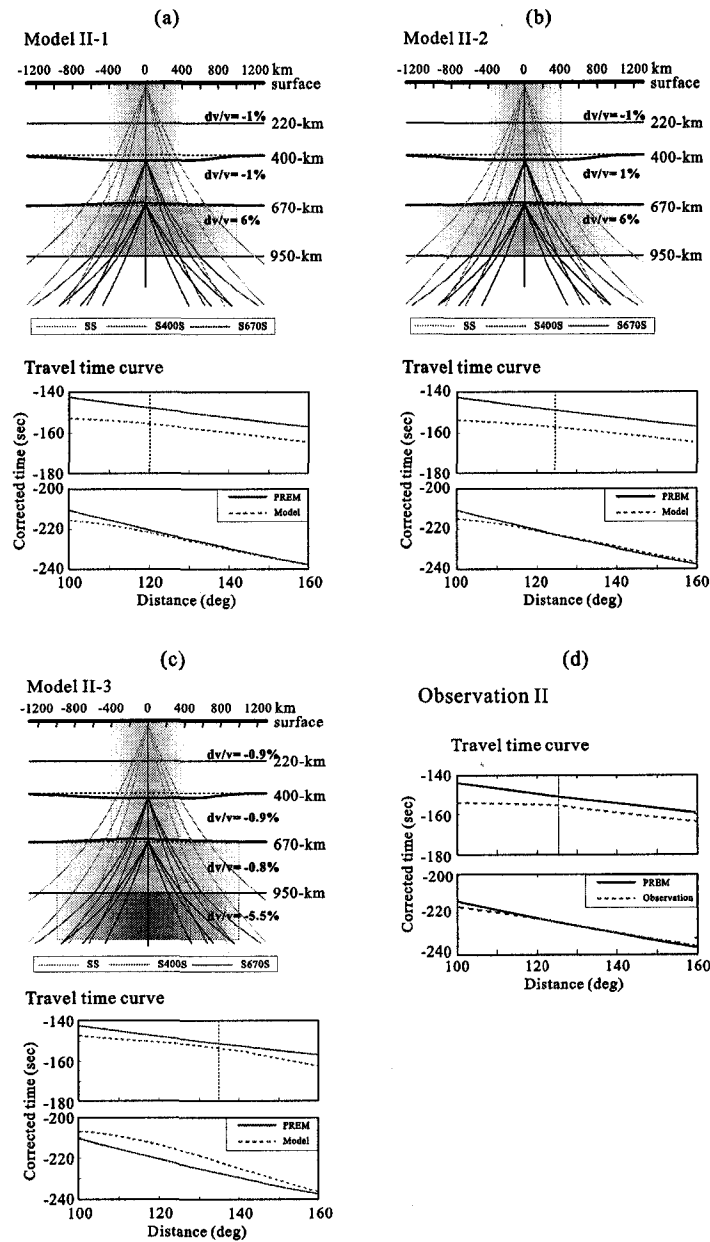
Figure 5-20 Numeric velocity models and their travel time curves which correspond to observation II. (a) The low velocity extends to the TZ followed by a high velocity anomaly. (b) The low velocity anomaly extends to the upper mantle followed by a high velocity anomaly in the TZ and mid-mantle. (c) The low velocity anomaly extends to the min-mantle. (d) The observed differential travel time curves ---- Observation II.

Model

-1200 -800 -400 0 400 800 1200 km

surface

dv/v=-1% 220-km

400-km

dv/v=-1%

670-km

dv/v=-6%

950-km

dv/v=-4%

| SS | S400S | S670S |

Travel time curve
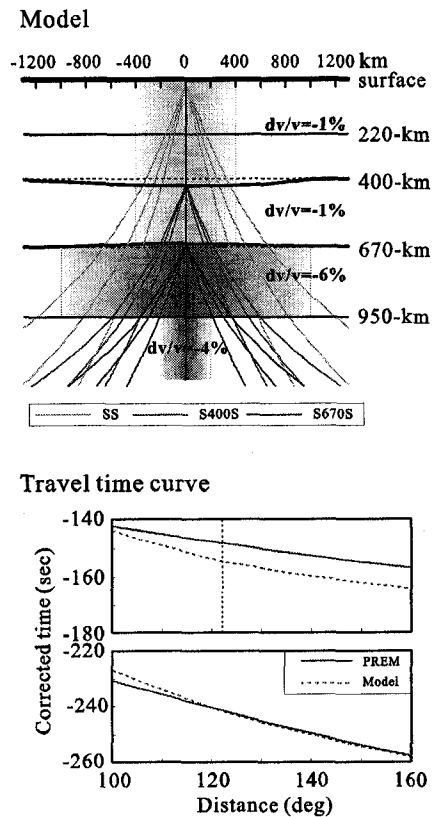
Figure 5-21 A thin plume conduit may exist beneath the large volume of low velocity plume head. But it is hard to detect with SS precursor dataset, because the rays of SS and its precursors may not travel through this low velocity anomaly beneath 950 km.

Model II (Type II hotspots): The velocity anomaly in the upper mantle is set the same as Model I, while a high velocity anomaly beneath the 670-km discontinuity is required to produce the differential travel time curves of observation II for models II-1 and II-2. In the TZ, both a low or high velocities may exist (see Figure 5-20a and 5-20b). Extremely high velocities (for example, +6% velocity variations) beneath 670-km discontinuity are required to generate the observed jump of differential travel time curves. From models II-1 and II-2, the low velocity anomaly may not extend below the TZ. The differential travel time curve of S400S from Model II-3 is consistent with observation II; however, the travel time curve of S670S is inconsistent with the observation II. Hence, we conclude that model II-3 is not a suitable model for observation II.

90

In short, the first two models in Figure 5-19 and Figure 5-20 are consistent with our observations. The magnitude and volume of low velocity vary according to the differential travel times. We hereby adopt model I-1 as a prototype in the discussion of the magnitude and volume of shear velocity structure beneath hotspots. Velocity variations of the upper mantle and TZ affect the travel time difference of $S400S$ and $S670S$, while the magnitude of velocity anomaly of the last anomalous layer affects the magnitude of a jump (Figure 5-22). When the hypothesized velocity perturbation varys from negative (-6%) to positive (+3%), the travel time curves of $S400S$ changes from observation I to observation II (see Figure 5-22). The differential ray parameter changes rapidly prior to the jump, but slows down consistently after the jump. The travel time curves of $S670S$ do not change significantly, which is consistent with observation.

Model
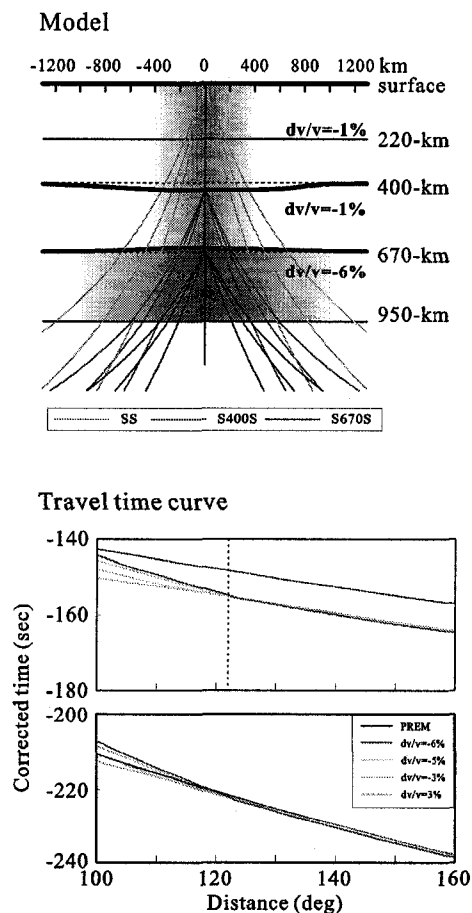
Travel time curve

Figure 5-22 The magnitude of velocity anomaly in the last anomalous layer affects the jump of differential travel time curves of $S400S$ and $S670S$.

The volume change of the last anomalous layer affects the ray path difference of *SS* at different epicentral distance and the position of the jump (see Figure 5-23 and Figure 5-24). In Figure 5-23, the width of the last anomalous layer is decreased from 1000 km (Figure 5-23a) to 800 km (Figure 5-23b). Accordingly, the turning point of differential travel time curve moves from ~124° to ~144°; the latter distance value is inconsistent with observation. Hence, we conclude that the width of the last anomalous layer should be wider than 800 km. The depth variation of the last anomalous layer has similar effects as width. The depth of the last anomalous layer changes from 950 km (Figure 5-24a) to 1000 km (Figure 5-24b), and the turning point position has switched from 124° to 132°, and the differential travel time has changed accordingly (Figure 5-24).
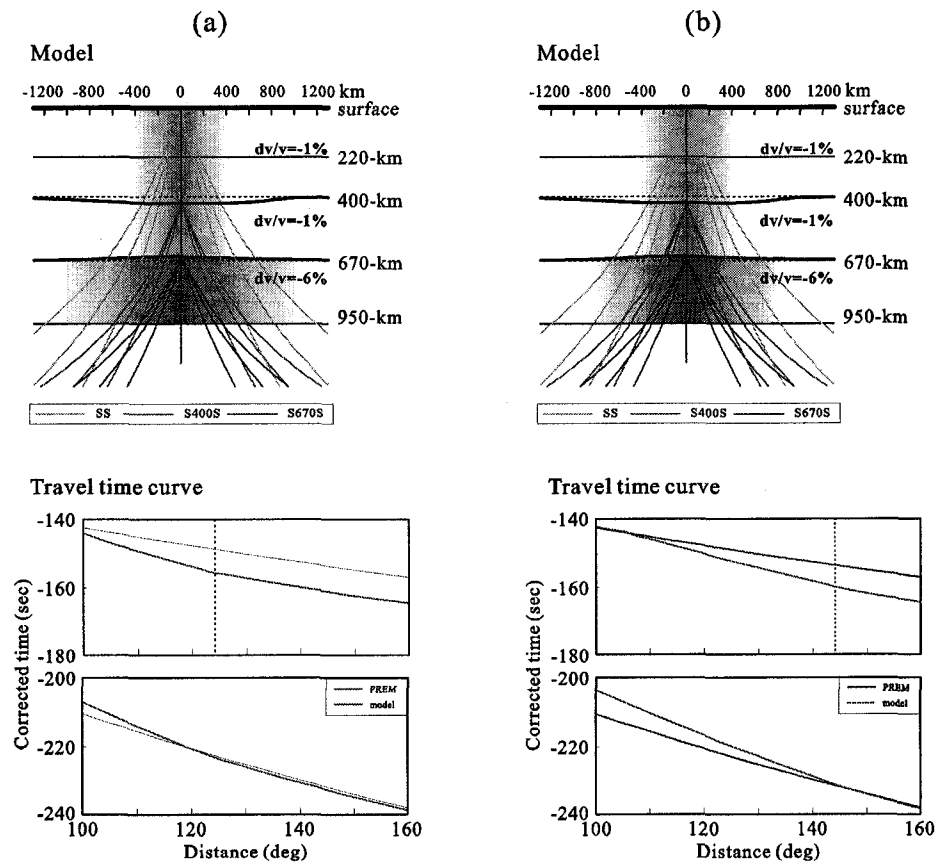
Figure 5-23 The width of velocity anomaly in the last anomalous layer changes the jump position of differential travel time curves. (a) The width of the last anomalous layer is set to be 1000 km, and the jump position of S400S is at 124°. (b) The width of the last anomalous layer is set to be 800 km, while the jump position is about 144°.
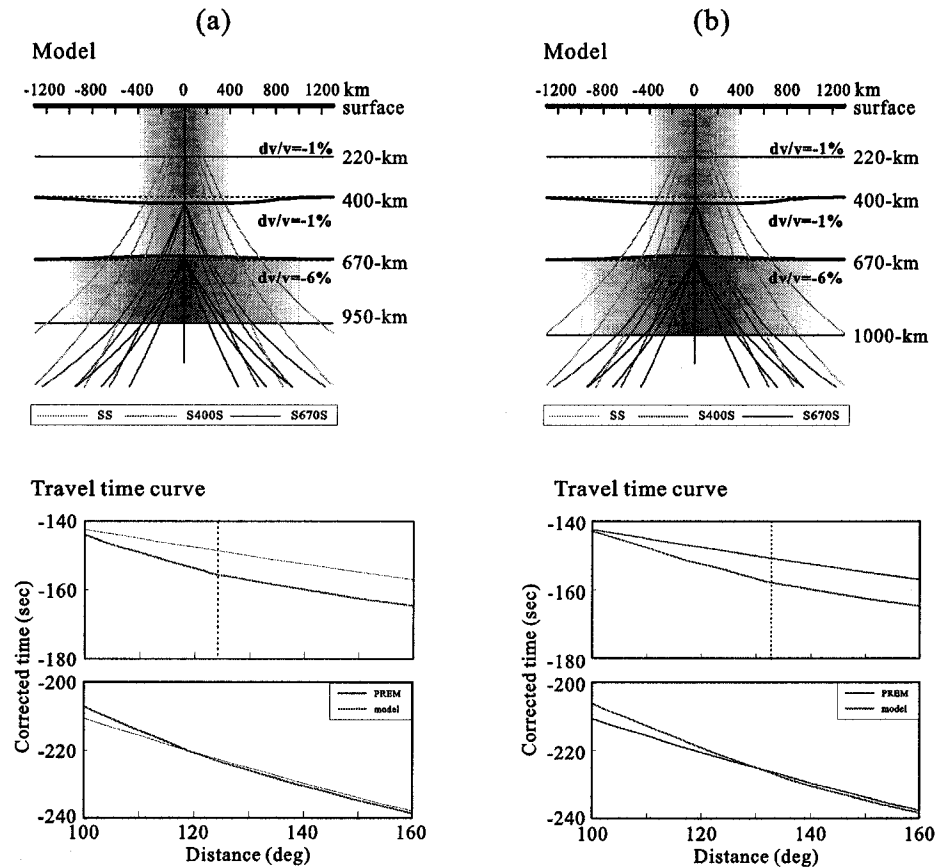
Figure 5-24 The depth of velocity anomaly in the last anomalous layer affects the jump position of differential travel time curves. The width of the anomaly is kept same for both (a) and (b). (a) The anomaly beneath 670-km discontinuity extends to 950 km. The turning point of differential travel time curve of S400S is close to 124°. (b) The velocity anomaly extends to 1000 km. The turning point of the differential travel time curve of S400S switch to 132°.

5.5 Discussion

The depths of 400-km discontinuity (416 km) are generally deeper than the global average (411 km, *Gu et al.*, 2003) at hotspot locations. The depression of 400-km at high temperature can be explained by the positive Clapeyron slope of olivine phase transition and suggest the presence of hot mantle material beneath most of the hotspot locations. The depths of 670-km discontinuity (653.5 km) are generally close to the global average of 654 km [*Gu et al.*, 1998]. This observation is inconsistent with the expected elevation from olivine dominated post-spinel phase transition at high temperatures. It is possible that mineral phase transitions in garnet are more pronounced at high temperatures [*Weidner* and *Wang*, 1998; *Hirose*, 2002; *Deuss et al.*, 2006]. As the result of garnet phase transitions, the depth of the 670-km discontinuity may not be a reliable indicator of thermal variation. The TZ thickness (235.5 km) at most hotspot locations is thinner than the global average of 242 km [*Gu et al.*, 2002]. Because of its dependence on the depth of the 670-km discontinuity, the TZ thickness may also be affected by the garnet phase transformation as well. Still, the consistently thin TZ beneath most hotspot locations suggests that thermal variations dominate the compositional (phase) variations.

The significant observation of differential ray parameter provides an additional clue on the possible depths of hotspots. There are two types of differential ray parameter variations: 1) a negative jump of ray parameter at 120° (observation I), and 2) a positive jump at 120° (observation II). Using 2D ray tracing, we are able to find two classes of models that support our observations. Model I-1 and model I-2 can adequately explain observation I. A low velocity anomaly in the upper mantle is needed to explain the time difference, while the layer beneath the TZ is responsible for the jump of differential ray parameter of $S400S$. A large anomaly of -5% or -6% beneath 670-km discontinuity could be produced by a thermal plume. If a large positive anomaly ponds beneath the 670-km discontinuity, the differential travel time curve of $S400S$ would be similar to observation II. This type of hotspots may originate from the upper mantle as secondary hotspots or from the TZ as the result of plate motions.

94

Based on the depth of 400-km discontinuity, the TZ thickness and the observation from differential ray parameters, we can identify potential depth of 17 hotspots (Figure 5-25). Hawaii, Tahiti, Macdonald, Juan de Fuca might be hotspots with potentially deep root (Figure 5-25). They are characterized by a depressed 400-km discontinuity, a thin TZ, and a differential travel time curve of Observation I. Azores, Cape Verde, Samoa, Louisville and New England are likely shallow hotspots (Figure 5-25), which exhibit a depressed 400-km discontinuity, a thin TZ and the differential travel time curve of Observation II. Bowie and Canary might be shallow upper mantle hotspots with an average 400-km discontinuity, an average TZ and a differential travel time curve of Observation II. We do not have enough constraints on Pitcairn and Marqueses hotspots which show a mild depression of the 400-km discontinuity, a relatively normal TZ and no change in the $S400S$-SS ray parameters. There is insufficient data to constrain Afar and Reunion hotspots. Furthermore, Yellowstone and Iceland are questionable deep mantle plumes, because the depths of the 400-km discontinuity beneath them are close to the global average. Table 5-2 compares our results with previous studies.
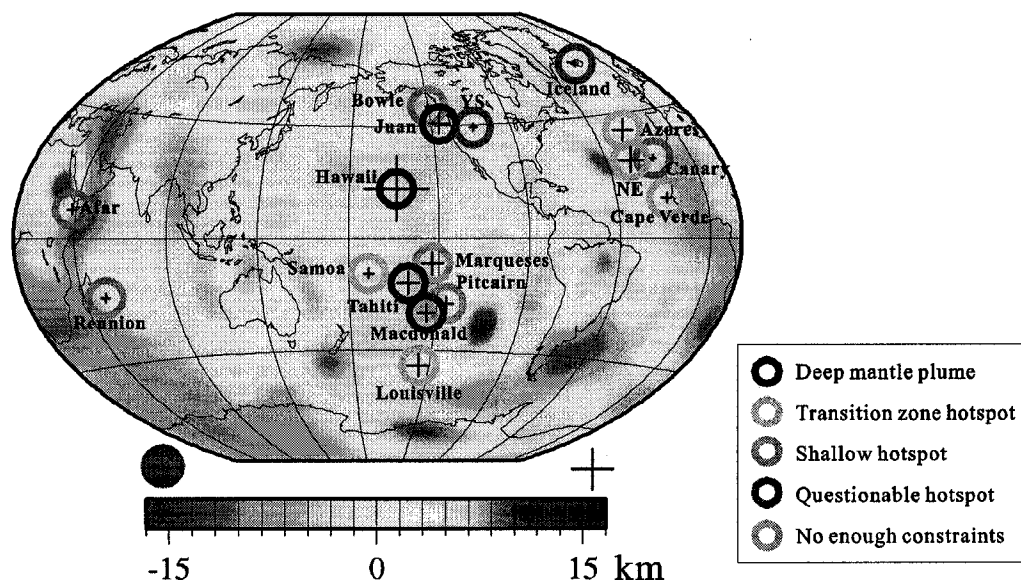
Figure 5-25 Potential depths of hotspots from this study.

The low velocity anomaly can originate from variations of temperature and/or compositions. Plume heads are known to have a mushroom-like shape, which can pond beneath the 670-km discontinuity. Chemical anomalies, phase transitions, partially molten material or low temperature may possibly account for the presence of ultra-low velocity zones detected beneath the 670-km discontinuity. The presence of iron or aluminum can affect the phase transition pressure and sharpness [*Lay et al.*, 2005] and reduce the shear velocity as well. At 900 km or 1200 km, a chemical boundary or a phase boundary may exist [*Shen et al.*, 2003].

Hawaii has large buoyancy [*Sleep*, 1990], which may be an indication of large volume of hot material ascending from the deep mantle. From our study, the depth of the 400-km discontinuity beneath Hawaii hotspot is 443 km and the TZ thickness is 229 km, both are consistent with hot upwelling. The differential ray parameter also supports the hypothesis of a potentially deep mantle plume [e.g., *Deuss*, 2007; *Mantelli*, 2006].

The evidence for a lower mantle plume beneath the Iceland hotspot remains questionable. The depth of 400-km discontinuity (407 km from this study) at Iceland hotspot is shallow than global average and the TZ thickness (248 km) is thicker than global average, which may suggest a shallow upper mantle plume; while the differential travel time curve of *S400S* is similar to observation I, which may suggest a deep-rooted mantle plume.

Yellowstone is another questionable hotspot since no clear evidence has been found for a lower mantle source [*Humphreys et al.*, 2000]. The evidence from this study only adds to the mystique of this hotspot. The depth of the 400-km and the TZ thickness are both close to the global average, and the differential ray parameter is similar to observation I. More work is necessary to fully resolve the mantle structure beneath the widely-debated hotspot.

Hotspot	this study			Deuss (2007)			Tomo		Score (Courtillot)	Bouy	obser-vation	this study
	TZ thick-ness (km)	Depth (km)		TZ thick-ness (km)	Depth (km)		S20RTS	FF				
		400	670		400	670						
Afar	213	414	630						4	1.0		?
Azores	226	420	646	243.7	401.8	645.6	Ridge	d	1+?	1.1	II	Trans
Bowie	241	411	652	237.1	414.7	651.8	Trans	mm	2+?	0.3	II	um
Canary	233	412	645	228.2	405.2	633.4		d	2	1.0	II	um
Cape Verde	236	414	650	255.0	389.7	644.7		d	2	1.6	I	Trans
Hawaii	229	443	672	245.7	405.2	650.9	Trans	pd	4+?	8.7	I	d
Iceland	248	407	655		395.8	D	Trans	d	4+?	1.4	I	d?
Juan de Fuca/Cobb	233	420	653	232.5	415.6	648.1	Ridge	mm	2+?	0.3	I	d
Louisville	236	421	657		415.4	D	Trans	pd	3+?	0.9	II	Trans
Macdonald	236	418	654	235.6	412.5	648.1	Trans		2+?	3.3	I	d
Marqueses	231	421	652	231.7	415.6	647.3	Ridge		2+?	3.3		d?
New England	231	422	653	228.0	416.3	644.3			0+?	0.5	II	Trans
Pitcairn	238	416	654	231.9	420.1	652.0	Ridge		2+?	3.3		?
Reunion	256	413	669	248.0	408.6	656.6		pd	4	1.9		?
Samoa	236	414	650	232.5	414.4	646.9	Trans	d	4	1.6	II	Trans
Tahiti	236	421	657	242.2	414.0	656.2		d	2+?	3.3	I	d
Yellowstone	242	413	655	253.9	408.3	662.2			2+	1.5	I	d?

Table 5-2 TZ measurements, observations of differential ray parameter from *SS* precursors for 17 hotspot locations and their potential origin depth. D denotes discontinuities with a double peak from *Deuss* [2007]. Tomographic information from shear wave velocity model S20RTS [*Ritsema* and *Allen*, 2003] is included and labeled to the depth of the low-velocity anomaly. Tomographic interpretations from finite frequency [FF, *Montelli et al.*, 2006] are also included, where d=deep plume, pd=potentially deep, mm=mid-mantle, um=upper mantle. The overall scores from five criteria of *Courtillot et al.* [2003] are also included. The Bouyancy flux is from *Sleep* [1990].

5.6 Summary

In this study, the non-quadratic Radon transform is introduced to investigate mantle discontinuities and velocity structures. The non-quadratic solution of the Radon transform provides higher resolution in constraining differential travel times and ray parameters than the damped least-squares solution. The reconstruction of the original time series with non-quadratic operator fully highlights the filtering and interpolation properties of the Radon transform.

The depth of 400-km discontinuity shows correlation with hotspots. The consistently deeper-than-average 400-km discontinuity at majority hotspot locations may be an important indicator of mantle plume since the Clapeyron slope of olivine dominated phase transition at the 400-km discontinuity is positive. From our results, the 670-km discontinuity shows average or normal depth beneath most hotspot locations. This is inconsistent with the elevated 670-km at higher temperature assuming that the phase transition is olivine dominated. The compositional variation and the majorite-garnet phase transition under high temperature and pressure [*Hirose*, 2002; *Deuss*, 2007] might be potential reasons. As a related parameter, TZ thickness may not be a good indicator of mantle plume if garnet plays an important role at the 670-km discontinuity under high temperatures and pressures.

The most significant observation of differential travel-time curves (or differential ray parameters) provides an alternative constraint on the possible depths of hot mantle upwellings. Two types of differential ray parameters are observed from *SS* precursor dataset ranging from 100°-160° beneath 17 hotspot locations. Several 2D numerical models with different velocity structures support these two types of observation.

Type I hotspots with observation I are supported by model I-1 and I-2, which may originate from lower mantle and are characterized by a large plume head (about 1000 km in width and 300 km in depth) ponding beneath the 670-km discontinuity. A deep thin plume tail may exist beneath plume head, though it is not possible to be imaged by the *SS* precursor dataset. In the upper mantle, a slight low velocity anomaly may exist to con-

98

tribute to the differential travel time difference. However, the velocity in the TZ is difficult to resolve.

Type II hotspots with observation II are supported by numerical model II-1 and II-2 and may originate from the TZ or the upper mantle. They may represent secondary hotspots originating from primary mantle plumes near 670-km depth.

Based on our depth measurements of the 400-km discontinuity, TZ thickness and the observation of differential ray parameter of *SdS*, we confidently identify Hawaii, Tahiti, Macdonald and Juan de Fuca as potentially deep-rooted mantle plumes. Azores, Samoa, Louisville, Canary, New England and Bowie hotspots are potentially shallow hotspot with TZ origins. Yellowstone and Iceland might be potential deep plume, but the evidence is still debatable. We don't have enough constraints on Pitcairn and Marqueses hotspots which show no indication of change in the *S400S-SS* ray parameters. Only mild depression of the 410-km discontinuity and relatively normal TZ thicknesses are observed beneath these two locations. Also, we have insufficient data to impose constraints on Afar and Reunion hotspots. These low velocity anomalies can be caused by thermal and compositional variations and it is hard to separate their effects.

This study does not account for the effects of a large Fresnel zone from *SS* precursors. The lateral scale length of our analysis is much larger than a typical thin "hotspot". We only aim at resolving the large-scale thermal/compositional structures and assume that the bounce points of *SS* fall in the center of a cap. Future work is still needed to consider the effect from a large Fresnel zone and three dimensional variations of seismic structures.

Chapter 6

Conclusions

In this thesis, I introduce the Radon transform to the global seismology and present two application examples. A distinct advantage of the Radon transform over traditional approaches is its ability to accurately constrain differential ray parameter and travel time. Combined with the effective removal of correlated/random noise through post-conditioning in the Radon domain, the Radon transform can be used to determine the topography of known TZ discontinuities accurately and detect weak mantle reflectors. In addition, through the constraint of sensitive factor ray parameter, the Radon transform is used to investigate the velocity variation in the upper-mid mantle.

The damped least-squares Radon transform is used to attenuate random noise from *SS* precursors and to depress undesired interference such as *sdsS/sdsSdiff* and *ScSdScS* in the first application. With the constraints of τ and p values, all the possible seismic discontinuities across the northeastern Pacific Ocean and the northwestern Canada are delineated. Two significant features are observed. First, there is a strong elevation of 400-km discontinuity and a normal 670-km discontinuity beneath Northwestern Canada that could be caused by reminents of the past subduction of Kula-Farallon plate into the North America plate. Second, we identify a narrow TZ beneath the northeastern Pacific Ocean that is likely caused by a low-velocity anomaly penetrating the TZ.

The second application highlights the usefullness of the Radon transform in the analysis of mantle structure and dynamics. The non-quadratic regulation is used to obtain high resolution Radon transform and impose simultaneous constraints on the differential travel time τ and ray parameter p. The Radon results are further used to infer the depths of mantle discontinuities and velocity structures beneath 17 hotspot locations. The depth of the 400-km discontinuity shows correlation with hotspots and may be an important indicator of mantle plume; while the depth of the 670-km discontinuity is inconsistent with the expected elevation of 670-km discontinuity at higher temperature and could be caused by the compositional variations and the majorite-garnet phase transition. Therefore, TZ thickness doesn't show good correlation with hotspots. The observation from

100

differential ray parameter provides additional seismic constraints on hotspots, which has been proven by numerical 2D models. Shallow and deep-rooted hot upwellings have been identified based on the depth of 400-km discontinuity, the TZ thickness and the differential ray parameter. Further work is still needed to test the observation with 3D spherical velocity models and account for the effects from large Fresnel zone of SS precursors.

Future works involve the application of Radon transform in global and regional analysis of PP precursors, ScS reverberations, converted waves (receiver functions) and, virtually, all other array techniques employed in mantle imaging.

References

1. Agee, C. B., and D. Walker (1988), Olivine flotation in mantle melt, *Earth Planet. Sci. Lett. 90*, 144-156.

2. An, Y., Y. J. Gu and M. Sacchi (2007), Imaging mantle discontinuities using least-squares Radon transform, *J. Geophys. Res.*, doi:10.1029/2007JB005009, in press.

3. Anderson, D.L., and J.H. Natland, (2005), A brief history of the plume hypothesis and its competitors: Concept and controversy, in Foulger, G.R., J.H. Natland, D.C. Presnall and D.L. Anderson, ed., *Plates, Plumes & Paradigms*, Volume Special Paper 388, Geological Society of America, p. 119-145.

4. Anderson, D. L. (2007), Dission of seismic observation of transition zone discontinuities beneath hotspot locations, by A. Deuss. *GSA Special Issue: Plates, Plumes, and Planetary Processes*, ED: G. R. Foulger and D. M. Jurdy, in press.

5. Bassin, C., G. Laske, and M. G. (2000), The current limits of resolution for surface wave tomography in North America. *EOS Trans, AGU, 81, Fall. Meet. Suppl.* F897.

6. Benz, H. M. and J. E. Vidale (1993), Sharpness of upper-mantle discontinuities determined from high-frequency reflections. *Nature, 365,* 147-150.

7. Bercovici, D. and S. Karato (2003), Whole-mantle convection and the transition-zone water filter, *Nature, 438,* 39-44.

8. Beylkin, G. (1987), Discrete radon transform. *IEEE Trans., Acoust., speech and signal proc.*, ASSP-35, 162-172.

9. Boschi, L. and A. M. Dziewonski (2000), Whole Earth tomography from delay times of P, PcP, and PKP phases: Lateral heterogeneity in the outer core or radial anisotropy in the mantle? *J. Geophys. Res., 105,* 13675-13696.

10. Bostock, N. G. (1996), Ps conversions from the upper mantle transition zone beneath the Canadian landmass. *J. Geophys. Res., 101,* 8393-8402.

11. Braunmiller, J. and J. Nabelek (2002), Seismotectonics of the Explorer region, *J. Geophys. Res., 107 (B10)*

12. Bunge, H. P. and S. P. Grand (2000), Mesozoic plate-motion history below the northeast Pacific Ocean from seismic images of the subducted Farallon slab. Nature, 405(18), 337-340.

13. Chambers, K., J. H. Woodhouse, and A. Deuss (2005), Topography of the 410-km

discontinuity from PP and SS precursors. *Earth and Planetary Science Letters, 234,* 610-622.

14. Chen, J., T. Inoue, H. Yurimoto, D. J. Weidner (2002), Effect of water on the olivine-wadsleyite phase boundary in the (Mg, Fe)$_2$SiO$_4$ system. *Geophys. Res. Lett., 29.*

15. Collier, J. D. and G. R. Helfrich (1997), Topography of the 410 and 660 km discontinuities in the Izu-Bonin subduction zones, *Geophys. Res. Lett, 24,* 1535-1538.

16. Collier, J. D., G. R. Helffrich, B. J. Wood (2001), Seismic discontinuities and subduction zones. *Phys. Earth Planet. Inter., 127,* 35-49.

17. Courtillot, V., A. Davaille, J. Besse and J. Stock (2003), Three distinct types of hotspots in the Earth's mantle. *Earth and Planetary Science Lett., 205,* 295-308

18. Davies, D., E. J. Kelly and J. R. Filson (1971), Vespa process for analysis of seismic signals, Nature Phys. Sci., 232, 8-13.

19. Depaolo, D. J. and M. Manga (2003) Deep origin of hotspots ---- the mantle plume model. *Science, 300,* 920-922

20. Deuss, A. and J. H. Woodhouse (2001), Seismic observations of splitting of the mid-transition zone discontinuity in the Earth's mantle. *Science, 294,* 354-357.

21. Deuss, A. and J. H. Woodhouse (2002), A systematic search for mantle discontinuities using SS-precursors, *Geophys. Res. Lett., 29,* x-1—x-4.

22. Deuss, A., S. A. T. Redfern, K. Chambers, and J. H. Woodhouse (2006), The nature of the 660-km discontinuity in earth's mantle from global seismic observations of PP precursors. *Science, 311,* 198-201.

23. Deuss, A. (2007), Seismic observations of transition zone discontinuities beneath hotspot locations, in G. R. Foulger & D. M. Jurdy, Plates, Plumes, and Planetary Processes. Geol. Soc. Am. Special Paper 430, in press.

24. Du, Z., L. P. Vinnik and G. R. Foulger (2006), Evidence from P-to-S mantle converted waves for a flat "660-km" discontinuity beneath Iceland, *Earth Planer. Sci. Lett., 241,* 271-280

25. Dziewonski, A. M. and D. L. Anderson (1981), Preliminary reference Earth model. *Phys. Earth Planet. Inter., 25,* 297-356.

26. Efron,B. and R. Tibshirani (1991), Statistical data analysis in the computer age.

Science, 253, 390- 395.

27. Ekström, G. and A. M. Dziewonski (1998), The unique anisotropy of the Pacific upper mantle. *Nature, 394,* 168-172.

28. Engl, H. W. and W. Grever (1994), Using the L-curve for determing optimal regularization parameters. *Numer. Math. 69,* 25-31.

29. Escalante, C., Y. J. Gu and M. D. Sacchi (2007), Simultaneous iterative time-domain deconvolution to teleseismic receiver functions, *Geophys. J. Int.* in press.

30. Flanagan, M. P., P. M. Shearer (1998), Global mapping of topography on transition zone velocity discontinuities by stacking SS precursors. *J. Geophys. Res., 103,* 2673-2692.

31. Flanagan, M. P. and P. M. Shearer (1999), A map of the topography on the 410-km discontinuity from PP precursors. *Geophys. Res. Lett., 26,* 549-552.

32. Foster, J. D. and C. C. Mosher (1992), Suppression of multiple reflections using the Radon Transform. *Geophysics, 57(3),* 386-395.

33. Foulger, G. R. (2007), The "Plate" model for the genesis of melting anomalies, *GSA Special Issue: Plates, Plumes, and Planetary Processes,* ED: G. R. Foulger and D. M. Jurdy, in press.

34. Gaherty, J. and T. H. Jordan (1995), Lehmann discontinuity as the base of an anisotropic layer beneath continents, *Science, 268,* 1468-1471.

35. Gossler, J., and R. Kind (1996), Seismic evidence for very deep roots of continents. *Earth and Planetary Science Letters, 138(1-4),* 1-13.

36. Grand, S. P., R. D. van der Hilst, and S. Widiyantoro (1997), Global seismic tomography: a snapshot of convection in the Earth. *GSA Today, 7,* 1-7.

37. Gu, Y. J., A. M. Dziewonski and C. B. Agee (1998), Global de-correlation of the topography of transition zone discontinuities. *Earth and Planetary Science Letters, 157,* 57-67.

38. Gu, Y. J., A. M. Dziewonski, and G. Ekstrm (2001), Preferential detection of the Lehmann discontinuity beneath continents, *Geophys. Res. Lett., 28,* 4655-4658.

39. Gu, Y. J. and A. M. Dziewonski (2002), Global variability of transition zone thickness. *J. Geophys. Res., 107,* No. B7.

40. Gu, Y. J., A. M. Dziewonski and G. Ekstrom (2003), Simultaneous inversion for mantle shear velocity and topography of transition zone discontinuities. *Geophys. J.*

104

Int., *154,* 559-583.

41. Gu, Y. J., A. L. Lerner-Lam, A. M. Dziewonski, G. Ekstrom (2005), Deep structure and seismic anisotropy beneath the East Pacific Rise. *Earth and Planetary Science Letters,* *232,* 259-272.

42. Hampson, D. (1986), Inverse velocity stacking for multiple elimination. *56th Ann. Internat. Mtg., Soc. Expl. Geophys.,* Expanded Abstracts, 422-424.

43. Hirose, K. (2002), Phase transitions in pyrolitic mantle around 670-km depth: implications for upwelling of plumes from the lower mantle. *J. Geophys. Res.,* *107(B4).*

44. Ito, E., and E. Takahashi (1989), Postspinel transformations in the system Mg_2SiO_4-Fe_2SiO_4 and some geophysical implications. *J. Geophys. Res.,* *94,* 10637-10646.

45. Kárason, H. and R.D. van der Hilst (1998), Improving seismic models of whole mantle P-wave speed by the inclusion of data from differential times and normal modes, *EOS, Trans. Am. geophys. Un.,* *79(45),* Fall Mtg Suppl., F656.

46. Katsura, T. and E. Ito (1989), The system Mg_2SiO_4-Fe_2SiO_4 at high pressures and temperatures; precise determination of stabilities of olivine, modified spinel, and spinel. *J. Geophys. Res.,* *94,* 15,663-15670.

47. Katsura, T., et al. (2004), Olivine-wadsleyite transition in the system (Mg, Fe)2SiO4, J. Geophys. Res. 109, doi:10.1029/2003JB002438.

48. Kawakatsu, H., and F. Niu (1994), Seismic evidence for a 920-km discontinuity in the mantle, *Nature,* *371,* 301-305.

49. Lawrence, J. F., and P. M. Shearer (2006), A global study of transition zone thickness using receiver functions, *J. Geophys. Res.,* *111,* doi: 10.1029 / 2005JB003973.

50. Lehmann, I. (1959), Velocities of longitudinal waves in the upper part of the Earth's mantle, *Ann. Geophys.,* *15,* 93-113.

51. Li, A., K. M. Fischer, M. E. Wysession, and T. J. Clarke (1998), Mantle discontinuities and temperature under the North American continental keel. *Nature,* *395,* 160-163.

52. Li, A. and K. M. Fischer (2002), Crust and upper mantle discontinuity structure beneath eastern North America, *J. Geophys. Res.,* *107(B5),* doi: 10.1029 /

2001JB000190.

53. Masters, G., G. Laske, H. Bolton, and A. M. Dziewonski (2000), The relative behavior of shear velocity, bulk sound speed, and compressional velocity in the mantle: Implications for chemical and thermal structure, in *Earth's deep interior: mineral physics and tomography from the atomic to the global scale*, vol. 117, 63-87, Eds: Karato, S., Forte, A.M., Libermann, R. C., Masters, G. & Stixrude, L., Geophys. Monogr. Ser., AGU, Washington, DC.

54. Menke, W. (1989), *Geophysical Data Analysis: Discrete Inverse Theory*.

55. Montelli, R., G. Nolet, G. Masters, F. Dahlen, and S. H. Hung (2004), Finite-frequency tomography reveals a variety of plumes in the mantle. *Science, 303*, 338-343.

56. Montelli, R., G. Nolet, F. Dahlen, and G. Masters (2006), A catalogue of deep mantle plumes: new results from finite-frequency tomography. Geochem. Geophys. Geosys. (G3), in press.

57. Neele, F., H. de Regt, and J. VanDecar (1997), Gross errors in upper-mantle discontinuity topography from underside reflection data. *Geophys. J. Int. 129(1)*.

58. Neele, F., and H de Regt (1999), Imaging upper-mantle discontinuity topography using underside-reflection data, *Geophysical Journal International, 137(1)*, 91-106.

59. Niu, F. and H. Kawakatsu (1995), Direct evidence for the undulation of the 660-km discontinuity beneath Tonga: Comparison of Japan and California array data. *Geophy. Res. Lett., 22 (5)*, 531-534.

60. Niu, F. and H. Kawakatsu (1997), Depth variation of the mid-mantle seismic discontinuity, *Geophys. Res. Lett., 24(4)*, 429-432.

61. Niu, F.L., S. C. Solomon, P. G. Silver, D. Suetsugu, and H. Inoue (2002), Mantle transition-zone structure beneath the South Pacific Superswell and evidence for a mantle plume underlying the Society hotspot, *Earth and Planetary Science Letters, 198(3-4)*, 371-380.

62. Obayashi, M., H. Sugioka, J. Yoshimitsu, Y. Fukao (2006), High temperature anomalies oceanward of subducting slabs at the 410-km discontinuity. *Earth and Planetary Science Letters, 243*, 149-158.

63. Papoulis, A.(1962), The Fourier Integral and its Applications. New York: McGraw-Hill.

64. Reif, C. G. G. Masters, M. Flanagan and P. Shearer (2007), Determination and Analysis of Long-wavelength Transition zone structure using SS precursors, *Geophys. J. Int.* submitted.

65. Revenaugh, J., and T. H. Jordan (1991), Mantle layering from ScS reverberations 3: The upper mantle. *J. of Geophys. Res., 96(B12)*, 19,781-19,810.

66. Ringwood, A. E.(1975), *Composition and Petrology of the Earth's Mantle*, 618pp., McGraw-Hill, New York.

67. Ritsema, J., M. Hagerty and T. Lay (1995), Comparison of broadband and short-period seismic waveform stacks: Implications for upper-mantle discontinuity structure. *Geophys. Res. Lett., 22 (23)*, 3151-3154.

68. Ritsema, J., H. J. Van Heijst, and J. H. Woodhouse (1999), Complex shear wav velocity structure imaged beneath Africa and Iceland. *Science, 286*, 1925-1928.

69. Ritsema, J., H, J. van Heijst (2000), Seismic imaging of structural heterogeneity in Earth's mantle: Evidence for large-scale mantle flow. *Sci. Prog., 83*, 243-259

70. Ritsema, J. and R. Allen (2003), The elusive mantle plume. *Earth and Planet. Sci. Lett., 207*, 1-12.

71. Rost, S. and C. Thomas (2002), Array seismology: methods and applications. *Reviews of Geophysics, 40*(3), 1-27.

72. Sacchi, M. and T. Ulrych (1995), High-resolution velocity gathers and offset space reconstruction. *Geophysics, 60*, 1169-1177.

73. Sacchi, M., and M. Porsani(1999), Fast high resolution parabolic RT. 69th Ann. Internat. Mtg., *Soc. Expl. Geophys.*, Expanded Abstracts, 1477-1480.

74. Scales, J. A. and A. Gersztenkorn (1988), *Robust methods in inverse theory: Inverse problems, 4*, 1071-1091.

75. Schmerr, N. and E. J. Garnero (2006), Investigation of upper mantle discontinuity structure beneath the central Pacific using SS precursors. *J. Geophys. Res., 111*.

76. Shearer, P. M.(1990), Seismic imaging of upper-mantle structure with new evidence for a 520-km discontinuity. *Nature, 344*, 121-126.

77. Shearer, P. M., and G. Masters (1992), Global mapping of topography on the 660-km discontinuity. *Nature, 355*, 791-796.

78. Shearer, P. M. (1993), Global mapping of upper mantle reflectors from long-period SS precursors. *Geophys. J. Int., 115*, 878-904.

79. Shearer, P. M. (1996), Transition zone velocity gradients and the 520-km discontinuity. *J. Geophys. Res.*, *101*, 3053-3066.

80. Shen, Y., C. J. Wolfe, and S. C. Solomon (2003), Seismological evidence for a mid-mantle discontinuity beneath Hawaii and Iceland, *Earth Planet. Sci. Lett.*, *214*, 143-151.

81. Sinogeikin, S. V., T. Katsura, J. D. Bass (1998), Sound velocities and elastic properties of Fe-bearing wadsleyite and ringwoo dite, *J. Geophys. Res.*, *103*, 20,819-20,825.

82. Sleep, N. (1990), Hotspots and mantle plumes: some phenomenology. *J. Geophys. Res.*, *95*, 6715-6736

83. Song, T. A., D. V. Helmberger, S. P. Grand (2004), Low-velocity zone atop the 410-km seismic discontinuity in the northwestern United States. *Nature, 427,* 530-533.

84. Stock, J. M., and P. Molnar (1988), Uncertainties and implications of the Cretaceous and Tertiary position of North America relative to Farallon, Kula, and Pacific plates, *Tectonics, 7*, 1339-1384.

85. Su, W. J., R. L. Woodward, and A. M. Dziewonski (1994), Degree-12 model of shear velocity heterogeneity in the mantle. *J. Geophys. Res., 99*, 6945-6980.

86. Thorson, J. and J. Claerbout (1985), Velocity-stack and slant-stack stochastic inversion. *Geophysics, 50*, 2727-2741.

87. Trad, D., et al. (2002), Accurate interpolation with high-resolution time-variant Radon transforms. *Geophysics, 67*, 644-656.

88. Trad, D., Ulrych, T. and Sacchi, M., 2003, Latest views of the sparse Radon transform: Geophysics, 68, 386-399.

89. Van der Hilst, R. D., S. Widiyantoro, and E. R. Engdahl (1997), Evidence for deep mantle circulation from global tomography. *Nature, 386*, 578-584.

90. Vidale, J. E., and H. M. Benz (1992), Upper-mantle seismic discontinuities and the thermal structure of subduction zones. *Nature, 356*, 678-683.

91. Vinnik, L., N. Kato, and H. Kawakatsu (2001), Search for seismic discontinuities in the lower mantle. *Geophys. J. Int. 147*, 41-56.

92. Vogel, C. R. (1996), Non-convergence of the L-curve regularization parameter selection method. *Inverse Problem, 12*, 535-547.

93. Wang, P., M. V. de Hoop, R.D. van der Hilst, P. Ma, L. Tenorio, Imaging of structure at and near the core mantle boundary using a generalized Radon transform: I-construction of image gathers. *J. Geophysical Research*, 2006, in press.

94. Weidner, D. J., and Y, Wang (2000), Phase transformations: Implications for mantle structure, in Earth'deep interior: Mineral physics and tomography from the atomic to the global scale. *Geophys. Monogr. Ser., 117*, edited by S. Karato et al., 215-235, AGU, Washington, D. C.

95. Willians, Q. and J. Revenaugh (2005), Ancient subduction, mantle eclogite, and the 300 km seismic discontinuity. *Geology, 33(1)*, 1-4.

96. Wilson, C. and A. Guitton (2007), Teleseismic wavefield interpolation and signal extraction using high-resolution linear radon transforms. *Geophys. J. Int. 168*, 171-181.

97. Wood, B. J. (1995), The effect of H_2O on the 410-kilometer seismic discontinuity. *Science, 268*, 74-76.

98. Xu, F., J. E. Vidale, P. S. Earle, and H. M. Benz (1998), Mantle discontinuities under southern Africa from precursors to P'P'$_{df}$. *Geophys. Res. Lett., 25*, 571-574.

99. Yusa, H. and T. Inoue (1997), Compressibility of hydrous wadsleyite (β −phase) in Mg2SiO4 by high pressure X-ray diffraction, Geophys. Res. Lett., 24, 1831-1834.